

Assessment of the Role and Origin of S* in Orange Carotenoid Protein Photoconversion

James P. Pidgeon,[†] George A. Sutherland,[‡] Matthew S. Proctor,[‡] Shuangqing Wang,^{†,¶} Dimitri Chekulaev,[§] Sayantan Bhattacharya,^{§,||} Rahul Jayaprakash,[†] Andrew Hitchcock,[‡] Ravi Kumar Venkatraman,[†] Matthew P. Johnson,[‡] C. Neil Hunter,[‡] and Jenny Clark^{*,†}

[†]*Department of Physics and Astronomy, University of Sheffield, Sheffield S3 7RH, UK*

[‡]*School of Biosciences, University of Sheffield, Sheffield S10 2TN, UK*

[¶]*Department of Chemistry and Biochemistry, University of California San Diego, La Jolla, California 92093, US*

[§]*Department of Chemistry, The University of Sheffield, Sheffield S3 7HF, UK*

^{||}*Department of Life Sciences, Imperial College London, London SW7 2AZ, UK*

E-mail: jenny.clark@sheffield.ac.uk

Phone: +44 (0)114 222 3526

Abstract

The orange carotenoid protein (OCP) is the water-soluble mediator of non-photochemical quenching in cyanobacteria, a crucial photoprotective mechanism in response to excess illumination. OCP converts from a globular, inactive state (OCPo) to an extended, active conformation (OCP_r) under high-light conditions, resulting in a concomitant redshift in the absorption of the bound carotenoid. Here, OCP was trapped in either the active or inactive state by fixing each protein conformation in trehalose-sucrose glass. Glass-encapsulated OCPo did not convert under intense illumination and

OCP_r did not convert in darkness, allowing the optical properties of each conformation to be determined at room temperature. We measured pump wavelength-dependent transient absorption of OCP_o in glass films and found that initial OCP photoproducts are still formed, despite the glass preventing completion of the photocycle. By comparison to the pump wavelength dependence of the OCP_o to OCP_r photoconversion yield in buffer, we show that the long-lived carotenoid singlet-like feature (S^{*}) is associated with ground-state heterogeneity within OCP_o, rather than triggering OCP photoconversion.

Contents

Introduction	4
Results	6
Discussion	17
Conclusions	24
Acknowledgement	24
Supporting Information Available	25
References	26
Supplementary Information	S1
S1 Literature review on S [*] in carotenoids and OCP	S1
S2 Methods	S4
S2.1 Sample preparation	S4
S2.2 Steady-state absorbance spectroscopy	S5
S2.3 Laser beam power and diameter measurements	S6

S2.4	Transient absorption spectroscopy	S6
S2.5	Time-resolved absorbance spectroscopy	S8
S2.6	Figure preparation	S10
S3	Supplementary visible/NIR ps transient absorption materials	S11
S3.1	Pump spectra	S11
S3.2	Transient absorption on OCPo and OCPr	S12
S3.3	Global lifetime analysis	S14
S4	Supplementary visible ns–ms transient absorption materials	S22
S4.1	Transient absorption dynamics of OCPo in a flow cell	S22
S4.2	Global lifetime analysis	S23
S5	Image showing no conversion in encapsulated CAN-OCPo	S30
S6	Supplementary UV-vis ps transient absorption materials	S31
S6.1	Pump spectra and comments on “bands”	S31
S6.2	Replicates at same pump wavelengths in different bands	S33
S6.3	Pump fluence independence	S36
S6.4	Global fit of dynamics parameters	S38
S6.5	Global target analysis summary and discussion	S38
S6.6	Global target analysis extended results	S39
S7	Time-resolved absorbance fit parameters and discussion	S59
S7.1	Global fit of difference dynamics	S59
S7.2	Experimental oversights discussion	S60

Introduction

Oxygenic photosynthetic organisms have evolved mechanisms to protect themselves from excess light conditions and the consequent formation of damaging reactive oxygen species. In cyanobacteria, this photoprotective response occurs over two different timescales. On long and medium timescales (hours/days), photoprotection is achieved by attenuation of protein expression and state transitions.^{1,2} On shorter timescales (seconds/minutes) photoprotection relies on a small (35 kDa), water-soluble, single carotenoid-binding protein known as the “orange carotenoid protein” (OCP), structure in Figure 1. This photoprotection process, sometimes referred to as “non-photochemical quenching” (NPQ), is initiated by the absorption of blue/green light by the OCP. Under these conditions, OCP undergoes a conformational change from a globular, inactive conformation (OCPo) to an extended, active state (OCPr)³⁻⁶ allowing it to bind to and dissipate excess energy in the photosynthetic light-harvesting phycobilisome.⁷⁻⁹ OCP’s photoactivated conformational change is accompanied by a redshift of its absorption spectrum, changing color from orange (OCPo) to red (OCPr) (Figure 1a) as the effective conjugation length of the bound carotenoid extends.¹⁰⁻¹³

While several groups have recently focused on understanding the mechanism of OCPr-induced phycobilisome quenching,^{8,14-23} here we focus instead on understanding the initial step of the OCP photocycle to help determine how excitation leads to the dramatic conformational change from OCPo to OCPr. The answer to this question is of interest because the photoswitch in OCP appears to be unique,^{10,24} and unlike other molecular and pigment-protein photoswitches such as rhodopsin²⁵ or phytochrome.²⁶ This OCP photoswitch is, nevertheless, relevant to an entire class of primary producers in many ecosystems,²⁷ and understanding the mechanism in greater depth will not only help our understanding of these key organisms, but may also help develop biomimetic optoelectronic or photonic technologies for light adaptation²⁸ or energy storage.²⁹

The significant work reported to date on this protein^{3-5,10-13,21,23,24,27,30-44} suggests that in the orange form (OCPo), the carotenoid is bound to the protein in a twisted, strained

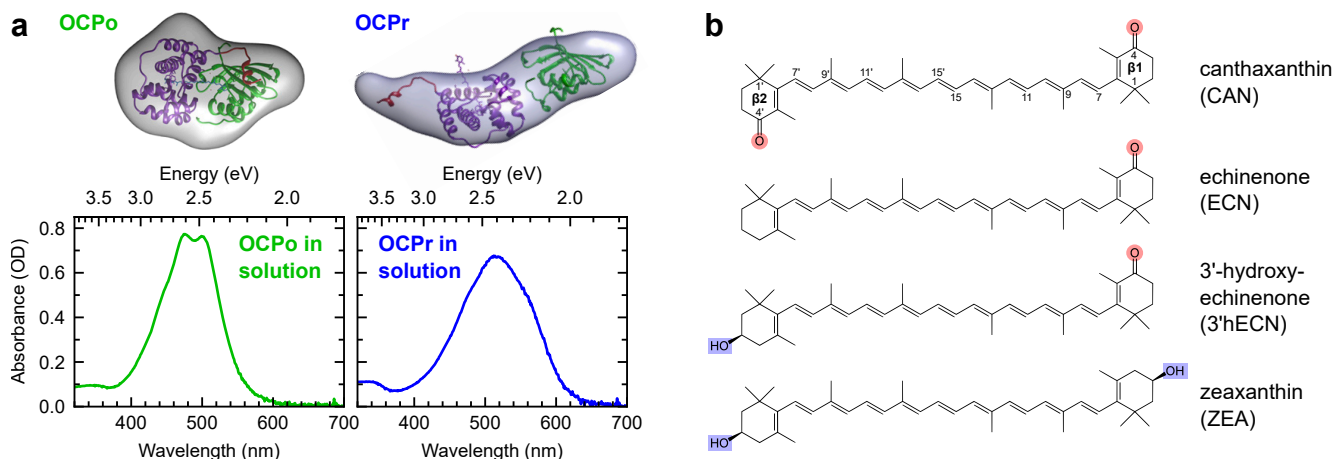


Figure 1: **OCP conformational change and carotenoids discussed in this study.** (a) Structural model of the conformational change from OCPo (left) to OCPr (right); reproduced with permission from previously reported small angle X-ray scattering (SAXS) analysis.⁵ Absorbance spectra of each conformation are displayed below. (b) Chemical structures of carotenoids discussed in this study; substitutions relative to β -carotene are highlighted, with carbonyl groups in red and hydroxyl in blue. Conventional numeration of carbons and β -rings is indicated for CAN.

geometry.^{3,12,24} It is held in this strained geometry mainly by hydrogen-bonding between its β 1-ring carbonyl group (C=O) and two conserved amino acid residues in the C-terminal domain of the protein: tryptophan 288 and tyrosine 201.^{3,10,24} Upon photoexcitation, at some time both hydrogen-bonds are believed to break,²⁴ either releasing the strain allowing the carotenoid to planarize and translocate into the N-terminal domain,^{13,24,36,39,42,45,46} or simply as a result of N- and C-terminal domain separation.⁴⁴

While there is consensus that the initial trigger of the OCP photocycle is absorption of blue/green light by the carotenoid, the processes immediately following this photoexcitation and the causes of hydrogen-bond breakage between the carbonyl group and protein Trp288/Tyr201 are an active topic of debate.^{24,33,35,44} A recent comprehensive study by Konold *et al.* using time-resolved UV-visible and polarized mid-infrared spectroscopy was able to follow the electronic and vibrational degrees of freedom through the OCP photocycle from femtoseconds to 0.5 ms.³⁶ A key hypothesis of this study is that photoexcitation of a carotenoid excited state, dubbed S^* , triggers the photocycle.

The presence of a putative S* feature in transient absorption spectroscopy studies of carotenoids has been discussed in the literature for several decades. Although debate remains,^{12,30,34,36,37,39,39–41,43,44,47–64} as described further in our literature review in the Supplementary Information (SI), the prevailing hypothesis seems to be that S* is due to ground state heterogeneity, giving rise to small changes in spectral features with different excitation wavelengths.^{48,49,60} This description of the S* feature as an artifact of ground-state heterogeneity, rather than a distinct excited state, suggests that the role of S* in OCP photoconversion merits further investigation.

To determine whether there is a correlation between the S* feature and OCP photo-switching, we measure the relative yield of both the S* feature and the OCPo→OCPr photoconversion process as a function of pump wavelength. To immobilize the carotenoid for spectroscopic analysis, we trapped OCP in either its OCPo or OCPr form at room temperature using a trehalose-sucrose glass^{65,66} (herein referred to simply as “trehalose”), as previously described.^{67,68}

We conclude that the S* spectral feature cannot be directly correlated with the photoconversion yield and that this spectral feature merely arises from ground-state OCPo heterogeneity, comparable with solution-phase carotenoid studies.^{48,49,62–64} We do, nevertheless observe a wavelength-dependent photoswitching yield, showing that higher energy photons cause more rapid photoswitching.

Results

OCP binding ~100% canthaxanthin prevents carotenoid heterogeneity. When extracted from *Synechocystis*, OCP binds a mixture of carotenoids that proportionally vary depending on the method used for production, leading to heterogeneous samples that complicate spectroscopic analysis. Here we employed a dual-plasmid system, comprised of pAC-CANTHi₁ to generate carotenoid (~100% CAN)⁶⁹ and pET28a::OCP to produce OCP.

Maintenance of both plasmids in BL21(DE3) *E. coli* allows incorporation of the carotenoid *in vivo* producing OCP binding near-100% CAN. See SI Section S2.1 for further details on the method. Unless stated otherwise, all experimentation was conducted with OCP containing near-100% CAN.

OCP trapping does not affect initial photophysics. To study the early-time photophysics of OCP without problems associated with full photoconversion of the sample during measurement, we trapped the protein in a trehalose matrix.⁶⁷ The lack of complete pho-

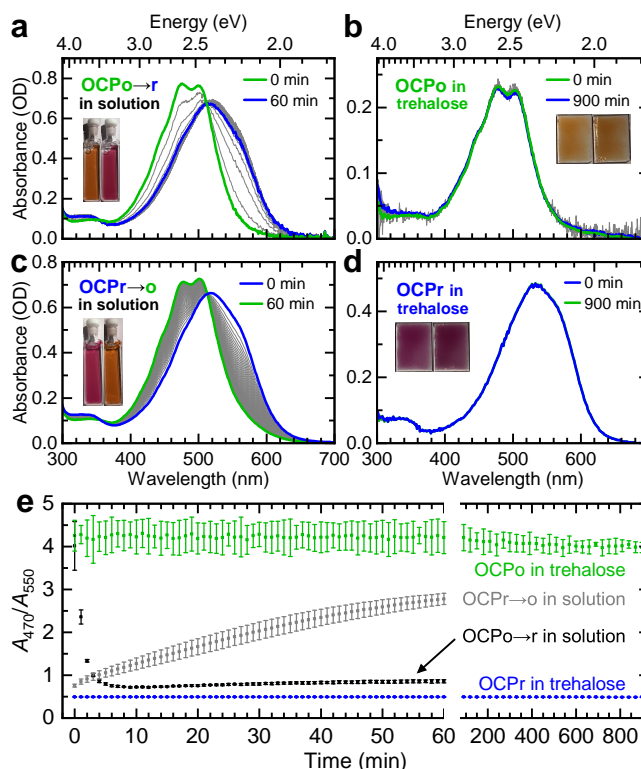


Figure 2: **Conversion of OCP in solution (a,c) and trapping in trehalose glass (b,d).** Absorbance spectra of OCPo (a,b), taken in 1 min intervals under constant white-light illumination ($1600 \mu\text{mol photon m}^{-2} \text{s}^{-1}$), or OCPr (c,d) taken in 1 min intervals at 22 °C in darkness. Noise contributions seen in (a,b) are due to scatter of the white-light illumination. (e) Dynamics of OCP conversion in trehalose glass and in solution represented as the ratio of the absorbance at 470 nm and 550 nm in 1 min intervals. Data points averaged from three experimental replicates, with error bars showing standard deviation. The optical path length for solution measurements was 1 mm.

toconversion in trehalose is demonstrated in Figure 2. Here we monitored the absorbance spectra of OCPo/OCPr in buffer (a,c) and in trehalose (b,d) as a function of time either

under illumination with intense white-light ($1600 \mu\text{mol photon m}^{-2} \text{s}^{-1}$; Figure 2a,b) or in the dark (Figure 2c,d) at room temperature. Full photoconversion of OCPo in solution occurred within 6 min of illumination and the reverse conversion completed within 60 min in darkness. No conversion was observed in either sample encapsulated in trehalose during the 15 hours measured, with absorbances the same at all times (Figure 2e).

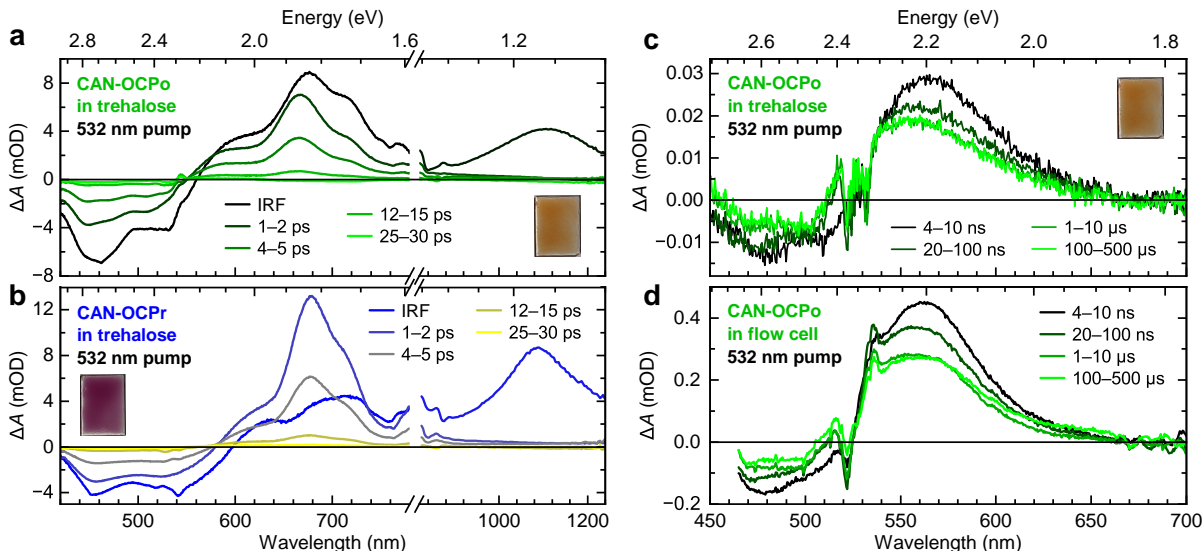


Figure 3: **Picosecond (a,b) and ns–ms (c,d) transient absorption spectra of CAN-binding OCP in trehalose glass (a–c) and in buffer (d) with pump wavelength 532 nm.** Singlet decay occurs over ~ 5 ps (a,b), and long-lived and static features are seen on the long-time (c,d), consistent with the literature on OCPo and OCPr in buffer.^{34,36,40} Spectra have been averaged between the times indicated. In (d), buffer was constantly refreshed by use of a flow cell. Pump fluence was set to $200 \mu\text{J cm}^{-2}$ for (a–c), and to $1600 \mu\text{J cm}^{-2}$ for (d). The instrument response function (IRF) spectrum was taken at a nominal delay of 0 fs, and is heavily impacted by a coherent artifact.

Transient absorption spectra of OCP in trehalose are shown in Figure 3a–c. To confirm that the early-time photophysics of OCP is not impacted by being trapped in the trehalose, or by the presence of only one carotenoid type (near-100% CAN), we compare these spectra to solution measurements (Figure 3d) and those reported in the literature, *e.g.* Ref.^{34,36,40} We find that the spectra of OCP measured on these timescales in trehalose show no obvious differences to those measured in flowed solution over the same timescales. For example, the picosecond spectra and dynamics (Figure 3a,b) are similar to those observed in CAN-binding

OCP,³⁴ RCP³⁴ and N-terminal domain helical carotenoid proteins (HCP) HCP2 and HCP3 in solution.⁴⁰ This includes the presence of significant excited-state absorption (ESA) in the 700 nm to 900 nm spectral range that is due to intramolecular charge transfer (ICT) state absorption.^{34,40} The longer-time behavior (Figure 3c) is also near-identical to results on 3'hECN-binding OCP reported recently³⁶ and to solution measurements in buffer (Figure 3d), up to at least 0.7 ms. Overall, our results demonstrate that the early-time photophysics of CAN-OCPo are not affected by the trehalose environment.

Importantly, we also observe no photoconversion during the transient measurements on trehalose films: inspection of the films after all experiments with pulsed lasers show no detectable color change (apart from bleaching in measurements using high pump fluences; see SI Figure S16) and the transient absorption spectra of individual sweeps from Figure 3c did not change over the course of the experiment (over 18 hours).

To summarize, trapping the OCPo and OCP_r protein conformations in trehalose glass prevents the full OCPo→OCP_r photoconversion. However, the initial photophysics remains unchanged in the trehalose compared with buffer and OCP remains in its native form within the trehalose. Trehalose-OCP films therefore provide us with stable solid-state samples that can help elucidate the mechanism of OCPo→OCP_r photoconversion.

Transient absorption spectroscopy shows different OCPo ground-state conformations. To test the recent hypothesis that a long-lived singlet (often dubbed S*) is an initial trigger for the photoconversion mechanism,^{36,39,43} we first turn to pump wavelength-dependent transient absorption measurements on OCPo in trehalose, shown in Figure 4. Here, to ensure a constant excitation density at each pump wavelength, we tuned the pump powers to target an initial ~ 3 mOD peak ground-state bleach (GSB) response at 1 ps. A different sample spot was pumped and probed per λ_{pump} . For most pump wavelengths, this resulted in a relatively low pump power (see SI Figure S17 for pump profiles and powers used). We chose a UV-vis probe spanning 370 nm to 690 nm to better resolve the GSB region.

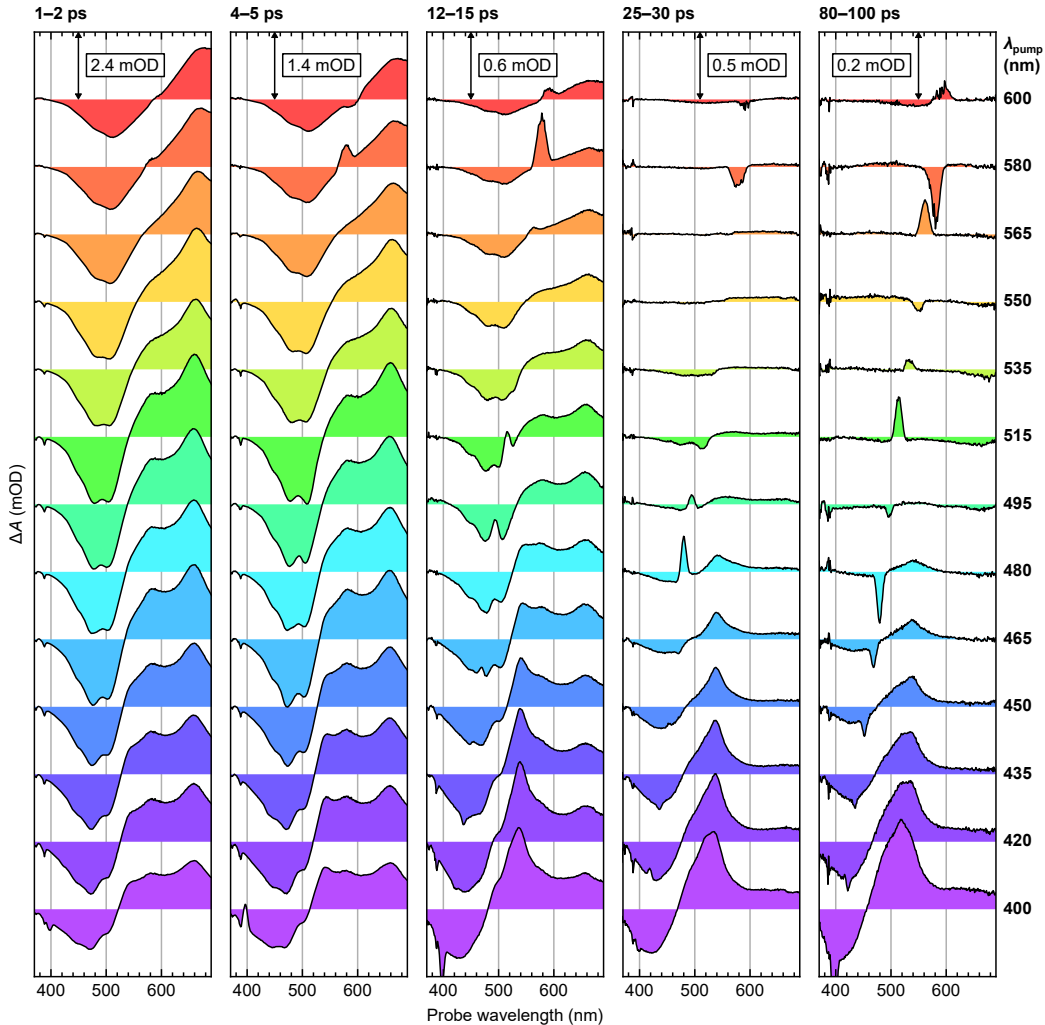


Figure 4: **Transient absorption spectra of CAN-binding OCPo in trehalose glass with pump wavelengths in the range 400 nm to 600 nm (specified on the right).** Spectra have been averaged between the times specified on the top, with arrows denoting the size of the y -axis scale (ΔA in mOD) for that column of spectra. Pump powers were tuned to give an initial ~ 3 mOD peak GSB response at 1 ps. We observe that higher-energy (lower wavelength) pump wavelengths (400-480 nm: blue/purple) give rise to long-lived features previously assigned to S^* -like features.³⁶ As the pump wavelength is tuned to lower energies (longer wavelengths), the spectra continuously shift spectrally, demonstrating ground-state heterogeneity. Note that sharp positive and negative peaks are due to noise in the pump scatter region.

We start by describing spectra with 495 nm pump, close to the peak absorption of OCPo and similar to pump wavelengths used in previous reports.^{12,34,36,40} As expected, the spectra show signatures of S_1 decay (~ 5 ps visible ESA decay) and associated effects due to intramolecular vibrational redistribution (IVR) and vibrational cooling (VC) (*e.g.* narrowing,

shifting, changes in vibronic lineshapes, see Refs.^{57,58} for details). We note that carotenoids, particularly keto-carotenoids such as CAN, demonstrate a wealth of different diabatic states and that any S_1 -like features we observe likely originate from S_1 /ICT (and other) admixtures, with confounding effects due to IVR/VC. In this work to simplify the discussion we describe the states as S_1 , S_2 , etc. with the implicit assumption of them being mixed states.

We now discuss the impact of redder pump wavelengths (from 495 nm to 600 nm) on the OCPo photophysics. For all times >1 ps, as λ_{pump} increases from 495 nm to 600 nm, we observe a continuous spectral evolution, consisting of two main factors: (1) a decrease in the S_1 - S_n ESA vibronic replica around 585 nm, together with an apparent narrowing of the entire ESA feature, and (2) a continuous change in the GSB vibronic structure, with the peak around 507 nm increasing relative to the ~ 481 nm peak. While (1) could be partially explained in terms of effects associated with IVR and VC, as modeled by Balevičius *et al.*,⁵⁷ the effect we observe is significantly more pronounced and long-lived, and therefore cannot be solely due to IVR and VC. In addition, considerations of IVR and VC do not explain (2). We therefore assign the λ_{pump} -dependence of the spectra as the result of heterogeneity in CAN-OCPo with a presence of multiple ground-state species, as others have done for OCP.^{12,30,34,40,41,60} As discussed below, we hypothesize that CAN-OCPo forms either a predominantly “blueshifted form” favorably excited with bluer pump wavelengths and a “redshifted form” (distinct from OCP_r) favorably excited with redder pump wavelengths. Both forms have similar lifetimes associated with their respective S_2 (~ 100 fs time constant) and S_1 (~ 5 ps) states with implicit admixtures (see global target analysis in SI Sections S6.5 and S6.6).

Pumping with wavelengths $\lambda_{\text{pump}} = 480$ nm and bluer results in the formation of additional and distinct S_1 -like excited-state features with significantly longer decay time constants than the expected ~ 5 ps. For $\lambda_{\text{pump}} = 480$ nm to 400 nm, features appear in the 25–30 ps and 80–100 ps spectra, and become stronger with decreasing pump wavelength. These have a comparatively unstructured GSB, and an ESA consisting of broad peak(s) around 520 nm

to 540 nm and a long, unstructured red tail. These features are consistent with additional ground-state species of OCPo that are only excited at ~ 480 nm and below, very similar to the contribution reported as S^* and assigned to ground-state non-all-*trans* conformations in studies of carotenoids in solution.^{48,49} To be consistent with the OCP literature, we will refer to this as an S^* -like feature. Its spectrum is similar to that described as S^* by Konold *et al.*³⁶ for 3'hECN-OCP and thought to be the precursor of OCP switching.^{36,39,43} It is also similar to the S^\sim state reported by Niziński *et al.* in ECN-OCP, who assign it to a non-photoactive carotenoid “impurity” (*e.g.* β -carotene) in their OCP sample.⁶⁰ We note that while largely obscured by this new S^* -like feature, the aforementioned spectral evolution behavior described above as (1) and (2) are still present with $\lambda_{\text{pump}} = 400$ nm to 480 nm.

We note that a different sample spot was pumped and probed per λ_{pump} to avoid any degradation-associated affects. The sample spots chosen were practically random. We rule out heterogeneity across the OCPo sample volume as the source of the phenomena seen for the following reasons: (1) the transient absorption spectra and dynamics for different sample spots probed with near-identical pumps (the same nominal λ_{pump} between different “bands”), shown in SI Figures S18 and S19, appear to be near-identical (see SI Section S6.2 for details), (2) the variations seen with decreasing λ_{pump} are directed trends, as opposed to random variations (as would be expected with practically random choices of the pump/probed sample spot). We therefore assign heterogeneity in OCPo itself. A similar λ_{pump} -dependence is observed in OCP_r, using 532 nm and 485 nm pumps; see SI Section S3 for details and figures.

To summarize, from inspection of the spectra of pump wavelength-dependent transient absorption on OCPo in trehalose (Figure 4), we have identified ground-state heterogeneity within OCPo, including a form with a long-lived (~ 65 ps) decay time constant that we term S^* -like.

To determine the long-lived S^* -like yield, we perform a global triexponential fit of normalized dynamics in the >500 fs time-region (Figure 5). We take the average ΔA in the

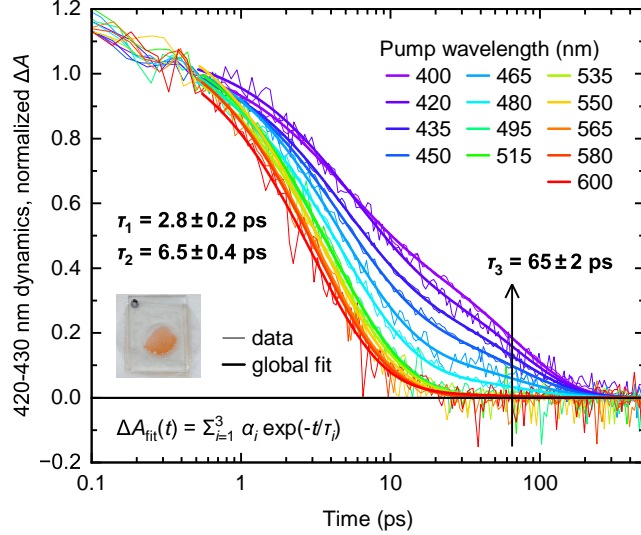


Figure 5: **Normalized dynamics and a triexponential global fit (equation inset bottom-left) in the long-lived GSB region for transient absorption experiments using different pump wavelengths on CAN-binding OCPo.** The S*-like amplitude clearly increases as pump wavelength is reduced from 480 nm to 400 nm. Dynamics are taken as the 420–430 nm probe range average, and subsequently normalized to average one in the 0.35 ps to 0.65 ps range. Errors denote fit parameter standard errors.

420–430 nm probe range (close to the peak GSB of the long-lived singlet features – see Figure 4), normalize to unity at ~ 0.35 – 0.65 ps, plot against time, and fit for times >500 fs (beyond any features associated with the coherent artifact and decay of S₂-like states) with a global triexponential fit with the following equation:

$$\Delta A_{\text{fit}}(t) = \alpha_1 \exp(-t/\tau_1) + \alpha_2 \exp(-t/\tau_2) + \alpha_3 \exp(-t/\tau_3) \quad (1)$$

Here t is the delay time in the transient absorption, α_i are fitted amplitudes with the applied lower-bound condition $\alpha_i \geq 0$, and τ_i are fitted time constants that are shared between the different pump wavelengths in the global fit. The dynamics and fit are shown in Figure 5, the fit parameters are printed in SI Table S4. We find that α_3 , the amplitude associated with the S*-like feature ($\tau_3 = 65 \pm 2$ ps), shows a significant wavelength dependence, increasing from 0% at $\lambda_{\text{pump}} \geq 495$ nm to $\sim 50\%$ at $\lambda_{\text{pump}} = 400$ nm, see Figure 7. This dependence matches with supplementary global target analysis; an additional component is required for

fitting $\lambda_{\text{pump}} < 495$ nm (see SI Sections S6.5 and S6.6).

In short, using pump wavelength-dependent transient absorption measurements on OCPo in trehalose, we have found evidence of heterogeneity in OCPo with populations of distinct OCPo “forms”, including an S*-like form. We have quantified the proportion of this S*-like feature as a function of λ_{pump} . If, as reported recently,^{36,39,43} this S*-like feature is a trigger for the OCPo to OCP_r photocycle, the OCP_r yield should show a similar excitation wavelength dependence. Therefore, in the next section, we turn to quantifying the excitation wavelength-dependence of the solution OCPo→OCP_r photoconversion yield.

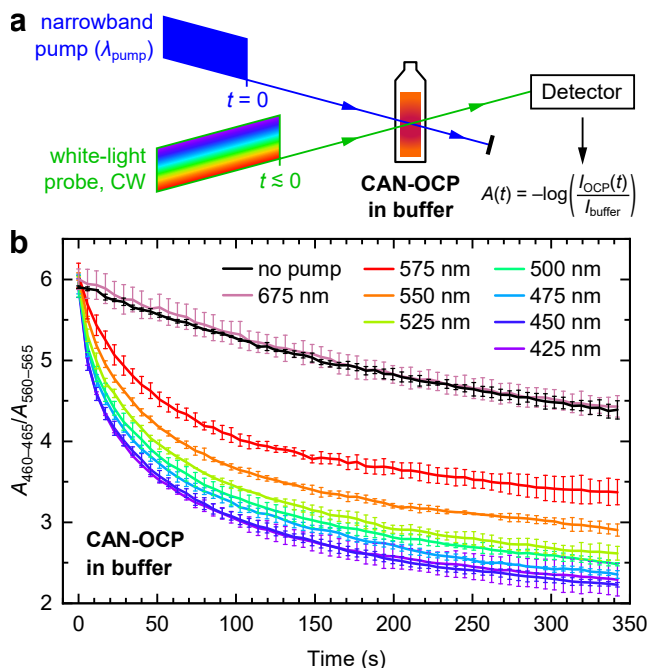


Figure 6: **Experimental setup for absorbance measurements of CAN-binding OCP in buffer that is continually photoconverted by narrowband pump light (a), and average absorbance ratios against time (b).** The pump power was tuned to give approximately the same OCPo excitation rate per-pump wavelength (except for 675 nm). All absorbed pump wavelengths give a conversion yield greater than the white-light probe alone, with the yield increasing as pump wavelength is reduced from 575 nm to 425 nm. Absorbance ratios are averaged from three experimental replicates, and the error bars show the standard deviation. The cuvette width was 2 mm.

Photoconversion is pump wavelength-dependent, but does not correlate with S*. We quantify the yield of OCPo→OCP_r photoconversion as a function of pump wavelength using absorbance measurements of dark-adapted OCPo in buffer as a function of

time, Figure 6b. A simplified diagram of the experiment is shown in Figure 6a and details of the method are outlined in SI Section S2.5; importantly, the pump power was tuned to give approximately the same rate of OCPo excitations for each pump wavelength (except for 675 nm) based on the dark-adapted absorbance. The conversion from OCPo to OCPr can be tracked by monitoring the ratio of absorbance due to OCPo at 460–465 nm and that of OCPr at 560–565 nm ($A_{460-465}/A_{560-565}$). The dynamics in Figure 6b are the average of three experimental replicates.

Figure 6b shows that the OCP photocycle is triggered by excitation into the OCPo absorption band, right down to the band-edge. Indeed, we observe photoconversion with pump wavelengths that do not generate S*-like features in transient absorption spectroscopy measurements (>480 nm, see Figure 4). This suggests that the S*-like feature is not required for photoconversion.

However, rather surprisingly, we do find that the photoconversion dynamics (Figure 6b) have a pump wavelength dependence. Before describing this pump wavelength-dependent behavior in detail, we first note that the white-light probe alone triggers some OCPo→OCPr photoconversion; see the average absorbance-ratio dynamics obtained without the pump (probe light only; black line) and 675 nm pump (non-absorbed pump; pink line). In subsequent analysis, we account for this “background” white light-induced photoconversion by subtracting the dynamic obtained without the pump from the dynamic at each pump wavelength to obtain

$$\Delta \left(\frac{A_{460-465}}{A_{560-565}} \right) = \left(\frac{A_{460-465}}{A_{560-565}} \right) - \left(\frac{A_{460-465}}{A_{560-565}} \right)_{\text{no pump}}. \quad (2)$$

The resulting difference dynamics are plotted as points in SI Figure S38 and are fitted using a global biexponential fit

$$\Delta \left(\frac{A_{460-465}}{A_{560-565}} \right)_{\text{fit}} = \beta_0 - \beta_1 \left[1 - \exp \left(-\frac{t}{T_1} \right) \right] - \beta_2 \left[1 - \exp \left(-\frac{t}{T_2} \right) \right] \quad (3)$$

to quantify the pump wavelength dependence of the photoconversion temporal behavior. Here t is the time after the pump is turned on, β_0 is a fitted offset term, β_1 , β_2 are fitted amplitudes, and T_1 , T_2 are fitted time constants that are shared between the different pump wavelengths in the global fit. The fit is shown as lines in SI Figure S38, the fitted β_1 ($T_1 = 4.12 \pm 0.18$ s; error denotes fit parameter standard error) and β_2 ($T_2 = 32.9 \pm 0.7$ s) are plotted as points in Figure 7b and other fitted parameters are shown in SI Table S5. A key finding is that although the amplitude term of the slower component (β_2) is roughly the same for each pump wavelength, the amplitude for the faster component (β_1) significantly increases with decreasing pump wavelength.

Using the amplitudes as a proxy for relative yield of photoconversion (Figure 6) or S*-like features (Figures 4 and 5), we compare the relative yield of OCP_r in buffer to the yield of the S*-like features in trehalose. Figure 7a shows the amplitude α_3 due to the S*-like features from the triexponential global fit of transient absorption dynamics (Figure 5) overlaid with the OCP_o in trehalose absorbance spectrum, and Figure 7b similarly shows the amplitudes from the photoconversion experiment (Figure 6) in buffer overlaid with the dark-adapted OCP_o in buffer absorbance. We find that photoconversion and the S*-like features do not follow the same pump wavelength dependence. Indeed, α_3 has a distinct threshold pump wavelength (480 nm), while β_1 and β_2 have amplitude at all pump wavelengths measured. The reason for the pump wavelength dependence of β_1 and β_2 , and thus the photoconversion behavior, is unclear.

To summarize, time-resolved absorbance measurements of continually-photoconverting OCP in buffer have shown that: (1) all wavelengths absorbed by OCP_o cause the transition to OCP_r, (2) photoconversion yield increases with decreasing pump wavelength, with the significant increase in the amplitude of a “fast” (~ 4 s) component, and (3) the pump wavelength dependence of the S*-like feature in transient absorption spectroscopy cannot explain the pump wavelength-dependent photoconversion yield. This leads us to reject the recent hypotheses^{36,39,43} that “S*” is the trigger for the photocycle.

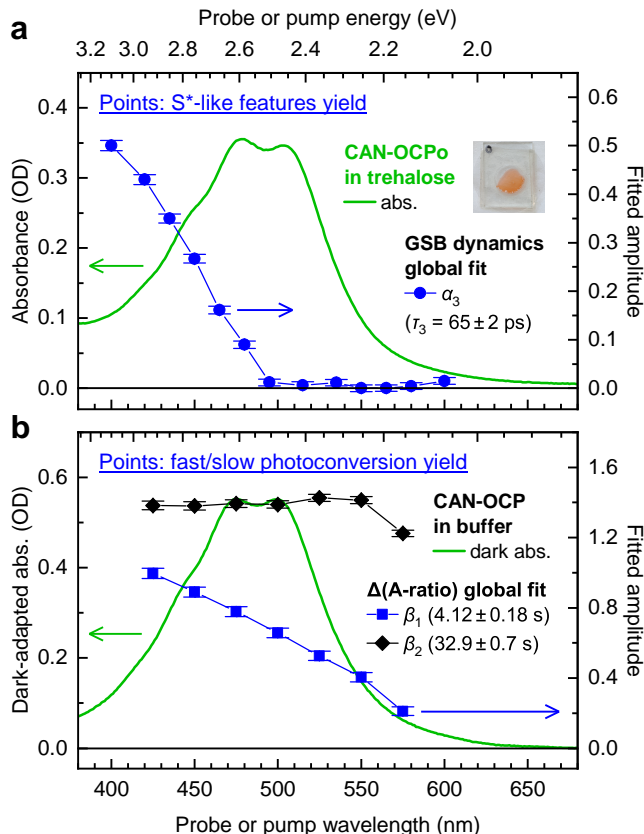


Figure 7: **Fitted amplitudes from the global fits of dynamics for different OCP experiments, with dark-adapted absorbance of OCPo samples studied.** (a) Absorbance of OCPo in trehalose (line, left axis), with fitted amplitude α_3 from a global triexponential fit of picosecond transient absorption dynamics (points, right axis). (b) Absorbance of dark-adapted (initially) OCPo in buffer (line, left axis), with fitted amplitudes β_1, β_2 against pump wavelength from a global biexponential fit of photoconverting solution dynamics (points, right axis). The apparently large absorbance at low wavelengths for OCPo in trehalose compared to that in buffer is due to increased scatter in the trehalose sample. Error bars denote fit parameter standard errors. Dynamic fits are shown and described in Figure 5 and Table S4 for transient absorption, and SI Figure S38 and SI Table S5 for photoconverting solution.

Discussion

Long-lived singlets do not appear to be associated with photoconversion. Long-lived singlet excited states have been suggested to play a pivotal role in the initial steps of OCPo to OCP_r photoconversion.^{36,39,43} This argument was based on sequential-model global lifetime analysis on transient absorption data with UV-vis and mid-IR probes, where the “S* state” was assigned a 24 ps lifetime,³⁶ within the 20–100 ps range typically assigned

to the S* feature in free carotenoids^{48,49} and other OCP studies.^{36,39–41,60} Here we show that photoconversion does not correlate with the long-lived S*-like feature in CAN-OCPo; there is no apparent correlation between the pump wavelength dependence of the conversion in buffer (Figure 7b) and the pump wavelength dependence of the “S*” yield (Figure 7a). Note our rejection of the hypothesis is independent of the physical identity of the long-lived S*-like feature, which we argue below arises from ground-state heterogeneity originating from CAN-associated chromophores, but is superfluous to our argument here.

Excitation dependent behavior in photoconversion can originate from two broad categories: chromophore or environmental heterogeneity, which we know is present in this sample (see below), or excitation-dependent processes such as intersystem crossing, which has previously been observed in carotenoids,⁷⁰ and implicated in OCP photoconversion.⁷¹ With the available data we cannot conclude whether either, or both, of these factors influence the photoconversion yield and suggest more detailed excitation-wavelength dependent studies using additional spectroscopic handles such as photoluminescence, Raman, transient mid-IR absorption spectroscopy is required. These studies are beyond the scope of the current work.

We note that the excitation wavelength dependence of photoconversion yield is primarily due to a “fast” photoconversion process ($T_1 \approx 4$ s) (see SI Figure S38). While the physical identity of the fast (wavelength dependent) and slow (wavelength independent) components of photoconversion remains obscure, recent work suggests that OCP dimerization can affect the photoconversion dynamics on this time scale,^{72,73} although it is unclear whether dimerization would also contribute to the excitation dependence.

OCPo photophysics show ground-state heterogeneity. Our pump-wavelength-dependent transient absorption spectra (Figure 4) demonstrate a surprisingly rich excitation dependence, given our attempts to restrict the carotenoid heterogeneity (all samples initially contain $\sim 100\%$ CAN). We note, in particular, that the observed changes in ground-state bleach (GSB) as a function of pump wavelength indicate that multiple ground-state OCPo species are present. The clearest form is the “S*-like form”, discussed above. It is only

apparent with pump wavelengths ≤ 480 nm, has the bluest GSB (highest S_2 -like energy), and a relatively long decay time constant (~ 65 ps). However, two other distinct forms are also present, which we denote the “blueshifted form”, most strongly excited with a pump wavelength of 495 nm and characterized by a relatively short decay time constant (≤ 10 ps) and a “redshifted form” with the reddest identified GSB contribution (lowest S_2 energy) and a decay time constant similar to the blueshifted form.

We first consider the possible origin of the S^* feature. The photophysical properties of carotenoids strongly depend on their effective conjugation length; as the length increases, the S_1 lifetime and energy decrease, the $S_0 \rightarrow S_2$ transition energy decreases, and the C=C vibration energy (ν_1 -peak in Raman spectroscopy) decreases.^{52,74,75} Such behavior might explain the origin of the long-lived “ S^* ” feature. From the non-radiative energy gap law,⁷⁶ we estimate the S^* -associated S_1 energy to be $\sim 16\,400$ cm^{-1} , corresponding to a conjugation length of $N \approx 8.2$.^{77,78} Similarly, in a resonance Raman spectroscopy study, Kish *et al.*¹² noted an excitation-wavelength dependent blue 1527 cm^{-1} shoulder of the main ν_1 peak. This ν_1 energy corresponds to an effective conjugation length of $N \approx 9$.¹² These values are shorter than the expected CAN conjugation length $N \approx 13$ and would require complete non-participation of the β_1 and β_2 rings to the effective conjugation length, which has not been observed to our knowledge. It is also unlikely that out-of-plane distortions of the terminal rings could change the effective conjugation length to such an extent.^{34,75}

Studies of carotenoids in solution, where signatures extremely similar to our S^* -like features have been identified in samples that are nominally all-*trans*, may contain impurities. A transient absorption study of β -carotene in solution by Ostroumov *et al.* showed that a long-lived contribution with lifetime 20–100 ps disappears if the samples are purified to all-*trans*- β -carotene immediately prior to a measurement. A 3-level carotenoid model with consideration of VC in the S_1 state is then sufficient to explain the photophysics in these purified samples.⁴⁸ It was suggested that the “impurities” removed through purification might be due to chromophore products from β -carotene, such as shorter conjugation-length

carotenoids. Work by Polak *et al.* undertaking pump wavelength-dependent transient absorption measurements on β -carotene and astaxanthin (a keto-carotenoid) in toluene confirmed the pump wavelength dependence of the long-lived contribution and showed the dependence in turn matches Ostroumov *et al.*'s impurity absorbance.⁴⁹ The wavelength dependence of Ostroumov *et al.*'s impurity absorbance and Polak *et al.*'s long-lived signal amplitude both follow a similar profile to our own pump wavelength dependence on the long-lived S*-like feature in OCPo (*e.g.* the dependence of α_3 on pump wavelength; Figure 7a).

From the observations and assignments made regarding the ECN-OCPo resonance Raman spectra by Kish *et al.*,¹² the similarity to an “impurity” contribution identified for carotenoid-in-solution studies,^{48,49} and the similarity to a 60–100 ps feature in transient absorption spectroscopy, assigned to a non-photoconverting “impurity”-OCP fraction,⁶⁰ we hypothesize that the S*-like species in OCPo is due to ground-state contributions of short conjugation length carotenoids or carotenoid-like chromophores. The precise identity of these chromophores remains to be determined, although similarities with Ostroumov’s work⁴⁸ suggests they may be CAN-associated products.

We now turn to the identities of the redshifted and blueshifted forms of OCPo described above. We are confident that these exist due to significant changes in the excited state absorption (ESA) vibronic replica intensities and the ground state bleach (GSB) vibrational structure in transient absorption experiments scanning pump wavelengths from 495 nm to 600 nm (Figure 4). We observe IVR and VC signatures at all pump wavelengths, but the pump wavelength dependence of these cannot explain the extent of the changes in the transient absorption spectra.^{55–58} As explained in the results, the effects of IVR and VC make application of multi-exponential dynamic fitting and global lifetime/target analysis poorly suited for this system, particularly with both forms decaying with similar lifetimes. We recall our global triexponential fit of the normalized dynamics in the 420–430 nm GSB region (Figure 5); while $\tau_3 = 65$ ps can safely be associated with the S*-like form of OCPo due to its 1-order time difference between that and the earlier-time dynamics, the extracted

$\tau_1 = 2.8$ ps and $\tau_2 = 6.5$ ps have a mixed and unknown physical correspondence, likely mixed S_1 /IVR/VC for multiple ground-state OCPo forms. Meanwhile, the SADS2 and SADS3 (Figure S21b,c) extracted from global target analysis also have an unknown correspondence, and vary significantly with pump wavelength. Applying a model accounting for IVR and VC such as those designed by Balevičius *et al.*^{55–58} is beyond the scope of this paper, considering the ground-state heterogeneity within the OCPo system.

We hypothesize that the redshifted and blueshifted forms arise from heterogeneities in the protein environment, associated with only minor CAN conformational differences.^{74,79} We reach this conclusion because, while the S_1 profiles and decay times of both redshifted and blueshifted forms are similar, the S_2 -associated GSB is significantly different in the two forms. S_1 and S_2 transition lifetimes/energies are affected differently by changes in conformation and environment; S_1 lifetime and energy are known to be insensitive to environment (namely its polarity)⁸⁰ but highly sensitive to conjugation length,⁷⁶ while the $S_0 \rightarrow S_2$ transition energy is sensitive to the polarizability of the environment.⁷⁴ Our results therefore suggest that the redshifted and blueshifted forms result from different CAN-protein microenvironments, rather than differences in CAN conjugation length.

This hypothesis can also be reconciled with the resonance Raman spectroscopy of Kish *et al.*¹² We previously assigned the reported 1527 cm^{-1} “shoulder” as due to the S^* -like form in CAN-OCPo, so both the redshifted and blueshifted forms would have a ν_1 wavenumber of 1518 cm^{-1} , within experimental tolerances. We note that the ν_1 wavenumber for carotenoids has only minor dependence on the microenvironment.^{12,74,79}

In the literature, similar heterogeneities to the ones we observe here have occasionally been assigned as due to differences in keto-carotenoid hydrogen-bonding to Tyr201 and Trp288,^{39,59} but as ZEA-OCP has no carbonyl group at carbon 4 yet still shows similar heterogeneity,³⁴ a pure hydrogen-bond-heterogeneity origin to the redshifted form and blueshifted form appears unlikely.⁴¹ Our hypothesis is supported by a recent theoretical study by Pigni *et al.* who modeled the CAN-OCP photoconversion. In their redshifted form,

the CAN β 1-ring still forms hydrogen-bonds to Tyr201 and Tyr288, but the protein environment is reorganized, giving a relatively planar CAN configuration with a different position for the β 2-ring within the NTD.⁴²

It is worth highlighting that multiple structural studies on dark-adapted OCP using X-ray crystallography have not observed inhomogeneity in carotenoid conformation. Such structural studies have been conducted on wild-type OCPo,^{3,4,24,41,44,81–83} mutant OCP,^{43,81} and various OCP homologs.^{84,85} It appears to counter the hypotheses above regarding the presence of multiple ground-state forms within CAN-OCPo due to distortions of the bound carotenoid. We can reconcile this by speculating that crystal packing and/or cryogenic temperatures used during data collection could artificially be responsible for preferentially adopting one ground-state OCPo geometry. This contrasts with our spectroscopic studies on dilute OCPo and OCPr in trehalose glass probed at room temperature, along with the aforementioned solution-based studies at room temperature, where heterogeneity is apparent.^{12,30,34,40,41,60}

In short, we have identified multiple ground-state forms within CAN-OCPo, three of the forms here dubbed “redshifted form”, “blueshifted form”, and “S*-like form”. By comparison to the OCP and carotenoid literature, we hypothesize that the redshifted and blueshifted forms arise due to minor distortions of CAN leading to different interactions between CAN and the protein. Meanwhile, the S*-like form is likely to be a consequence of the presence of short CAN-associated molecules.^{48,49} To determine the origin of the red- and blue-shifted forms, further experiments are required, such as transient vibrational spectroscopy.

Photoexcitation of OCPo in trehalose forms initial photoproducts, without completion of the cycle. We end the discussion by recalling that our transient absorption spectroscopy measurements were performed on OCPo in trehalose glass, a method used to prevent the full transition to OCPr (Figure 2). Despite the lack of full photoconversion, the transient absorption spectroscopy (Figure 3a,c) shows very similar features to those observed in OCPo buffer by us (Figure 3d) and in the literature.^{34,36} Inspection of the films

and individual transient absorption sweeps show that no permanent change is induced by laser excitation (aside from bleaching in high pump-fluence measurements; see Figure S16). Therefore the trehalose prevents the overall transition to OCP_r, yet the trehalose does not prevent the initial (pre-OCP_r) photoproducts from forming.

We do not assign identities (protein conformation, interactions such as hydrogen-bonds, *etc.*) of the initially formed photoproducts seen in our spectroscopic measurements. These identities are under active debate in the literature, with experimental work^{4,36,46} and theoretical studies^{13,42,45} generally suggesting a process involving rupture of the hydrogen-bonds between the β 1-ring carbonyl group and Tyr201/Tyr288, subsequent translocation of the carotenoid into the NTD, and final separation of the CTD and NTD, giving OCP_r. Some studies question whether the translocation occurs,²⁴ and a recent study suggested that carotenoid photoisomerization and subsequent structural rearrangements are the first events that occur, with hydrogen-bond breakage merely a secondary effect accompanying domain separation.⁴⁴ Our findings are consistent with initial photo-induced formation of a red-shifted chromophore that sits within a “compact” OCP_o-type protein structure, even with the full conversion to OCP_r (with associated domain separation) prevented by the trehalose.

Finally, we note that the use of trehalose to prevent photoconversion of OCP also offers easy and efficient use of material. We found that the sample could be stored at room temperature in the dark without degradation or photoconversion for weeks at a time, allowing us to perform multiple experiments on the same sample, thus saving both material and time (avoiding the need to prepare large volumes of (mutant) samples,^{33,35,39,43} setting up and cleaning the flow cell^{15,31,34,36,60} or cryogenically freezing the solution¹¹). The trehalose glass system is therefore a relatively straightforward, material-efficient, and artifact-mitigated method for spectroscopic studies of photoactive proteins.

Conclusions

We fabricated samples of canthaxanthin-binding inactive (OCPo) and active (OCP_r) forms of orange carotenoid protein (OCP) in trehalose glass. We found that formation of OCP_r is prevented in this matrix, enabling static and time-resolved photophysical characterization of using samples that are stable and material-efficient.

Our results clear up some confusion from the literature, showing that photoconversion is not correlated with an S*-like feature observed in transient absorption spectroscopy, but leave many questions unanswered: what is the origin of the wavelength-dependent photoconversion? Why are there different photoconversion timescales? Does the structural heterogeneity in OCP have a functional role in cyanobacteria, or is it just a spandrel? In either case, we highlight the importance, due to this heterogeneity, of pump wavelength dependence of the OCP photophysics.

Acknowledgement

The authors thank James D. Shipp and David G. Bossanyi for assistance with transient absorption measurements. The authors thank Andrew J. Musser, Daniel W. Polak and D.G.B. for their contributions to the nanosecond-millisecond transient absorption system.

Funding: J.P.P. thanks the EPSRC for support through a Doctoral Training Partnership Scholarship (EP/R513313/1) and through an Impact Acceleration Account (EP/X525790/1). G.A.S. and C.N.H. acknowledge ERC Synergy Grant 854126. The authors thank the EPSRC for a Capital Equipment Award (EP/L022613/1 and EP/R042802/1) which funded the Lord Porter Laser facility used in this study. J.C., C.N.H, G.A.S. and S.W. thank the EPSRC for funding through EP/S002103/1. J.P.P., J.C., R.J. and R.K.V. thank the EPSRC for funding through EP/T012455/1. J.C. and S.W. also thank the EPSRC for funding through EP/N014022/1. S.B. thanks the EPSRC for support through EP/R045305/1. M.S.P. and M.P.J. were supported by Leverhulme Trust award RPG-2019-

045. A.H. acknowledges support of a Royal Society University Research Fellowship (award URF\R1\191548).

Author contributions: J.P.P. and G.A.S. conceived the study. J.P.P., G.A.S., S.W., R.J. and J.C. designed the experiments. G.A.S., M.S.P. and A.H. prepared protein samples under the supervision of M.P.J. and C.N.H. The absorbance measurements in Figures 1a and 2 were performed by G.A.S. Transient absorption was conducted by J.P.P. and S.W. within the Lord Porter Laser Facility, with S.B. assisting and D.C. providing facility management. S.B. finalized construction of the nanosecond-millisecond transient absorption system. J.P.P. and R.J. conducted the narrowband-pump time-resolved absorbance experiments. J.P.P. and G.A.S. analyzed the data. R.K.V. assisted with the literature review. J.P.P., G.A.S. and J.C. wrote the manuscript and prepared the figures with input from all authors.

Supporting Information Available

- **Supplementary Information (SI):** Literature review clarifying our current understanding of S^* in carotenoids and OCP; experimental methods, including canthaxanthin-binding OCP production, OCPo and OCPr in sugar glasses preparation, spectroscopic setups, beam characterization methods, and data analysis procedures; supplementary visible/NIR picosecond transient absorption materials, including pump spectra, 485 nm pump measurements on OCPo and OCPr, and the results of global lifetime analysis; supplementary nanosecond-millisecond transient absorption materials, including the results of global lifetime analysis on OCPo in trehalose and buffer; image of encapsulated OCPo with bleaching but no conversion after high-fluence measurements; supplementary UV-vis picosecond transient absorption materials, including pump spectra, replicate measurements at the same nominal pump fluence, measurements demonstrating pump fluence independence, fit parameters for the global fit of dynamics, and the

results of global target analysis; further details on time-resolved absorbance, including the global fit of difference dynamics and about the experimental oversights.

- Data will be available on the University of Sheffield’s repository, ORDA, once the paper has been accepted for publication.

References

- (1) van Thor, J. J.; Mullineaux, C. W.; Matthijs, H. C. P.; Hellingwerf, K. J. Light Harvesting and State Transitions in Cyanobacteria. *Botanica Acta* **1998**, *111*, 430–443.
- (2) Mullineaux, C. W. State Transitions: An Example of Acclimation to Low-Light Stress. *J. Exp. Bot.* **2005**, *56*, 389–393.
- (3) Kerfeld, C. A.; Sawaya, M. R.; Brahmandam, V.; Cascio, D.; Ho, K. K.; Trevithick-Sutton, C. C.; Krogmann, D. W.; Yeates, T. O. The Crystal Structure of a Cyanobacterial Water-Soluble Carotenoid Binding Protein. *Structure* **2003**, *11*, 55–65.
- (4) Leverenz, R. L.; Sutter, M.; Wilson, A.; Gupta, S.; Thurotte, A.; Bourcier de Carbon, C.; Petzold, C. J.; Ralston, C.; Perreau, F.; Kirilovsky, D.; Kerfeld, C. A. A 12 Å Carotenoid Translocation in a Photoswitch Associated with Cyanobacterial Photoprotection. *Science* **2015**, *348*, 1463–1466.
- (5) Gupta, S.; Guttman, M.; Leverenz, R. L.; Zhumadilova, K.; Pawlowski, E. G.; Petzold, C. J.; Lee, K. K.; Ralston, C. Y.; Kerfeld, C. A. Local and Global Structural Drivers for the Photoactivation of the Orange Carotenoid Protein. *Proc. Natl. Acad. Sci. U.S.A.* **2015**, *112*, E5567–E5574.
- (6) Domínguez-Martín, M. A.; Sauer, P. V.; Kirst, H.; Sutter, M.; Bína, D.; Greber, B. J.; Nogales, E.; Polívka, T.; Kerfeld, C. A. Structures of a Phycobilisome in Light-Harvesting and Photoprotected States. *Nature* **2022**,

- (7) Kirilovsky, D. Photoprotection in Cyanobacteria: The Orange Carotenoid Protein (OCP)-Related Non-Photochemical-Quenching Mechanism. *Photosynth. Res.* **2007**, *93*, 7–16.
- (8) Tian, L.; Gwizdala, M.; van Stokkum, I. H.; Koehorst, R. B.; Kirilovsky, D.; van Amerongen, H. Picosecond Kinetics of Light Harvesting and Photoprotective Quenching in Wild-Type and Mutant Phycobilisomes Isolated from the Cyanobacterium *Synechocystis* PCC 6803. *Biophys. J.* **2012**, *102*, 1692–1700.
- (9) Kirilovsky, D.; Kerfeld, C. A. Cyanobacterial Photoprotection by the Orange Carotenoid Protein. *Nat. Plants* **2016**, *2*, 16180.
- (10) Wilson, A.; Punginelli, C.; Gall, A.; Bonetti, C.; Alexandre, M.; Routaboul, J.-M.; Kerfeld, C. A.; van Grondelle, R.; Robert, B.; Kennis, J. T. M.; Kirilovsky, D. A Photoactive Carotenoid Protein Acting as Light Intensity Sensor. *Proc. Natl. Acad. Sci. U.S.A.* **2008**, *105*, 12075–12080.
- (11) Niedzwiedzki, D. M.; Liu, H.; Blankenship, R. E. Excited State Properties of 3*H*-Hydroxyechinenone in Solvents and in the Orange Carotenoid Protein from *Synechocystis* sp. PCC 6803. *J. Phys. Chem. B* **2014**, *118*, 6141–6149.
- (12) Kish, E.; Pinto, M. M. M.; Kirilovsky, D.; Spezia, R.; Robert, B. Echinenone Vibrational Properties: From Solvents to the Orange Carotenoid Protein. *Biochim. Biophys. Acta, Bioenerg.* **2015**, *1847*, 1044–1054.
- (13) Bondanza, M.; Cupellini, L.; Faccioli, P.; Mennucci, B. Molecular Mechanisms of Activation in the Orange Carotenoid Protein Revealed by Molecular Dynamics. *J. Am. Chem. Soc.* **2020**, *142*, 21829–21841.
- (14) Tian, L.; van Stokkum, I. H. M.; Koehorst, R. B. M.; Jongerius, A.; Kirilovsky, D.; van Amerongen, H. Site, Rate, and Mechanism of Photoprotective Quenching in Cyanobacteria. *J. Am. Chem. Soc.* **2011**, *133*, 18304–18311.

- (15) Berera, R.; van Stokkum, I. H. M.; Gwizdala, M.; Wilson, A.; Kirilovsky, D.; van Grondelle, R. The Photophysics of the Orange Carotenoid Protein, a Light-Powered Molecular Switch. *J. Phys. Chem. B* **2012**, *116*, 2568–2574.
- (16) Niyogi, K. K.; Bjorkman, O.; Grossman, A. R. The Roles of Specific Xanthophylls in Photoprotection. *Proc. Natl. Acad. Sci. U.S.A.* **1997**, *94*, 14162–14167.
- (17) Pascal, A. A.; Liu, Z.; Broess, K.; van Oort, B.; van Amerongen, H.; Wang, C.; Horton, P.; Robert, B.; Chang, W.; Ruban, A. Molecular Basis of Photoprotection and Control of Photosynthetic Light-Harvesting. *Nature* **2005**, *436*, 134–137.
- (18) Harris, D.; Tal, O.; Jallet, D.; Wilson, A.; Kirilovsky, D.; Adir, N. Orange Carotenoid Protein Burrows into the Phycobilisome to Provide Photoprotection. *Proc. Natl. Acad. Sci. U.S.A.* **2016**, *113*, E1655–E1662.
- (19) Squires, A. H.; Dahlberg, P. D.; Liu, H.; Magdaong, N. C. M.; Blankenship, R. E.; Moerner, W. E. Single-Molecule Trapping and Spectroscopy Reveals Photophysical Heterogeneity of Phycobilisomes Quenched by Orange Carotenoid Protein. *Nat. Commun.* **2019**, *10*, 1172.
- (20) Lou, W.; Niedzwiedzki, D. M.; Jiang, R. J.; Blankenship, R. E.; Liu, H. Binding of Red Form of Orange Carotenoid Protein (OCP) to Phycobilisome Is Not Sufficient for Quenching. *Biochim. Biophys. Acta, Bioenerg.* **2020**, *1861*, 148155.
- (21) Maksimov, E. G.; Li, W.-J.; Protasova, E. A.; Friedrich, T.; Ge, B.; Qin, S.; Sluchanko, N. N. Hybrid Coupling of R-Phycoerythrin and the Orange Carotenoid Protein Supports the FRET-Based Mechanism of Cyanobacterial Photoprotection. *Biochem. Biophys. Res. Commun.* **2019**, *516*, 699–704.
- (22) Krasilnikov, P. M.; Zlenko, D. V.; Stadnichuk, I. N. Rates and Pathways of Energy Migration from the Phycobilisome to the Photosystem II and to the Orange Carotenoid Protein in Cyanobacteria. *FEBS Lett.* **2020**, *594*, 1145–1154.

- (23) Wilson, A.; Muzzopappa, F.; Kirilovsky, D. Elucidation of the Essential Amino Acids Involved in the Binding of the Cyanobacterial Orange Carotenoid Protein to the Phycobilisome. *Biochim. Biophys. Acta, Bioenerg.* **2022**, *1863*, 148504.
- (24) Bandara, S.; Ren, Z.; Lu, L.; Zeng, X.; Shin, H.; Zhao, K.-H.; Yang, X. Photoactivation Mechanism of a Carotenoid-Based Photoreceptor. *Proc. Natl. Acad. Sci. U.S.A.* **2017**, *114*, 6286–6291.
- (25) Lutz, I.; Sieg, A.; Wegener, A. A.; Engelhard, M.; Boche, I.; Otsuka, M.; Oesterhelt, D.; Wachtveitl, J.; Zinth, W. Primary Reactions of Sensory Rhodopsins. *Proc. Natl. Acad. Sci. U.S.A.* **2001**, *98*, 962–967.
- (26) Yang, X.; Ren, Z.; Kuk, J.; Moffat, K. Temperature-Scan Cryocrystallography Reveals Reaction Intermediates in Bacteriophytochrome. *Nature* **2011**, *479*, 428–432.
- (27) Kerfeld, C. A.; Melnicki, M. R.; Sutter, M.; Dominguez-Martin, M. A. Structure, Function and Evolution of the Cyanobacterial Orange Carotenoid Protein and Its Homologs. *New Phytol.* **2017**, *215*, 937–951.
- (28) Piccinini, L.; Iacopino, S.; Cazzaniga, S.; Ballottari, M.; Giuntoli, B.; Licausi, F. A Synthetic Switch Based on Orange Carotenoid Protein to Control Blue–Green Light Responses in Chloroplasts. *Plant Physiol.* **2022**, *189*, 1153–1168.
- (29) Dominguez-Martin, M. A.; Kerfeld, C. A. Engineering the Orange Carotenoid Protein for Applications in Synthetic Biology. *Curr. Opin. Struct. Biol.* **2019**, *57*, 110–117.
- (30) Polívka, T.; Chábera, P.; Kerfeld, C. A. Carotenoid–Protein Interaction Alters the S₁ Energy of Hydroxyechinenone in the Orange Carotenoid Protein. *Biochim. Biophys. Acta, Bioenerg.* **2013**, *1827*, 248–254.
- (31) Berera, R.; Gwizdala, M.; van Stokkum, I. H. M.; Kirilovsky, D.; van Grondelle, R.

- Excited States of the Inactive and Active Forms of the Orange Carotenoid Protein. *J. Phys. Chem. B* **2013**, *117*, 9121–9128.
- (32) De Re, E.; Schlau-Cohen, G. S.; Leverenz, R. L.; Huxter, V. M.; Oliver, T. A. A.; Mathies, R. A.; Fleming, G. R. Insights into the Structural Changes Occurring upon Photoconversion in the Orange Carotenoid Protein from Broadband Two-Dimensional Electronic Spectroscopy. *J. Phys. Chem. B* **2014**, *118*, 5382–5389.
- (33) Maksimov, E. G.; Shirshin, E. A.; Sluchanko, N. N.; Zlenko, D. V.; Parshina, E. Y.; Tsoraev, G. V.; Klementiev, K. E.; Budylin, G. S.; Schmitt, F.-J.; Friedrich, T.; Fadeev, V. V.; Paschenko, V. Z.; Rubin, A. B. The Signaling State of Orange Carotenoid Protein. *Biophys. J.* **2015**, *109*, 595–607.
- (34) Šlouf, V.; Kuznetsova, V.; Fuciman, M.; de Carbon, C. B.; Wilson, A.; Kirilovsky, D.; Polívka, T. Ultrafast Spectroscopy Tracks Carotenoid Configurations in the Orange and Red Carotenoid Proteins from Cyanobacteria. *Photosynth. Res.* **2017**, *131*, 105–117.
- (35) Maksimov, E. G.; Sluchanko, N. N.; Slonimskiy, Y. B.; Slutsкая, E. A.; Stepanov, A. V.; Argentova-Stevens, A. M.; Shirshin, E. A.; Tsoraev, G. V.; Klementiev, K. E.; Slatinskaya, O. V.; Lukashev, E. P.; Friedrich, T.; Paschenko, V. Z.; Rubin, A. B. The Photocycle of Orange Carotenoid Protein Conceals Distinct Intermediates and Asynchronous Changes in the Carotenoid and Protein Components. *Sci. Rep.* **2017**, *7*, 15548.
- (36) Konold, P. E.; van Stokkum, I. H. M.; Muzzopappa, F.; Wilson, A.; Groot, M.-L.; Kirilovsky, D.; Kennis, J. T. M. Photoactivation Mechanism, Timing of Protein Secondary Structure Dynamics and Carotenoid Translocation in the Orange Carotenoid Protein. *J. Am. Chem. Soc.* **2019**, *141*, 520–530.
- (37) Pishchalnikov, R. Y.; Yaroshevich, I. A.; Slastnikova, T. A.; Ashikhmin, A. A.; Stepanov, A. V.; Slutsкая, E. A.; Friedrich, T.; Sluchanko, N. N.; Maksimov, E. G.

- Structural Peculiarities of Keto-Carotenoids in Water-Soluble Proteins Revealed by Simulation of Linear Absorption. *Phys. Chem. Chem. Phys.* **2019**, *21*, 25707–25719.
- (38) Wei, T.; Balevičius, V.; Polívka, T.; Ruban, A. V.; Duffy, C. D. P. How Carotenoid Distortions May Determine Optical Properties: Lessons from the Orange Carotenoid Protein. *Phys. Chem. Chem. Phys.* **2019**, *21*, 23187–23197.
- (39) Maksimov, E. G.; Protasova, E. A.; Tsoraev, G. V.; Yaroshevich, I. A.; Maydykovskiy, A. I.; Shirshin, E. A.; Gostev, T. S.; Jelzow, A.; Moldenhauer, M.; Slonimskiy, Y. B.; Sluchanko, N. N.; Friedrich, T. Probing of Carotenoid-Tryptophan Hydrogen Bonding Dynamics in the Single-Tryptophan Photoactive Orange Carotenoid Protein. *Sci. Rep.* **2020**, *10*, 11729.
- (40) Khan, T.; Dominguez-Martin, M. A.; Šímová, I.; Fuciman, M.; Kerfeld, C. A.; Polívka, T. Excited-State Properties of Canthaxanthin in Cyanobacterial Carotenoid-Binding Proteins HCP2 and HCP3. *J. Phys. Chem. B* **2020**, *124*, 4896–4905.
- (41) Kuznetsova, V.; Dominguez-Martin, M. A.; Bao, H.; Gupta, S.; Sutter, M.; Kloz, M.; Rebarz, M.; Přeček, M.; Chen, Y.; Petzold, C. J.; Ralston, C. Y.; Kerfeld, C. A.; Polívka, T. Comparative Ultrafast Spectroscopy and Structural Analysis of OCP1 and OCP2 from *Tolypothrix*. *Biochim. Biophys. Acta, Bioenerg.* **2020**, *1861*, 148120.
- (42) Pigni, N. B.; Clark, K. L.; Beck, W. F.; Gascón, J. A. Spectral Signatures of Canthaxanthin Translocation in the Orange Carotenoid Protein. *J. Phys. Chem. B* **2020**, *124*, 11387–11395.
- (43) Yaroshevich, I. A. et al. Role of Hydrogen Bond Alternation and Charge Transfer States in Photoactivation of the Orange Carotenoid Protein. *Commun. Biol.* **2021**, *4*, 539.
- (44) Chukhutsina, V. U.; Baxter, J. M.; Fadini, A.; Morgan, R. M.; Pope, M. A.; Maghlaoui, K.; Orr, C. M.; Wagner, A.; van Thor, J. J. Light Activation of Orange Carotenoid

- Protein Reveals Bicycle-Pedal Single-Bond Isomerization. *Nat. Commun.* **2022**, *13*, 6420.
- (45) Bondanza, M.; Cupellini, L.; Lipparini, F.; Mennucci, B. The Multiple Roles of the Protein in the Photoactivation of Orange Carotenoid Protein. *Chem* **2020**, *6*, 187–203.
- (46) Gupta, S.; Sutter, M.; Remesh, S. G.; Dominguez-Martin, M. A.; Bao, H.; Feng, X. A.; Chan, L.-J. G.; Petzold, C. J.; Kerfeld, C. A.; Ralston, C. Y. X-Ray Radiolytic Labeling Reveals the Molecular Basis of Orange Carotenoid Protein Photoprotection and Its Interactions with Fluorescence Recovery Protein. *J. Biol. Chem.* **2019**, *294*, 8848–8860.
- (47) Polívka, T.; Sundström, V. Dark Excited States of Carotenoids: Consensus and Controversy. *Chem. Phys. Lett.* **2009**, *477*, 1–11.
- (48) Ostroumov, E. E.; Reus, M. G. M., Michael; Holzwarth, A. R. On the Nature of the “Dark S*” Excited State of β -Carotene. *J. Phys. Chem. A* **2011**, *115*, 3698–3712.
- (49) Polak, D. W.; Musser, A. J.; Sutherland, G. A.; Auty, A.; Branchi, F.; Dzurnak, B.; Chidgey, J.; Cerullo, G.; Hunter, C. N.; Clark, J. Band-Edge Excitation of Carotenoids Removes S* Revealing Triplet-Pair Contributions to the S₁ Absorption Spectrum. *arXiv preprint* **2019**, arXiv:1901.04900.
- (50) Šebelík, V.; Duffy, C. D. P.; Keil, E.; Polívka, T.; Hauer, J. Understanding Carotenoid Dynamics via the Vibronic Energy Relaxation Approach. *J. Phys. Chem. B* **2022**, *126*, 3985–3994.
- (51) Niedzwiedzki, D. M.; Swainsbury, D. J. K.; Martin, E. C.; Hunter, C. N.; Blankenship, R. E. Origin of the S* Excited State Feature of Carotenoids in Light-Harvesting Complex 1 from Purple Photosynthetic Bacteria. *J. Phys. Chem. B* **2017**, *121*, 7571–7585.

- (52) Kloz, M.; Weißenborn, J.; Polívka, T.; Frank, H. A.; Kennis, J. T. M. Spectral Water-marking in Femtosecond Stimulated Raman Spectroscopy: Resolving the Nature of the Carotenoid S* State. *Phys. Chem. Chem. Phys.* **2016**, *18*, 14619–14628.
- (53) Niedzwiedzki, D.; Kosciielecki, J. F.; Cong, H.; Sullivan, J. O.; Gibson, G. N.; Birge, R. R.; Frank, H. A. Ultrafast Dynamics and Excited State Spectra of Open-Chain Carotenoids at Room and Low Temperatures. *J. Phys. Chem. B* **2007**, *111*, 5984–5998.
- (54) Kolano, C.; Helbing, J.; Kozinski, M.; Sander, W.; Hamm, P. Watching Hydrogen-Bond Dynamics in a β -Turn by Transient Two-Dimensional Infrared Spectroscopy. *Nature* **2006**, *444*, 469–472.
- (55) Balevičius, V.; Pour, A. G.; Savolainen, J.; Lincoln, C. N.; Lukeš, V.; Riedle, E.; Valkunas, L.; Abramavicius, D.; Hauer, J. Vibronic Energy Relaxation Approach Highlighting Deactivation Pathways in Carotenoids. *Phys. Chem. Chem. Phys.* **2015**, *17*, 19491–19499.
- (56) Balevičius, V.; Abramavicius, D.; Polívka, T.; Galestian Pour, A.; Hauer, J. A Unified Picture of S* in Carotenoids. *J. Phys. Chem. Lett.* **2016**, *7*, 3347–3352.
- (57) Balevičius, V.; Lincoln, C. N.; Viola, D.; Cerullo, G.; Hauer, J.; Abramavicius, D. Effects of Tunable Excitation in Carotenoids Explained by the Vibrational Energy Relaxation Approach. *Photosynth. Res.* **2018**, *135*, 55–64.
- (58) Balevičius, V.; Wei, T.; Di Tommaso, D.; Abramavicius, D.; Hauer, J.; Polívka, T.; Duffy, C. D. P. The Full Dynamics of Energy Relaxation in Large Organic Molecules: From Photo-Excitation to Solvent Heating. *Chem. Sci.* **2019**, *10*, 4792–4804.
- (59) Polívka, T.; Kerfeld, C. A.; Pascher, T.; Sundström, V. Spectroscopic Properties of the Carotenoid 3*H*-Hydroxyechinenone in the Orange Carotenoid Protein from the Cyanobacterium *Arthrospira maxima*. *Biochemistry* **2005**, *44*, 3994–4003.

- (60) Niziński, S.; Wilson, A.; Uriarte, L. M.; Ruckebusch, C.; Andreeva, E. A.; Schlichting, I.; Colletier, J.-P.; Kirilovsky, D.; Burdzinski, G.; Sliwa, M. Unifying Perspective of the Ultrafast Photodynamics of Orange Carotenoid Proteins from *Synechocystis*: Peril of High-Power Excitation, Existence of Different S* States, and Influence of Tagging. *JACS Au* **2022**, *2*, 1084–1095.
- (61) Arcidiacono, A.; Accomasso, D.; Cupellini, L.; Mennucci, B. How Orange Carotenoid Protein Controls the Excited State Dynamics of Canthaxanthin. *ChemRxiv preprint* **2023**, DOI:10.26434/chemrxiv-2023-bd7r6.
- (62) Polgár, A.; Zechmeister, L. Isomerization of β -Carotene. Isolation of a Stereoisomer with Increased Adsorption Affinity. *J. Am. Chem. Soc.* **1942**, *64*, 1856–1861.
- (63) Zechmeister, L. *Cis-Trans* Isomerization and Stereochemistry of Carotenoids and Diphenylpolyenes. *Chem. Rev.* **1944**, *34*, 267–344.
- (64) Pesek, C. A.; Warthesen, J. J. Kinetic Model for Photoisomerization and Concomitant Photodegradation of β -Carotenes. *J. Agric. Food Chem.* **1990**, *38*, 1313–1315.
- (65) Jain, N. K.; Roy, I. Effect of Trehalose on Protein Structure. *Protein Sci.* **2009**, *18*, 24–36.
- (66) Kurashov, V.; Gorika, M.; Milanovsky, G. E.; Johnson, T. W.; Cherepanov, D. A.; Semenov, A. Y.; Golbeck, J. H. Critical Evaluation of Electron Transfer Kinetics in P700–FA/FB, P700–FX, and P700–A1 Photosystem I Core Complexes in Liquid and in Trehalose Glass. *Biochim. Biophys. Acta, Bioenerg.* **2018**, *1859*, 1288–1301.
- (67) Sutherland, G. A.; Polak, D.; Swainsbury, D. J. K.; Wang, S.; Spano, F. C.; Auman, D. B.; Bossanyi, D. G.; Pidgeon, J. P.; Hitchcock, A.; Musser, A. J.; Anthony, J. E.; Dutton, P. L.; Clark, J.; Hunter, C. N. A Thermostable Protein Matrix for Spectroscopic Analysis of Organic Semiconductors. *J. Am. Chem. Soc.* **2020**, *142*, 13898–13907.

- (68) Sutherland, G. A.; Pidgeon, J. P.; Lee, H. K. H.; Proctor, M. S.; Hitchcock, A.; Wang, S.; Chekulaev, D.; Tsoi, W. C.; Johnson, M. P.; Hunter, C. N.; Clark, J. Twisted Carotenoids Do Not Support Efficient Intramolecular Singlet Fission in the Orange Carotenoid Protein. *J. Phys. Chem. Lett.* **2023**, *14*, 6135–6142.
- (69) Cunningham, F. X.; Gantt, E. A Portfolio of Plasmids for Identification and Analysis of Carotenoid Pathway Enzymes: *Adonis aestivalis* as a Case Study. *Photosynth. Res.* **2007**, *92*, 245–259.
- (70) Nielsen, B. R.; Mortensen, A.; Jørgensen, K.; Skibsted, L. H. Singlet *versus* Triplet Reactivity in Photodegradation of C₄₀ Carotenoids. *J. Agric. Food Chem.* **1996**, *44*, 2106–2113.
- (71) Khan, T.; Kuznetsova, V.; Dominguez-Martin, M. A.; Kerfeld, C. A.; Polívka, T. UV Excitation of Carotenoid Binding Proteins OCP and HCP: Excited-State Dynamics and Product Formation. *ChemPhotoChem* **2022**, *6*, e202100194.
- (72) Rose, J. B.; Gascón, J. A.; Sutter, M.; Sheppard, D. I.; Kerfeld, C. A.; Beck, W. F. Photoactivation of the Orange Carotenoid Protein Requires Two Light-Driven Reactions Mediated by a Metastable Monomeric Intermediate. *Phys. Chem. Chem. Phys.* **2023**, *25*, 33000–33012.
- (73) Niziński, S.; Schlichting, I.; Colletier, J.-P.; Kirilovsky, D.; Burdzinski, G.; Sliwa, M. Is Orange Carotenoid Protein Photoactivation a Single-Photon Process? *Biophys. Rep.* **2022**, 100072.
- (74) Llansola-Portoles, M. J.; Pascal, A. A.; Robert, B. Electronic and Vibrational Properties of Carotenoids: From *in Vitro* to *in Vivo*. *J. R. Soc. Interface.* **2017**, *14*, 20170504.
- (75) Fuciman, M.; Keşan, G.; LaFountain, A. M.; Frank, H. A.; Polívka, T. Tuning the Spectroscopic Properties of Aryl Carotenoids by Slight Changes in Structure. *J. Phys. Chem. B* **2015**, *119*, 1457–1467.

- (76) Chynwat, V.; Frank, H. A. The Application of the Energy Gap Law to the S₁ Energies and Dynamics of Carotenoids. *Chem. Phys.* **1995**, *194*, 237–244.
- (77) Fujii, R.; Onaka, K.; Kuki, M.; Koyama, Y.; Watanabe, Y. The 2Ag⁻ Energies of All-Trans-Neurosporene and Spheroidene as Determined by Fluorescence Spectroscopy. *Chem. Phys. Lett.* **1998**, *288*, 847–853.
- (78) Koyama, Y.; Fujii, R. In *The Photochemistry of Carotenoids*; Frank, H. A., Young, A. J., Britton, G., Cogdell, R. J., Eds.; Springer Netherlands: Dordrecht, 1999; Vol. 8; pp 161–188.
- (79) Mendes-Pinto, M. M.; Sansiaume, E.; Hashimoto, H.; Pascal, A. A.; Gall, A.; Robert, B. Electronic Absorption and Ground State Structure of Carotenoid Molecules. *J. Phys. Chem. B* **2013**, *117*, 11015–11021.
- (80) Bondarev, S.; Knyukshto, V. Fluorescence from the S₁ (2¹Ag) State of All-Trans-β-Carotene. *Chem. Phys. Lett.* **1994**, *225*, 346–350.
- (81) Wilson, A.; Kinney, J. N.; Zwart, P. H.; Punginelli, C.; D’Haene, S.; Perreau, F.; Klein, M. G.; Kirilovsky, D.; Kerfeld, C. A. Structural Determinants Underlying Photoprotection in the Photoactive Orange Carotenoid Protein of Cyanobacteria. *J. Biol. Chem.* **2010**, *285*, 18364–18375.
- (82) López-Igual, R.; Wilson, A.; Leverenz, R. L.; Melnicki, M. R.; Bourcier de Carbon, C.; Sutter, M.; Turmo, A.; Perreau, F.; Kerfeld, C. A.; Kirilovsky, D. Different Functions of the Paralogs to the N-Terminal Domain of the Orange Carotenoid Protein in the Cyanobacterium *Anabaena* Sp. PCC 7120. *Plant Physiol.* **2016**, *171*, 1852–1866.
- (83) Wilson, A.; Andreeva, E. A.; Niziński, S.; Talbot, L.; Hartmann, E.; Schlichting, I.; Burdzinski, G.; Sliwa, M.; Kirilovsky, D.; Colletier, J.-P. Structure-Function-Dynamics Relationships in the Peculiar *Planktothrix* PCC7805 OCP1: Impact of His-Tagging and Carotenoid Type. *Biochim. Biophys. Acta, Bioenerg.* **2022**, *1863*, 148584.

- (84) Dominguez-Martin, M. A.; Polívka, T.; Sutter, M.; Ferlez, B.; Lechno-Yossef, S.; Montgomery, B. L.; Kerfeld, C. A. Structural and Spectroscopic Characterization of HCP2. *Biochim. Biophys. Acta, Bioenerg.* **2019**, *1860*, 414–424.
- (85) Melnicki, M. R.; Leverenz, R. L.; Sutter, M.; López-Igual, R.; Wilson, A.; Pawlowski, E. G.; Perreau, F.; Kirilovsky, D.; Kerfeld, C. A. Structure, Diversity, and Evolution of a New Family of Soluble Carotenoid-Binding Proteins in Cyanobacteria. *Mol. Plant* **2016**, *9*, 1379–1394.
- (86) Snellenburg, J.; Laptенок, S.; Seger, R.; Mullen, K. Glotaran: A Java-Based Graphical User Interface for the R Package TIMP. *J. Stat. Softw.* **2012**, *49*.
- (87) Mullen, K. M.; van Stokkum, I. H. M. TIMP: An R Package for Modeling Multi-Way Spectroscopic Measurements. *J. Stat. Softw.* **2007**, *18*, 1–46.
- (88) Berera, R.; van Grondelle, R.; Kennis, J. T. M. Ultrafast Transient Absorption Spectroscopy: Principles and Application to Photosynthetic Systems. *Photosynth. Res.* **2009**, *101*, 105–118.
- (89) Ruckebusch, C.; Sliwa, M.; Pernot, P.; de Juan, A.; Tauler, R. Comprehensive Data Analysis of Femtosecond Transient Absorption Spectra: A Review. *J. Photochem. Photobiol., C* **2012**, *13*, 1–27.
- (90) van Stokkum, I. H.; Larsen, D. S.; van Grondelle, R. Global and Target Analysis of Time-Resolved Spectra. *Biochim. Biophys. Acta, Bioenerg.* **2004**, *1657*, 82–104.
- (91) Fernández-Terán, R. J.; Sucre-Rosales, E.; Echevarria, L.; Hernández, F. E. A Sweet Introduction to the Mathematical Analysis of Time-Resolved Spectra and Complex Kinetic Mechanisms: The Chameleon Reaction Revisited. *J. Chem. Educ.* **2022**, *99*, 2327–2337.

- (92) Lakowicz, J. R. *Principles of Fluorescence Spectroscopy*, 3rd ed.; Springer: New York, 2006.

Supplementary Information

S1 Literature review on S* in carotenoids and OCP

We start our discussion with a description of S* as a generic spectral feature without assigning it to any distinct excited-state or process at this point. S* is a catch-all term for a excited-state absorption (ESA) spectral feature located at the red edge of the S₀→S₂ ground-state bleach (GSB), and distinct from the main singlet S₁ ESA band.⁴⁷ The S* feature is typically weak (~1–5% of the S₁→S_n absorption intensity) with a long lifetime (~20–100 ps) compared to the S₁ absorption features. The S* feature is sometimes also associated with narrowing of the GSB and often shows pump (excitation) wavelength-dependent behavior (it is relatively more intense with higher-energy excitation).^{48,49,60} This broad definition of the S* spectral feature and its location at the edge of the GSB, which can be prone to artifacts (because depositing energy into a system can lead to an increase in local temperature, resulting in changes in the sample’s refractive index and absorption spectrum in the probe region), means that S* has been assigned to a variety of different phenomena.^{47,48,50,51}

In OCP, Konold *et al.*, Ref.³⁶ suggest that the S* feature represents a key intermediate electronic excited state that drives the switch from OCPo to OCP_r. They hypothesize that S* is a structurally distorted form of the lowest singlet excited state in carotenoids,^{36,52,53} and that this distortion enables hydrogen-bond rupture between C=O and Trp288/Tyr201. A more recent study by Yaroshevich *et al.* supports the hypothesis that S* is a distinct excited state,⁴³ but suggests that it enables accumulation of intramolecular charge transfer (ICT) states which are themselves responsible for hydrogen-bond breaking.⁴³ In both of these pictures, hydrogen-bond rupture should occur during the S* lifetime, which was indeed reported in a tryptophan fluorescence study of an OCP mutant, where four Trp residues were mutated, allowing analysis of the crucial W288-carotenoid hydrogen bond interaction (the one involved in hydrogen-bonding to C=O).³⁹ However, hydrogen-bond breaking should also be observable through shifts in the transient mid-infrared or UV-vis absorption spectra;

either as a blue-shifted ESA of the C=O band,⁵⁴ or as a ESA to the blue-edge of the GSB in UV-vis transient absorption spectroscopy.⁴³ To our knowledge, neither of these features have been observed on the S* timescale (~ 20 – 100 ps), although it is possible that these features are simply outside of the measured spectral ranges³⁶ or obscured by other spectral features. In addition, a more recent study by Chukhutsina *et al.*, using time-resolved crystallography and optical spectroscopy suggests that the hydrogen-bond breakage occurs on 5–10 min timescales, and not during the S* lifetime, and is merely as a consequence of N- and C-terminal domain separation.⁴⁴

Other research by Balevičius *et al.* supports the hypothesis that observation of an S* feature in visible transient absorption spectroscopy is key to understanding the trigger to photoswitching in OCP.⁵⁸ However, Balevičius’ study on carotenoids in solvent, together with earlier work,^{55–57} suggest that the S* spectral feature is not an excited-state signature, but instead arises due to transient heating of the carotenoid and solvent during and immediately following internal conversion.⁵⁸ Internal conversion in carotenoids is incredibly rapid and most of the energy deposited into OCP by light (~ 2 eV) is converted into vibrational or kinetic energy within ~ 100 fs to 20 ps through intramolecular vibrational redistribution (IVR) and vibrational cooling (VC) to the surroundings. IVR and VC populate both higher-lying vibronic levels ($\nu \geq 1$) in the ground (S₀) and excited (S₁) electronic states^{55–57} and cause local heating in the form of population of low-energy molecular, solvent, or protein vibrational/rotational modes. Both of these result in transient spectral features in the GSB spectral region which could be assigned to S*.^{50,55–58} From these carotenoid-in-solution studies, Balevičius *et al.*⁵⁸ suggested that the S* feature seen in OCP by Konold *et al.*³⁶ was consistent with a residual “hot ground state”, associated with a non-equilibrium distribution of carotenoid vibronic populations as well as elevated local temperature (rather than a distinct excited state), that may provide enough energy to break the weak hydrogen-bonds⁵⁸ (estimated to have a bond energy of ~ 8 kcal mol⁻¹ or 0.35 eV per molecule⁴³).

Still others claim that the S* feature in transient absorption spectroscopy is not due to an

intermediate excited state, or due to heating, but is instead due to inhomogeneity of the sample. The inhomogeneity is observed as a pump wavelength-dependent change in resonance Raman¹² and transient absorption spectra^{30,34,40,41,60} and is usually attributed to carotenoid conformational inhomogeneity as the carotenoid adopts more than one conformation in the ground-state,^{12,34,37,41,61} possibly due to spontaneous hydrogen-bond disruption.³⁹ This spectral heterogeneity has been observed in OCPo binding 3'-hydroxyechinenone (3'hECN),^{30,59} echinenone (ECN),^{12,34,37,60} canthaxanthin (CAN)^{34,61} and zeaxanthin (ZEA),³⁴ in N-terminal domain helical carotenoid proteins (HCP) HCP2 and HCP3 containing CAN,⁴⁰ and in the non-canonical OCP2 clade.⁴¹

The hypothesis that the pump wavelength dependence of OCP spectral features is due to conformational heterogeneity of the carotenoid has basis in studies of isolated carotenoid in solution.^{48,49,62-64} For example, an important study by Ostroumov *et al.*⁴⁸ demonstrated that the pump wavelength dependence could be removed by purifying β -carotene immediately prior to measurement. The resulting transient absorption spectra of all-*trans* β -carotene showed no sign of the putative S* spectral feature. While the aforementioned transient heating due to rapid internal conversion is also predicted to show some pump wavelength dependence,⁵⁷ the effect is small and short-lived, and cannot on its own explain the sometimes dramatic changes in transient absorption spectra in relation to pump wavelength.⁴⁹

The literature places great emphasis on the S* feature because it is widely believed to be directly correlated with the first steps of the photoconversion mechanism of OCP.^{36,39,43} We find that the evidence for this key assumption is largely circumstantial and requires further scrutiny. Therefore, in the main paper, we aim to test the hypothesis that the S* spectral feature is directly correlated with photoconversion.

S2 Methods

S2.1 Sample preparation

OCP binding near-100% CAN was produced using the same method to that in previous work.⁶⁸ CAN-OCP from BL21(DE3) *Escherichia coli* (*E. coli*) using a dual-plasmid system comprised of pAC-CANTH_{ip}⁶⁹ and pET28a containing the gene encoding OCP (slr1963) from *Synechocystis* sp. PCC 6803. Briefly, 500 mL cultures were grown at 37 °C (200 rev min⁻¹ agitation) in 2 L baffled Erlenmeyer flasks using lysogeny broth medium containing the appropriate concentrations of antibiotics. When the absorbance of the medium at 600 nm had reached $A_{600} = 0.6$ (1 cm path length), protein production was induced by addition of 0.5 mM isopropyl β -D-1-thiogalactopyranoside and the cultures incubated for 16 hours at 18 °C.

Cells were harvested by centrifugation (4,400 $\times g$, 30 min, 4 °C) and resuspended in binding buffer (50 mM HEPES, pH 7.4, 500 mM NaCl, 5 mM imidazole). Cells were lysed by sonication and then centrifuged (53,000 $\times g$, 30 min, 4 °C). The supernatant was collected and filtered (0.22 μ m filter pores) and applied to a Chelating Sepharose Fast Flow column (GE Healthcare) pre-equilibrated with NiSO₄. The column was washed with binding buffer, wash buffer (50 mM HEPES, pH 7.4, 500 mM NaCl, 50 mM imidazole) and elution buffer (50 mM HEPES, pH 7.4, 100 mM NaCl, 400 mM imidazole) with the elution pooled for further purification. The protein sample was buffer exchanged into buffer A (50 mM HEPES, pH 7.4) loaded onto a Fast Flow Q-Sepharose column (GE Healthcare) and a linear gradient of 0–1 M NaCl was applied. Fractions were analyzed by SDS-PAGE and appropriate samples taken forward for size exclusion chromatography on a Superdex 200 Increase column (GE Healthcare) in buffer B (50 mM HEPES, pH 7.4, 200 mM NaCl). Where necessary OCP samples were concentrated using centrifugal dialysis (VivaSpin, Sartorius).

Trehalose glass encapsulation of OCP_o and OCP_r was conducted using a similar method to that in previous work.^{67,68} 100 μ L of concentrated protein solution ($A_{\max} \sim 2$, 1 cm

path length) in aqueous buffer (50 mM HEPES, 200 mM NaCl, pH 7.4) was mixed with 100 μL of a trehalose-sucrose mixture (0.5 M trehalose, 0.5 M sucrose). 200 μL of the protein-trehalose mixture was drop-cast in the center of a quartz-coated glass substrate (S151, Ossila; $15\times 20\times 1.1$ mm). The substrate was incubated under vacuum (-70 kPa) with an excess of calcium sulfate desiccant (Drierite) at room temperature for at least 48 hours.

Some samples were additionally encapsulated with imaging spacers and a cover slip to protect the trehalose against atmospheric rehydration. For these samples, a stack of two imaging spacers (SecureSeal, Grace BioLabs; 9 mm diameter, 0.12 mm thickness) were attached to the quartz-coated glass substrate (S151, Ossila; $15\times 20\times 1.1$ mm) and 40 μL of the protein-trehalose mixture drop-cast in the center of the imaging spacer. The substrate was then placed in vacuum as above; pressure was released under a continuous flow of ultra-pure nitrogen gas, and a glass microscope cover slip (ThermoScientific; 22×22 mm, No.1 thickness) was attached to the upper imaging spacer.

For OCPo samples, all preparation steps and desiccation were conducted in the dark. For OCP_r, preparation and desiccation were conducted under bright white light, with samples illuminated for 30 min ($1600 \mu\text{mol photon m}^{-2} \text{s}^{-1}$) prior to the addition of the trehalose-sucrose solution and constant weaker illumination ($500 \mu\text{mol photon m}^{-2} \text{s}^{-1}$) for the duration of the desiccation. After encapsulation, samples were stored at room temperature in the dark.

S2.2 Steady-state absorbance spectroscopy

Absorbance of samples were (unless specified otherwise) measured in a commercial Cary double-beam spectrometer (Cary 60 UV-Vis Spectrophotometer, Agilent Technologies). Both zero and baseline corrections were applied with a blank sample; in the case of trehalose-encapsulated samples, an trehalose blank was used.

S2.3 Laser beam power and diameter measurements

Laser beam spot diameters ($1/e^2$) were measured at the sample positions with a CCD beam profiler (BC106N-VIS/M, Thorlabs). Unless stated otherwise, laser beam powers were measured slightly before the sample position (off-focus) with a photodiode power sensor (S120VC, Thorlabs) and meter console (PM100A or PM100D, Thorlabs). Both measurements were used in subsequent calculations for the pump fluence using the formula

$$\text{pump fluence} = \frac{P}{f\pi r_1 r_2} \tag{S2}$$

where P is the measured power, f is the laser repetition rate, and r_1, r_2 are the major/minor radii ($1/e^2$) of the beam at the sample position.

S2.4 Transient absorption spectroscopy

Picosecond transient absorption spectroscopy was undertaken with a commercial spectrometer (Helios, Ultrafast Systems) outfitted with a Ti:Sapphire seed laser (MaiTai, Spectra-Physics) providing 800 nm pulses (84 MHz, 25 fs nominal FWHM) and a Ti:Sapphire chirped-pulse amplifier (Spitfire Ace PA-40, Spectra-Physics) amplifying 800 nm pulses (10 kHz, 12 W average power, 40 fs nominal FWHM). Pump pulses were generated by seeding a part of the 800 nm beam into either a frequency doubler/tripler utilizing β -barium borate crystals (TimePlate, Photop Technologies) for 400 nm excitation, or an optical parametric amplifier (TOPAS Prime, Light Conversion) and subsequent frequency mixer (NirUVis, Light Conversion) for 420 nm to 600 nm excitations. An optical chopper was used to modulate the pump frequency to 5 kHz. Pump spectra used for some of the visible/NIR probe experiments are shown in Figure S2, and pump spectra for the UV-vis probe experiments are shown in Figure S17. Supercontinuum probes were generated with a part of the 800 nm pulse focused on either a continuously translating CaF_2 crystal for UV-vis probes (350–750 nm; we note that the use of a hot mirror and filters typically restricted the range to 370–690 nm, and with

low probe in the 370–400 nm sub-range), a sapphire crystal for visible probes (450–800 nm), or a YAG crystal for NIR probes (800–1600 nm). Pump-probe delay was controlled with a motorized delay stage with a random stepping order per-sweep, and the resulting sweeps are averaged. The signal was dispersed with a grating and detected with a CMOS sensor for UV-vis and visible probes, or an InGaAs sensor for NIR probe. The pump and probe polarizations were set to the magic angle. The room temperature was controlled at 19 °C.

Nanosecond to millisecond transient absorption spectroscopy was undertaken with a home-built pump-probe-reference setup. A Q-switched Nd:YVO₄ laser (Piccolo AOT 1, In-nolas) outfitted with an integrated harmonic module for frequency-doubling (to 532 nm) provided pump pulses (500 Hz, <800 ps nominal FWHM). A Ti:Sapphire regenerative amplifier (Solstice, Spectra-Physics) provided 800 nm pulses (1 kHz, 4 W nominal power, 90 fs nominal FWHM) for supercontinuum generation. 450–700 nm supercontinuum pulses were generated by focusing part of the 800 nm pulse on a sapphire crystal, and subsequently split into probe and reference beams with a 50:50 beamsplitter. The pump and probe were focused and overlapped on the sample, while the reference was focused on the sample \sim 2 mm away from the pump/probe overlap. Pump-probe/reference delay was controlled electronically with a digital delay generator (DG645, Stanford) with a linear stepping order per-sweep, and the resulting sweeps are averaged. To reduce 532 nm pump scatter, a 532 nm notch filter (NF533-17, Thorlabs) is placed after the sample. The probe and reference were dispersed with a volume phase holographic grating (Wasatch, 360 lines mm⁻¹ at 550 nm CW, 30 mm diameter, 3 mm thick, BK7) and directed onto two linear image sensors (S7030, Hamamatsu) driven and read out at the probe/reference repetition rate (1 kHz) by a custom-built board (Entwicklungsbuero Stresing). Transient absorption data was acquired with home-built software. The pump and probe polarizations were set to the magic angle. The room temperature was controlled at 19 °C.

Surface Xplorer 4.3.0 (Ultrafast Systems) was used in processing the transient absorption datasets. Noisy edges of the spectra were trimmed, and the program's bad spectra replace-

ment procedure was applied. A background correction (“subtract scattered light”) was then applied using the spectra before any apparent response from the sample. For ps transient absorption data using the visible and UV-vis probes, chirp correction was applied, choosing points at the first apparent signal for a given dynamic. Chirp was not discernible in the NIR-probe ps transient absorption data nor all ns–ms transient absorption data, so a chirp correction was not applied. Time zero was adjusted to the time of maximum initial signal in ps transient absorption data, while for ns–ms transient absorption data it was adjusted to the time of first signal. Further processing and some analysis was performed with home-built Python code. Glotaran 1.5.1 (<http://glotaran.org>),⁸⁶ a GUI for the R package TIMP,⁸⁷ was used in global lifetime/target analysis.

S2.5 Time-resolved absorbance spectroscopy

Time-resolved absorbance spectroscopy on continually-photoconverting OCP in solution under narrowband pump was undertaken using a home-built system. OCP in buffer was placed in a 2 mm path length (at normal incidence) quartz cuvette (Hellma 110-2-40). Conversion to OCP_r was continuously triggered by narrow-band pump light (78.3 MHz, <10 nm nominal FWHM, ± 5 nm nominal center wavelength accuracy) turned on at time $t = 0$. This pump light was provided by a supercontinuum laser (SuperK EXTREME EXU-6 PP, NKT Photonics) outfitted with a tunable filter (SuperK VARIA, NKT Photonics). Pump light was focused by a lens (LA4380, Thorlabs) through the cuvette at $\sim 40^\circ$ from the cuvette’s normal to minimize transmission and scattering into the spectrometer. The power of the pump was controlled such that the number rate of photon absorptions (*i.e.* OCP_o excitations) was approximately the same for each pump wavelength, achieved by keeping a constant product

$$P\lambda_{\text{pump}}(1 - 10^{A_{\text{dark}}}) \tag{S3}$$

where P is the steady-state power of the pump, λ_{pump} is the pump wavelength, and A_{dark} (shown as a green line in main text Figure 7b) is the absorbance of dark-adapted OCP in buffer determined at normal incidence using a separate spectrometer (FluoroMax-4, Horiba, fitted with a Xenon lamp). The exception to this pump power control was the non-absorbed 675 nm pump, where instead the photon rate was kept the same as that for 550 nm pump (so controlling $P\lambda_{\text{pump}}$ between those two pumps). We note that pump powers P were not measured close to the sample position to prevent pre-measurement photoconversion and also due to spatial limitations; they were instead measured and controlled at a position such that to reach the sample, reflection by three UV-enhanced Al mirrors (PF10-03-F01, Thorlabs) and focusing through the aforementioned lens is required. This results in a slightly wavelength-dependent fraction of power difference between what was measured as P and what was incident on the sample. After measurements were completed, this was checked by positioning the power meter at the sample position and at the far position, and summarized in Table S6. We note also that A_{dark} was determined at normal incidence, but the pump light was at $\sim 40^\circ$ from the cuvette's normal, so that the fraction of pump photons absorbed differs from $(1 - 10^{A_{\text{dark}}})$. We give full details of the pump power control, including an explanation and correction of these noted oversights, in Section S7.2; in short, the oversights did not have a substantial effect on our results. The yield of OCP_r was monitored by measuring the absorbance spectrum of OCP using a weak white-light probe from a fiber-coupled halogen-tungsten/deuterium lamp (DH-2000-BAL, Ocean Optics), turned on just before the pump; turning both on at $t = 0$ was not possible. This white-light was focused onto the sample close to normal incidence using collimating and focusing lenses. The pump and white light were overlapped in the cuvette close to their focuses. The sample-attenuated white light was collimated and focused by subsequent lenses into an optical fiber, in turn coupled to a CCD spectrometer (Andor Shamrock SR-303i-A, Oxford Instruments), measuring white-light transmission through the sample. Absorbance $A(t)$ was calculated using the measured

transmission through a cuvette containing solvent (buffer), with the equation

$$A(t) = -\log\left(\frac{I_{\text{OCP}}(t)}{I_{\text{buffer}}}\right) \quad (\text{S4})$$

where I_{OCP} is the transmission in counts measured by the CCD for OCP in solution, and I_{buffer} is that for buffer only. The pump spot diameter was ~ 30 μm and the white light spot diameter was ~ 1 mm at the overlap/sample position; note that these could not be determined precisely using a beam profiler due to the large angle of incidence of the pump beam. Experimental consistency was verified by repeating the experiment twice on the same OCP in buffer sample. No apparent degradation of the OCP occurred, and back-conversion from OCP_r to OCP_o in the dark was successful in the ≥ 1 hour between experimental runs. The room temperature was controlled at 18 °C.

S2.6 Figure preparation

OriginPro 9.6.0.172 (OriginLab), home-built Python code, and Inkscape 1.1.2 (<https://inkscape.org/>) were used to prepare the plots.

S3 Supplementary visible/NIR ps transient absorption materials

S3.1 Pump spectra

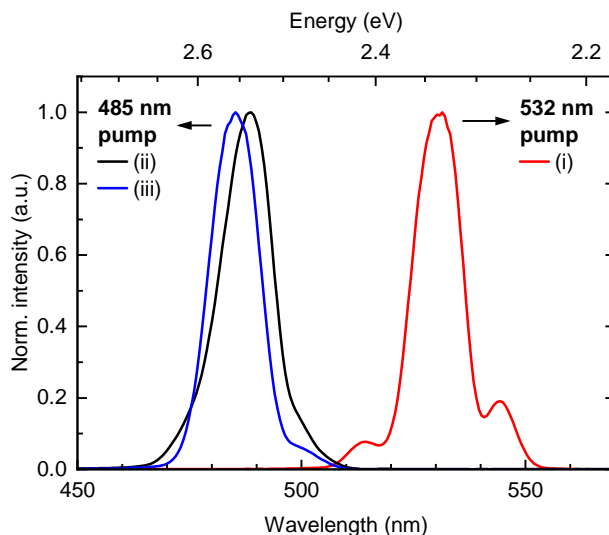


Figure S2: **Intensity spectra of the pumps used in the visible/NIR ps transient absorption experiments, normalized to the maximum intensity.** Small variations in the tunable pump generation resulted in slightly different pump profiles on each experimental day. 532 nm pump (i) was used in taking the visible-probe data shown in Figures 3a,b, S3a, and S4a. 485 nm pump (ii) was used in taking the visible-probe data shown in Figures S3b and S4b. 485 nm pump (iii) was used in taking the NIR-probe data shown in Figures S3b and S4b. The 532 nm pump used in taking the NIR-probe data of Figures 3a,b, S3a, and S4a was not recorded, and may have had a slightly different spectrum to (i).

S3.2 Transient absorption on OCPo and OCPr

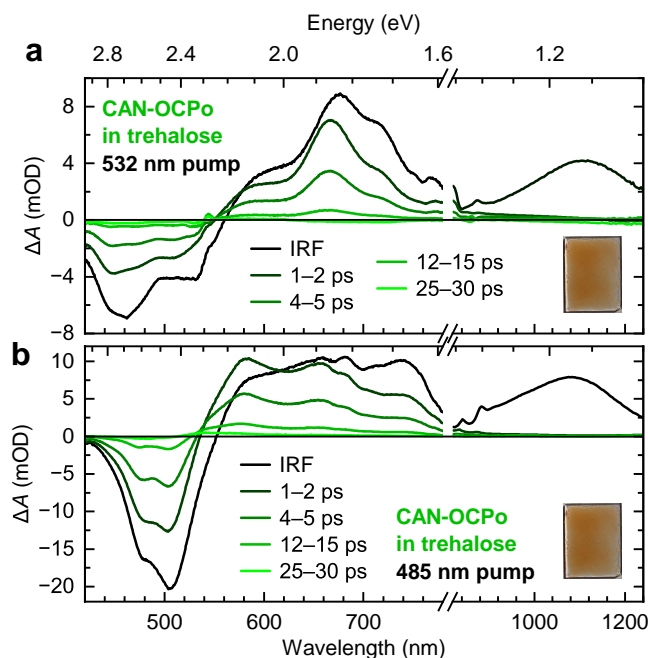


Figure S3: Picosecond transient absorption spectra of CAN-binding OCPo in trehalose glass with pump wavelength 532 nm (a) or 485 nm (b) with visible (left) and NIR (right) probes. Note that panel (a) is depicted in the main text (Figure 3a). Spectra have been averaged between the times indicated. Pump fluence was set to $200 \mu\text{J cm}^{-2}$.

In this section, we highlight the results of ps transient absorption with visible- and NIR-region probes under two different pump (excitation) wavelengths on CAN-OCPo in trehalose glass. We note that the visible/NIR-region measurements are admittedly worse quality than the UV-vis probe transient absorption, largely due to the significant sample degradation and the strong coherent artifact (from *e.g.* cross-phase modulation⁸⁸) present due to the high pump fluence densities ($200 \mu\text{J cm}^{-2}$) used. Furthermore, the set maximum time delay in the measurements was ~ 40 ps, leading to difficulty in resolving states with lifetimes beyond that. We therefore refrain from assigning a photophysical model to OCPo; doing this would require further ps transient absorption measurements with a lower fluence and further pump wavelengths.

The behavior of OCPo seemingly matches that of OCPr, including its pump wavelength

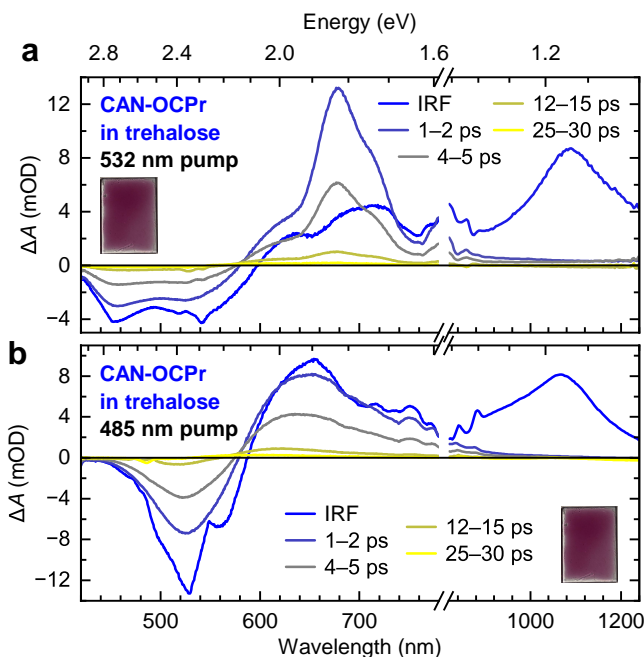


Figure S4: **Picosecond transient absorption spectra of CAN-binding OCPr in trehalose glass with pump wavelength 532 nm (a) or 485 nm (b) with visible (left) and NIR (right) probes.** A pump wavelength dependence on the spectra is apparent. Note that panel (a) is depicted in the main text (Figure 3b). Spectra have been averaged between the times indicated. Pump fluence was set to $200 \mu\text{J cm}^{-2}$.

dependence, although with an overall redshift. The photophysics with 532 nm pump (Figure S4a) is similar to that of OCPo, although with an overall redshift, consistent with the redshift seen in the absorbance (main text Figure 2). We see signatures of a longer-lived S*-like feature around 600 nm probe when using 485 nm pump (Figure S4b), easily seen with the loss of the near-isosbestic point, suggesting that OCPr also has an S*-like feature. However, the OCPr GSB at probe wavelength ~ 480 nm appears relatively diminished using 485 nm pump compared to 532 nm pump. This is the opposite to the relation seen in OCPo, most easily seen in main text Figure 4. We note that the signal is noisy in the ~ 480 nm region due to the 485 nm pump.

S3.3 Global lifetime analysis

As a comparison of the visible-probe ps transient absorption data of OCPo (Figure S3) to that using a UV-vis probe (Figure 4), in addition to seeing if an S*-associated component is fit in the case for OCPr (Figure S4), global lifetime analysis on the data was performed. This was done using the Glotaran 1.5.1 software package (<http://glotaran.org>),⁸⁶ a GUI for the R package TIMP.⁸⁷ Data used had already been processed with the steps outlined in the methods (Section S2.4); in particular, a chirp correction had already been applied, so that a term to account for chirp did not need to be included in the fitting. Noisy regions in the data due to pump scatter were excluded for all times to ensure a good fit of the rest of the data. Noisy red and blue ends in the data associated with tails of the probe were also excluded, so that the fitted wavelengths were 430 nm to 780 nm. The fitting was weighted favorably at later delay times to ensure good fits; Table S2 shows the weighting applied. Due to the strong coherent artifact feature in the first 0.5 ps, only data beyond that time was fitted. Thus, in the model, terms to account for the coherent artifact and S₂-like states were not included. This left a relatively simple fitted model of a number of decay-associated difference spectra (DADS) decaying exponentially in parallel.

Table S2: Weightings applied to time-ranges of the visible ps transient absorption data for the global lifetime analysis. Note that the maximum time delay in these experiments was ~ 40 ps.

Time range (ps)	Weighting
0.5 – 10	1
10 – 20	2
20 – 30	3
30 – 35	4
>35	5

2-component global lifetime analysis of the 532 nm pump data shown in the top panels of Figure S3 and Figure S4 are shown in Figure S5 and Figure S8. Fitting a 2-component parallel decay model in an artifact-free region of the visible-probe data beyond the initial

coherent artifact and S_2 -associated response gives two decay-associated difference spectra (DADS) for both the OCPo data and OCPPr data, with the longer time-constant DADS relatively weaker and blueshifted in both cases. A single component is not sufficient to adequately fit the region of the data, and a fitting a third component gives results with spurious DADS profiles. The results for OCPo are consistent (in the sense of the number of components required for a reasonable fit) with a 3-component global target analysis model applied to the UV-vis probe transient absorption data for pump wavelengths from 495 nm to 580 nm (and for the 2-component global lifetime analysis on the data for $\lambda_{\text{pump}} = 600$ nm); see Section S6.6.

Global lifetime analysis of the 485 nm pump data shown in the bottom panels of Figure S3 and Figure S4 clearly show the appearance of the S^* -like feature, with a third component required to adequately fit the data. The results for OCPo are consistent (in the sense of the number of components required for a reasonable fit) with the 4-component (or 5-component) global target analysis model applied to the UV-vis probe transient absorption data for 400 nm to 495 nm pump wavelengths; see Section S6.6.

We note that sample degradation (caused by the higher pump fluences in comparison with the UV-vis transient absorption data) likely affects the fitted time constants and DADS profiles. No further states with longer lifetimes were identified from these analyses of visible-probe transient absorption data, largely due to the limited delay time range chosen in the experiments (up to 40 ps).

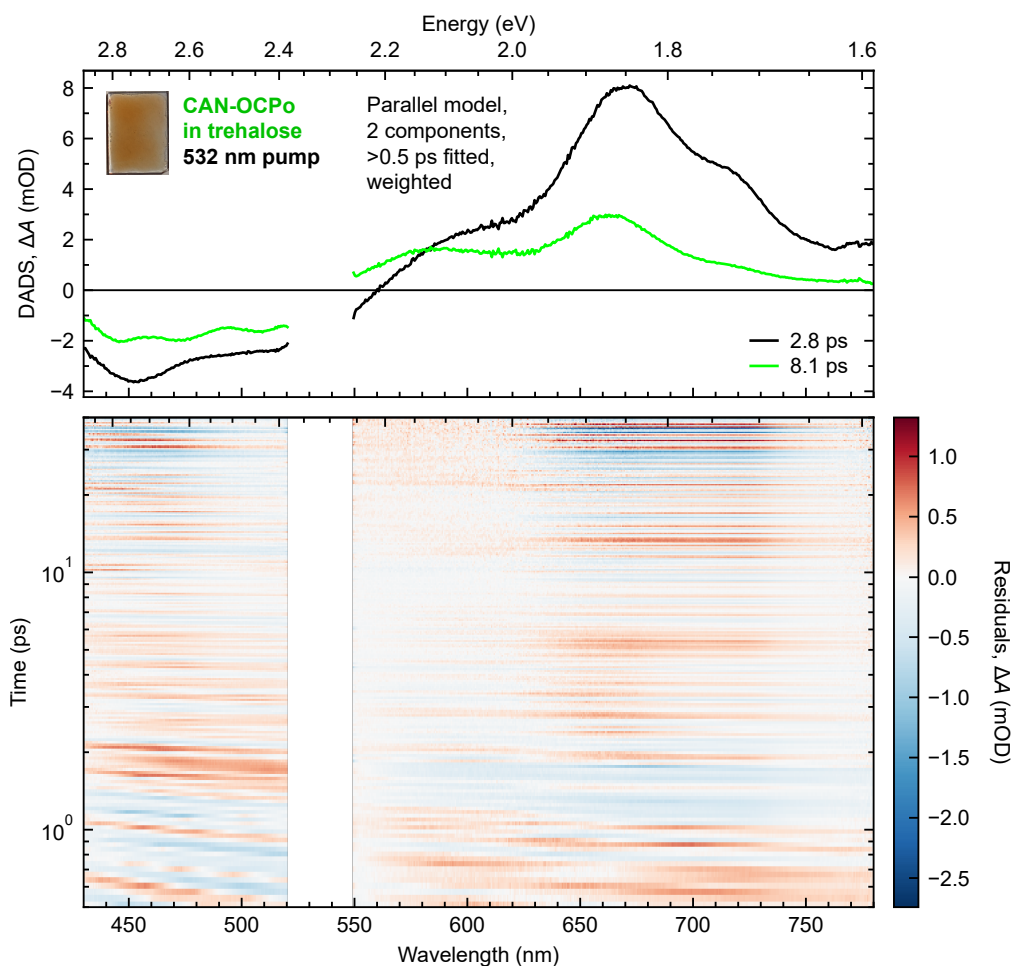


Figure S5: **Results of global lifetime analysis with a 2-component parallel model on transient absorption data of CAN-binding OCPo in trehalose with pump wavelength 532 nm and a visible probe: DADS (top) and residuals (bottom).** Only the wavelength range 430–780 nm and times >0.5 ps were fitted, and noisy data from 520.5–549.5 nm due to significant pump scatter was excluded from the fit. DADS time constants are specified in the legend. Residuals = Data – Fit. See text for further details.

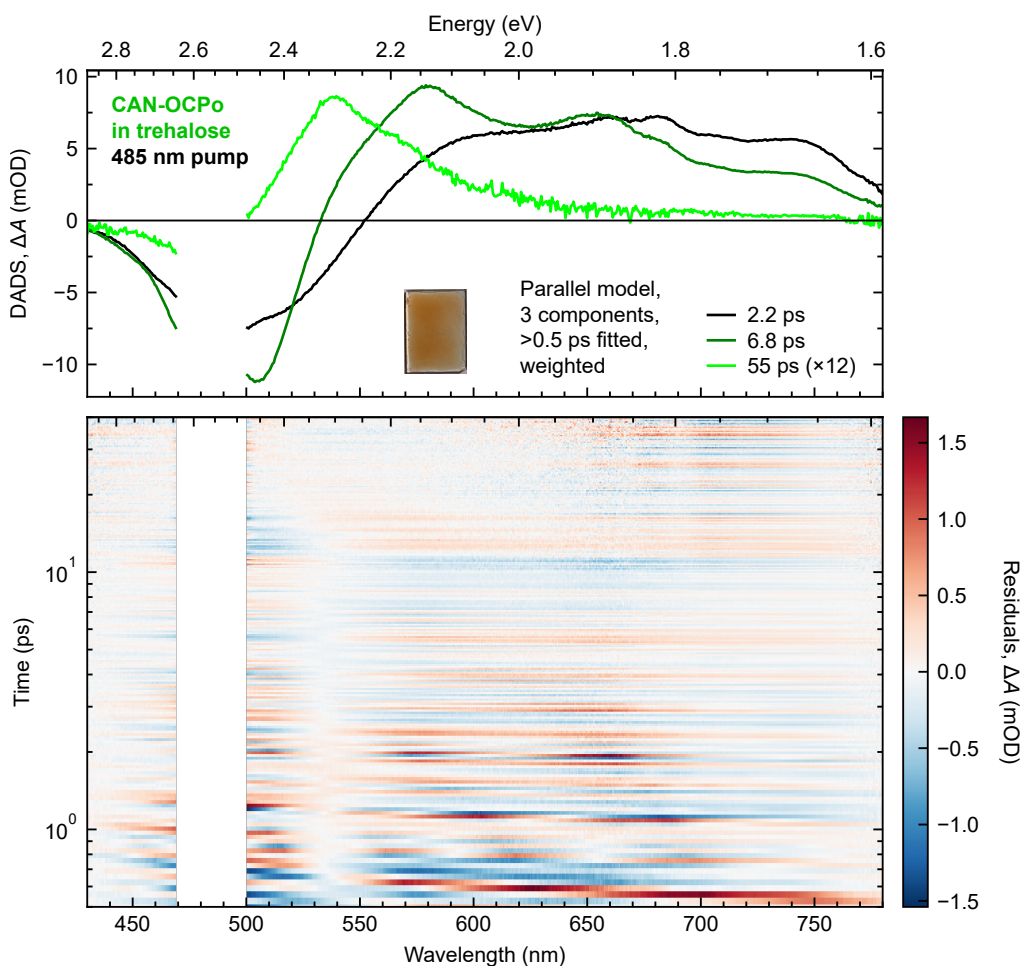


Figure S6: **Results of global lifetime analysis with a 3-component parallel model on transient absorption data of CAN-binding OCPo in trehalose with pump wavelength 485 nm and a visible probe: DADS (top) and residuals (bottom).** Only the wavelength range 430–780 nm and times >0.5 ps were fitted, and noisy data from 469.5–500 nm due to significant pump scatter was excluded from the fit. DADS time constants are specified in the legend; multiplications refer to scalings applied to the DADS. Residuals = Data – Fit. See text for further details.

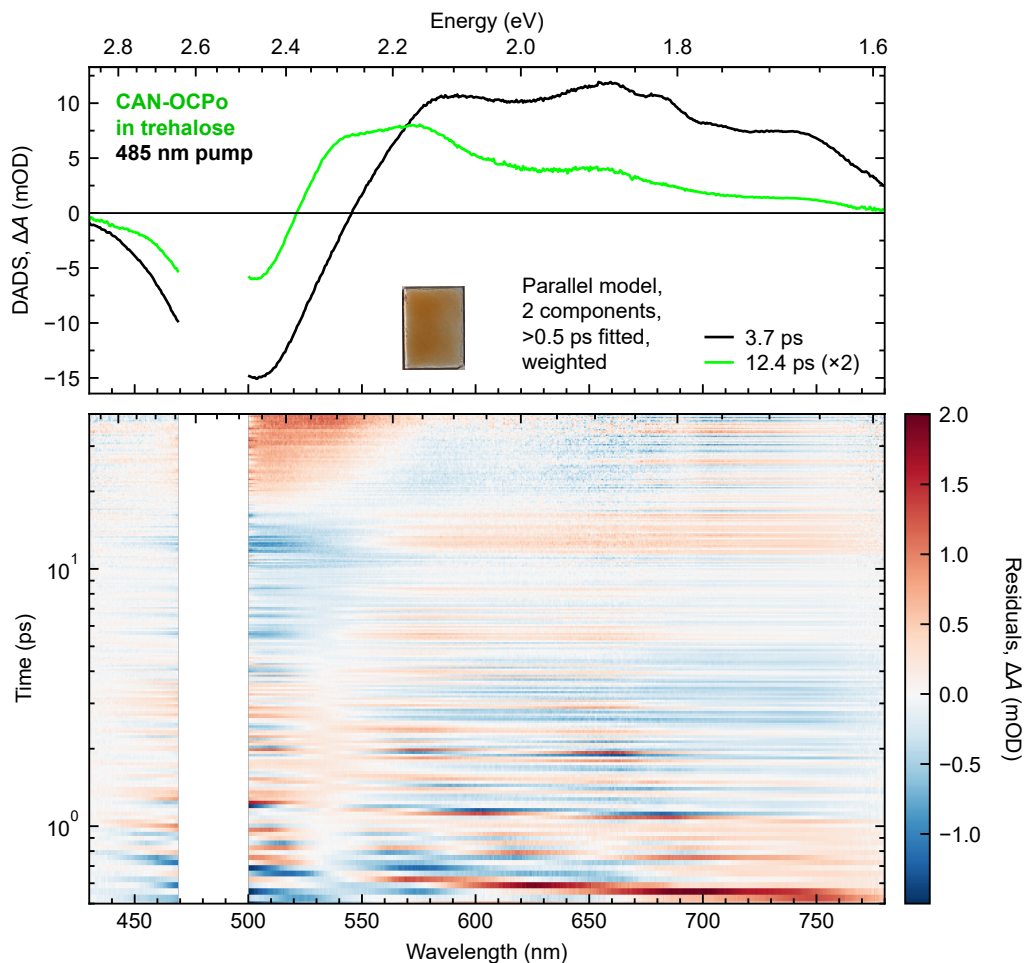


Figure S7: **Results of global lifetime analysis with a 2-component parallel model on transient absorption data of CAN-binding OCPo in trehalose with pump wavelength 485 nm and a visible probe: DADS (top) and residuals (bottom).** From the structure of the residuals, it is apparent that 2 components is not sufficient to fit this data. Only the wavelength range 430–780 nm and times >0.5 ps were fitted, and noisy data from 469.5–500 nm due to significant pump scatter was excluded from the fit. DADS time constants are specified in the legend; multiplications refer to scalings applied to the DADS. Residuals = Data – Fit. See text for further details.

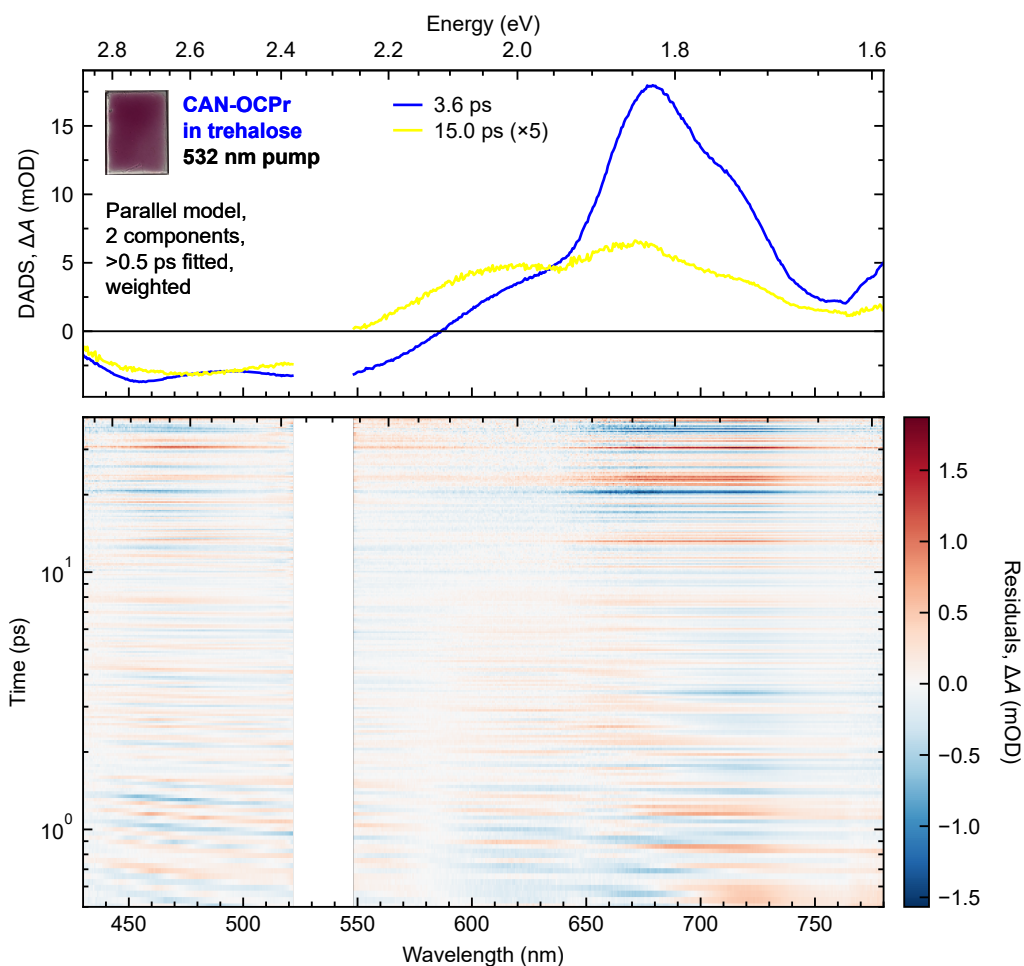


Figure S8: Results of global lifetime analysis with a 2-component parallel model on transient absorption data of CAN-binding OCPr in trehalose with pump wavelength 532 nm and a visible probe: DADS (top) and residuals (bottom). Only the wavelength range 430–780 nm and times >0.5 ps were fitted, and noisy data from 522–548 nm due to significant pump scatter was excluded from the fit. DADS time constants are specified in the legend; multiplications refer to scalings applied to the DADS. Residuals = Data – Fit. See text for further details.

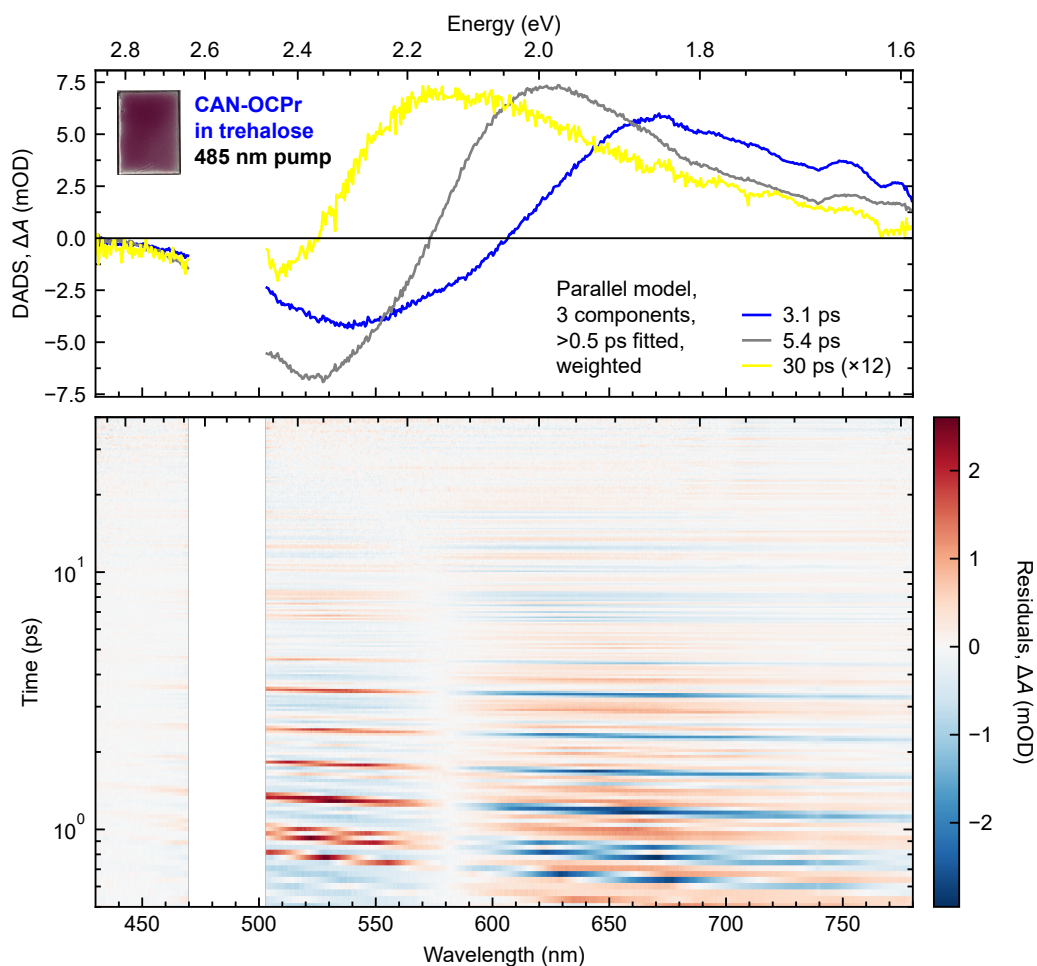


Figure S9: **Results of global lifetime analysis with a 3-component parallel model on transient absorption data of CAN-binding OCP_r in trehalose with pump wavelength 485 nm and a visible probe: DADS (top) and residuals (bottom).** Only the wavelength range 430–780 nm and times >0.5 ps were fitted, and noisy data from 470–503 nm due to significant pump scatter was excluded from the fit. DADS time constants are specified in the legend; multiplications refer to scalings applied to the DADS. Residuals = Data – Fit. See text for further details.

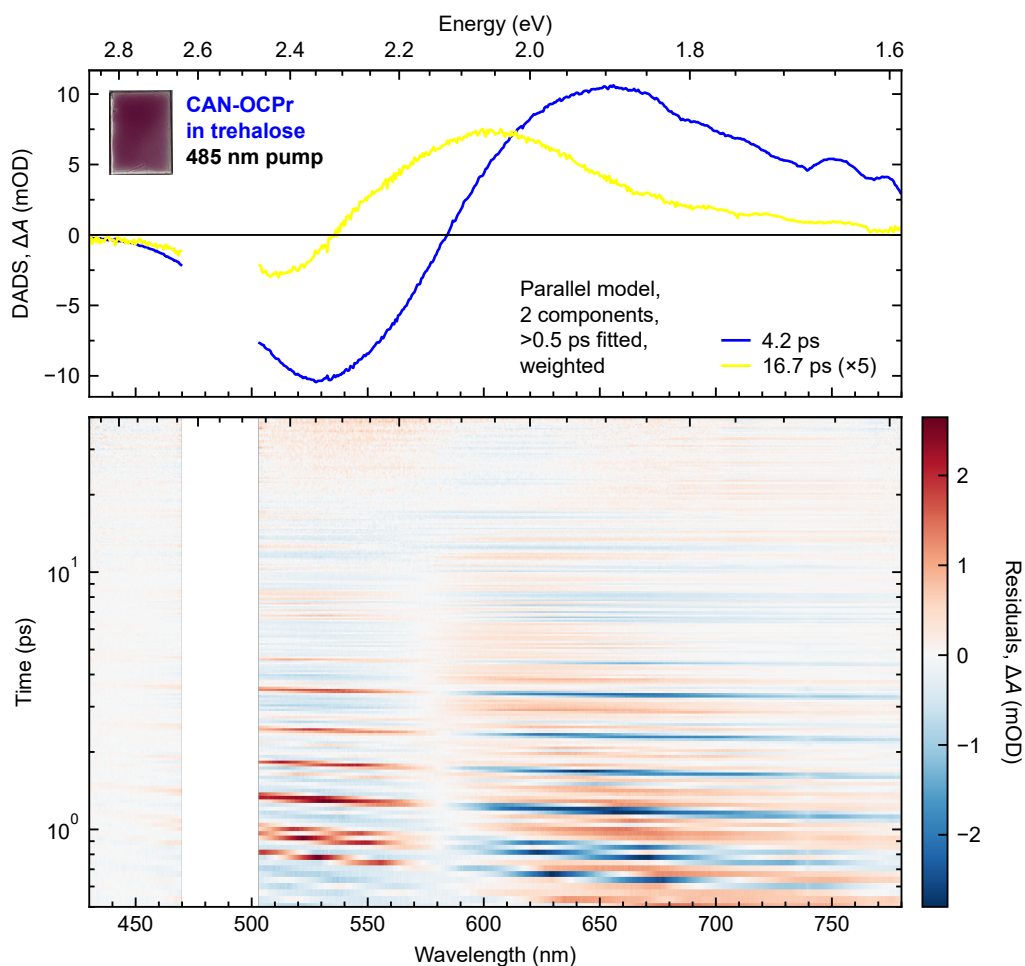


Figure S10: Results of global lifetime analysis with a 2-component parallel model on transient absorption data of CAN-binding OCP_r in trehalose with pump wavelength 485 nm and a visible probe: DADS (top) and residuals (bottom). Only the wavelength range 430–780 nm and times >0.5 ps were fitted, and noisy data from 470–503 nm due to significant pump scatter was excluded from the fit. DADS time constants are specified in the legend; multiplications refer to scalings applied to the DADS. Residuals = Data – Fit. See text for further details.

S4 Supplementary visible ns–ms transient absorption materials

S4.1 Transient absorption dynamics of OCPo in a flow cell

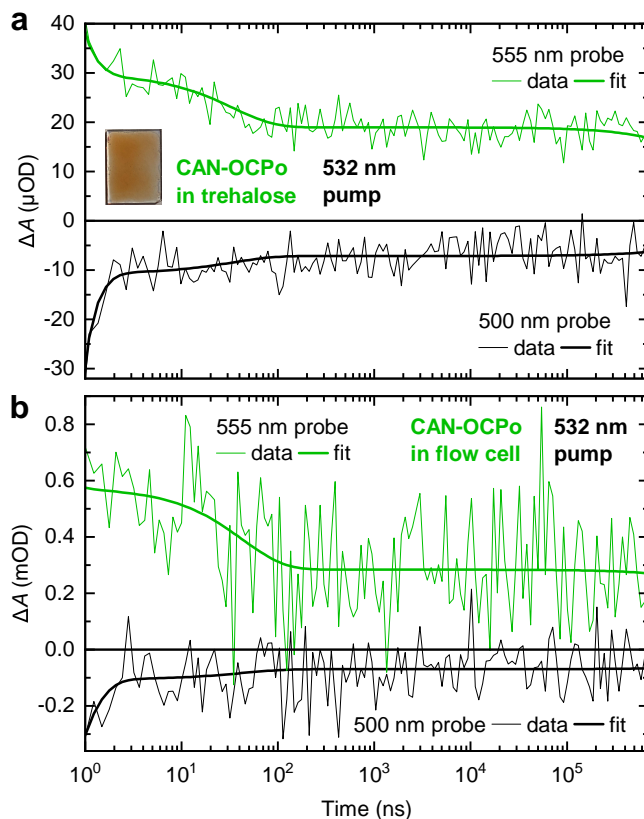


Figure S11: **Visible-probe ns–ms transient absorption dynamics of CAN-binding OCPo in trehalose (a) and in buffer (b) with pump wavelength 532 nm.** Data (thin lines) are a single probe wavelength (*i.e.* not averaged); see Figures 3c (trehalose) and 3d (buffer) for spectra. Fit (thick lines) are a single wavelength from the 4-component parallel global lifetime analysis on the data; see Figures S13 (trehalose) and S15 (buffer). Note the different y -axis scales between each panel.

Nanosecond-millisecond transient absorption dynamics of CAN-OCPo in trehalose at probe wavelengths 500 nm and 555 nm are shown in Figure S11a as thin lines. This is from the same dataset as that for the spectra of Figure 3c. Similar transient absorption dynamics of CAN-OCPo in buffer, refreshed with a flow cell, are shown in Figure S11b as thin lines. Spectra from the same dataset are shown in Figure 3d. As discussed in the main text, this transient absorption data in buffer shows no obvious differences to CAN-OCPo measured in trehalose or to 3'hECN-OCP reported elsewhere recently.³⁶

S4.2 Global lifetime analysis

Table S3: **Summary of initial parametrizations used in the global lifetime analysis of the visible ns–ms transient absorption data.** The time constants t_3 , t_4 , and t_5 (light green) were chosen to match the ≥ 50 ns EADS time constants determined by Konold *et al.* when using a higher pump power.³⁶ The 4-component sequential model omits the 10 μ s component. Note that a different initial IRF center is used for the trehalose and buffer data. As sequential models are being used, the decay rate constants k_i are the inverse of the corresponding time constants t_i ($k_i = t_i^{-1}$).

5-component sequential model	4-component sequential model
$t_1 = 100$ ps	$t_1 = 100$ ps
$t_2 = 1$ ns	$t_2 = 1$ ns
$t_3 = 50$ ns	$t_3 = 50$ ns
$t_4 = 10$ μ s	—
$t_5 = \infty$	$t_4 = \infty$
IRF center = 1 ns (trehalose) or 0.65 ns (buffer)	IRF center = 1 ns (trehalose) or 0.65 ns (buffer)
IRF FWHM = 0.35 ns	IRF FWHM = 0.35 ns

Global lifetime analysis was also performed on a selection of the ns–ms transient absorption data, using similar sequential models Konold *et al.* used for transient absorption data on 3'hECN-OCP with a 475 nm pump,³⁶ to check if similar >1 ns photoproducts described in their work are being formed in our samples, even when OCPo is within trehalose. This was also done using the Glotaran 1.5.1 software package (<http://glotaran.org>),⁸⁶ a GUI for the R package TIMP.⁸⁷ Data had already been processed with the steps outlined in the methods (Section S2.4). Noisy regions in the data due to pump scatter were set to zero ΔA for all times to ensure a good fit of the rest of the data. Noisy red and blue ends in the data associated with tails of the probe were also excluded. A number of models with different numbers of components were applied to the data, with the resulting evolution-associated difference spectra (EADS) corresponding to different photoproducts that exponentially decay into one another in sequence. A summary of the initial choices for time constants (*i.e.* decay rate constants) and the instrument response function (IRF) center and FWHM in the applied

models is shown in Table S3.

A 5-component sequential fit to the CAN-OCPO in trehalose transient absorption data gives latter components very similar to those found by Konold *et al.*, both in spectral profile and associated time constant. Figure S12 shows the fit, with EADS in the top panel and time constants specified in the legend. The first two EADS do not resemble those seen in Konold *et al.*, in terms of spectral profile and especially in associated time constants.³⁶ This is likely due to the instrument response function in our ns–ms transient absorption setup being ~ 1 ns, which is greater than the first three EADS time constants from a 6-component sequential fit in Konold *et al.* (1.4 ps, 4.5 ps, 24 ps), and greater than our own fitted EADS time constants (30.32 ps, 423.5 ps) and Gaussian IRF (FWHM = 350.2 ps). Our own attempts of a 6-component sequential fit result in degenerate EADS. However, the subsequent EADS (29.8 ns, 7.6 μ s, 11 ms closely match those of Konold *et al.* (50 ns, 50 μ s, infinite when using a higher pump power, and 50 ns, 25 μ s, infinite when using a lower pump power), further demonstrating that we are seeing the same photoproducts as 3'hECN-OCP in solution, despite our CAN-OCPO being trapped in trehalose. We note that the profile of the two EADS associated with 7.6 μ s and 11 ms match very closely, with a smaller amplitude decrease in the excited-state absorption (ESA) and especially in the ground-state bleach (GSB) compared to Konold *et al.*'s comparable EADS. We therefore print the results of a 4-component sequential fit on the same data in Figure S15; it is apparent from the structure of the residuals that omitting a ~ 10 μ s component does not affect the fit quality. The 4-component global fit is displayed as dynamics in Figure S11a as bold lines (data are thin lines).

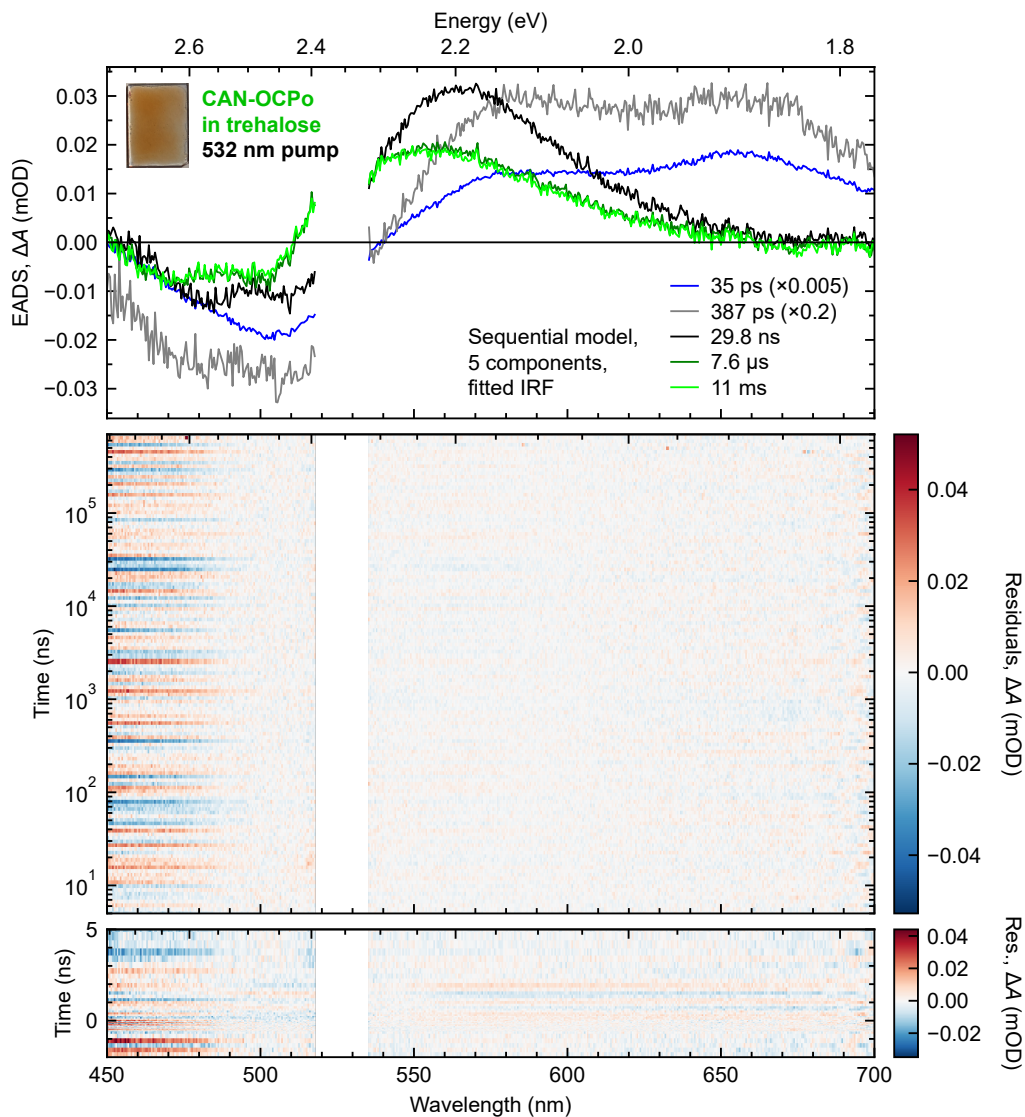


Figure S12: **Results of global lifetime analysis with a 5-component sequential model on transient absorption data of CAN-binding OCPo in trehalose with pump wavelength 532 nm and a visible probe: EADS (top) and residuals (middle, bottom).** Only the wavelength range 450–700 nm was fitted, and noisy data from 518–535 nm due to significant pump scatter was excluded from the fit. EADS time constants are specified in the legend; multiplications refer to scalings applied to the EADS. The fitted IRF has center 1.09 ns and FWHM 0.36 ns. Residuals = Data – Fit; note the logarithmic time-scale in the middle panel, and the linear time-scale and different residuals scale in the bottom panel. See text for further details.

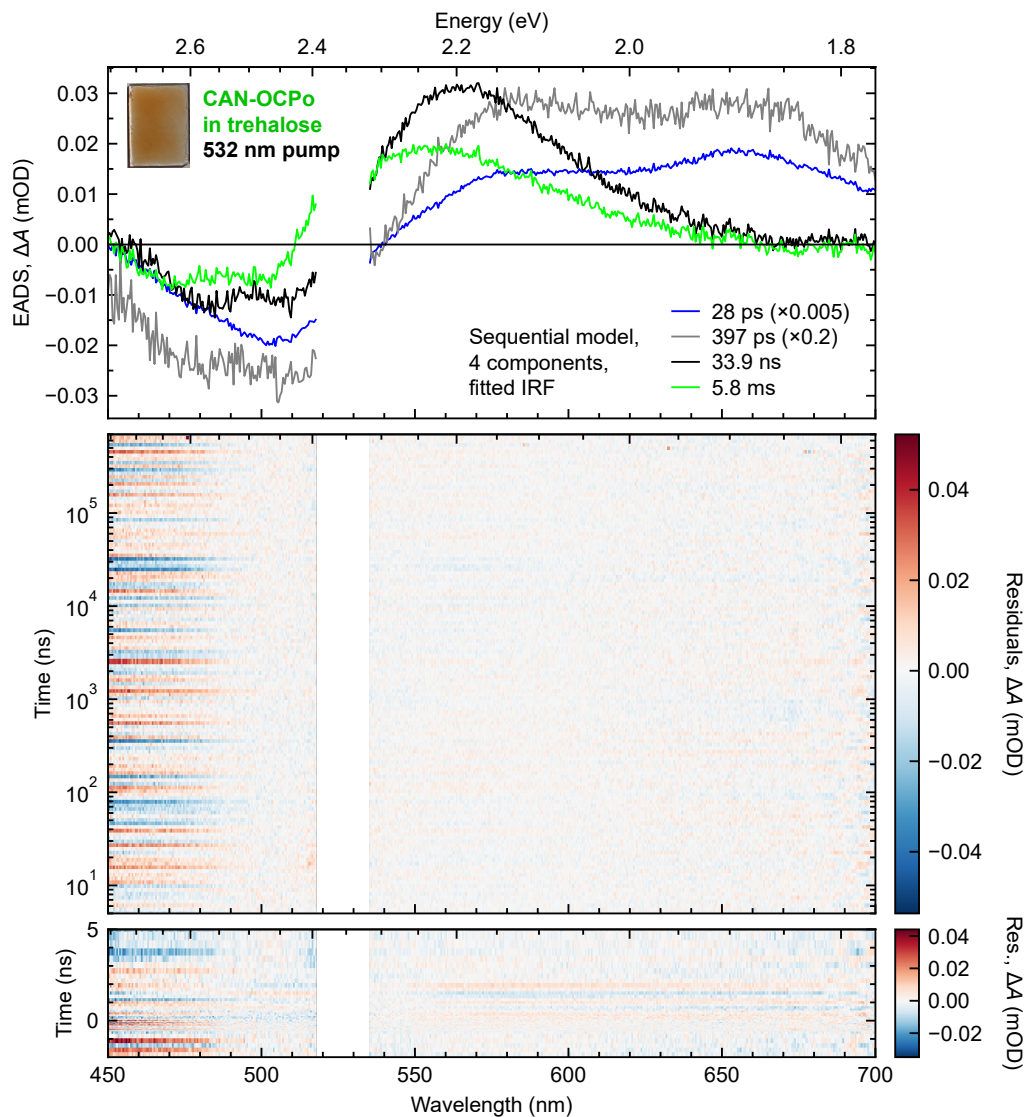


Figure S13: **Results of global lifetime analysis with a 4-component sequential model on transient absorption data of CAN-binding OCPo in trehalose with pump wavelength 532 nm and a visible probe: EADS (top) and residuals (middle, bottom).** Only the wavelength range 450–700 nm was fitted, and noisy data from 518–535 nm due to significant pump scatter was excluded from the fit. EADS time constants are specified in the legend; multiplications refer to scalings applied to the EADS. The fitted IRF has center 1.09 ns and FWHM 0.36 ns. Residuals = Data – Fit; note the logarithmic time-scale in the middle panel, and the linear time-scale and different residuals scale in the bottom panel. See text for further details.

As a final check, we undertake the same 5-component and 4-component sequential global lifetime analysis on our transient absorption data of CAN-OCPO in buffer in a flow cell, and the results are indeed consistent with both Konold *et al.*'s and our own in trehalose. The 5-component model results are shown in Figure S14. Here, the EADS associated with 1.6 ms appears to shift to more positive ΔA for all wavelengths, compared to the EADS for 12.4 μ s. This is inconsistent with both our in-trehalose results and Konold *et al.*'s results.³⁶ The 4-component model (dynamics in Figure S11b and EADS in Figure S15) where the ~ 10 μ s EADS is essentially omitted appears to fit the data as well as the 5-component model.

We emphasize that in these global lifetime analyses of the ns–ms transient absorption data, our first two EADS (time constants < 1 ns) have little physical significance. We also note that the maximum time delay in these experiments was 0.7 ms, and that the final EADS all have a fitted time constant exceeding that.

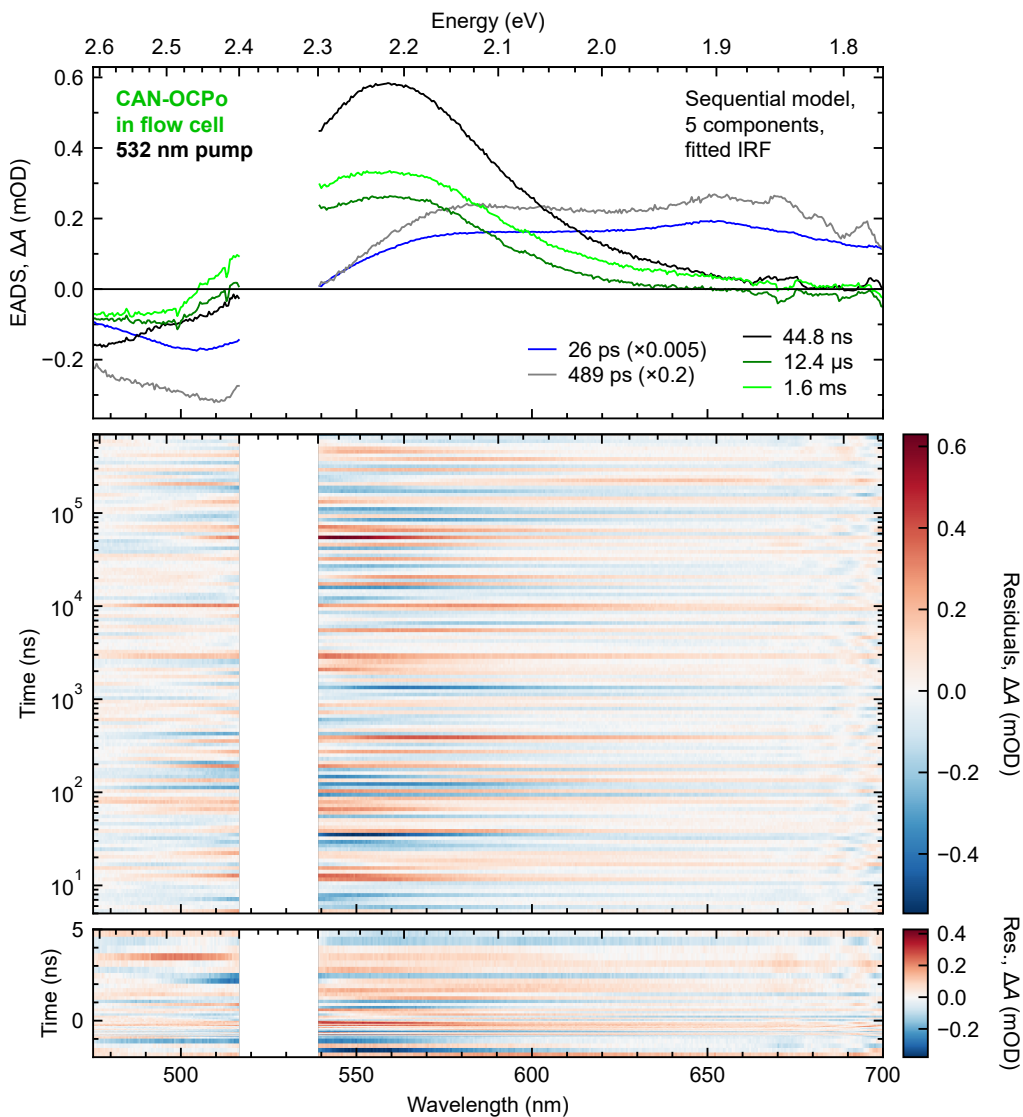


Figure S14: **Results of global lifetime analysis with a 5-component sequential model on transient absorption data of CAN-binding OCPo in buffer with pump wavelength 532 nm and a visible probe: EADS (top) and residuals (middle, bottom).** Only the wavelength range 475–700 nm was fitted, and noisy data from 517–539 nm due to significant pump scatter was excluded from the fit. EADS time constants are specified in the legend; multiplications refer to scalings applied to the EADS. The fitted IRF has center 0.67 ns and FWHM 0.28 ns. Residuals = Data – Fit; note the logarithmic time-scale in the middle panel, and the linear time-scale and different residuals scale in the bottom panel. See text for further details.

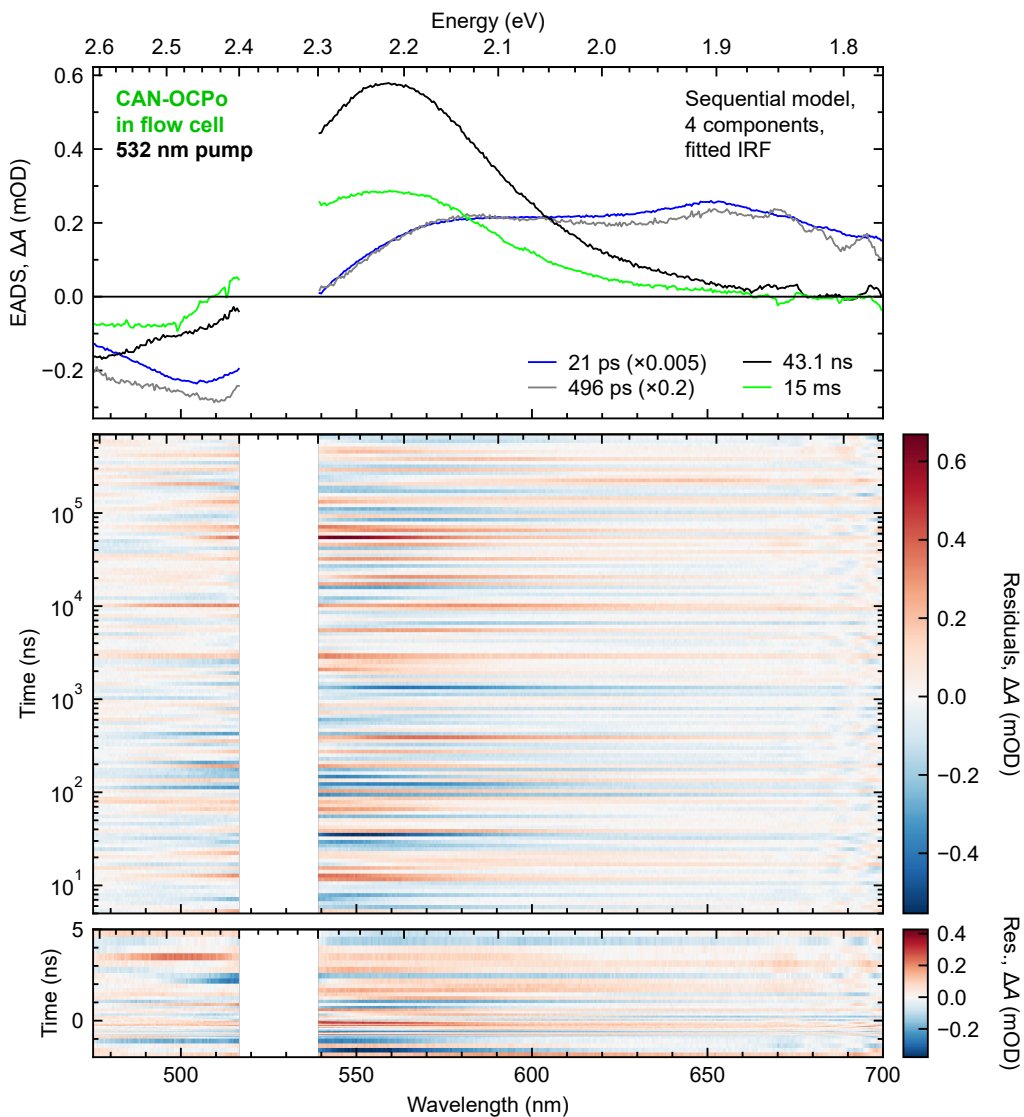


Figure S15: **Results of global lifetime analysis with a 4-component sequential model on transient absorption data of CAN-binding OCPo in buffer with pump wavelength 532 nm and a visible probe: EADS (top) and residuals (middle, bottom).** Only the wavelength range 475–700 nm was fitted, and noisy data from 517–539 nm due to significant pump scatter was excluded from the fit. EADS time constants are specified in the legend; multiplications refer to scalings applied to the EADS. The fitted IRF has center 0.69 ns and FWHM 0.29 ns. Residuals = Data – Fit; note the logarithmic time-scale in the middle panel, and the linear time-scale and different residuals scale in the bottom panel. See text for further details.

S5 Image showing no conversion in encapsulated CAN-OCPO

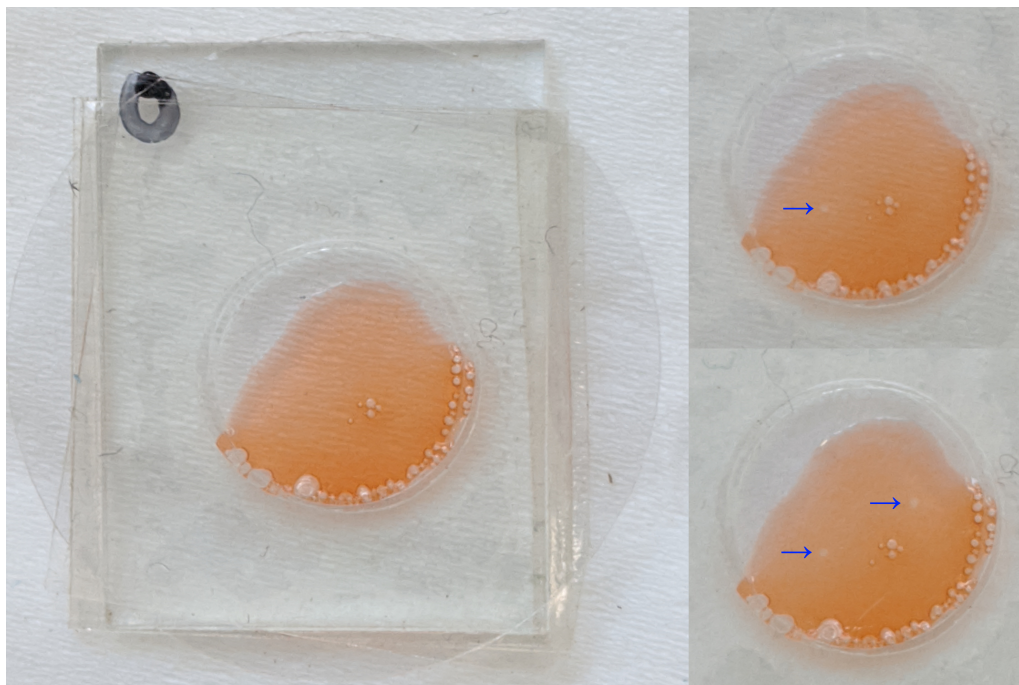


Figure S16: **CAN-OCPO sample in trehalose-sucrose glass with cover slip encapsulation.** Images to the right are the same sample after a first (top-right) and second (bottom-right) high pump-fluence picosecond transient absorption measurement; note the bleach spots indicated with blue arrows. No conversion to OCPr is apparent. In the ~ 30 min measurements, the film was pumped with 532 nm, 3.6 mW, 5 kHz pump pulses, with 465 μm and 340 μm the major and minor diameters ($1/e^2$). Therefore the pump fluence was 580 $\mu\text{J cm}^{-2}$. The majority of picosecond transient absorption measurements used significantly lower fluences and did not induce significant bleaching.

S6 Supplementary UV-vis ps transient absorption materials

S6.1 Pump spectra and comments on “bands”

For our pump wavelength-dependent ps transient absorption measurements on CAN-OCPo in trehalose, we obtain 420 nm to 600 nm pump pulses with an optical parametric amplifier (TOPAS Prime, Light Conversion). Certain pump wavelength “bands” require a different configuration of the TOPAS Prime. For 420 nm to 480 nm pump pulses, a configuration we dub band (A) is used; for 480–535 nm, band (B) is used; for 535–600 nm, band (C) is used. Measurements using each band were completed on separate experimental days (*i.e.* one day for band (B), one later day for band (A), and so on). We note that for 400 nm pump pulses, a frequency doubler utilizing β -barium borate crystals is used instead, and is denoted (TP) (see methods Section S2.4 for further experimental details).

Figure S17a shows normalized intensity spectra for the pump wavelengths used for transient absorption measurements depicted in Figures 4, 5, and 7a. The legend shows the nominal pump wavelength (as set in WinTopas4), the band used in generating that wavelength, and the measured pump powers (of the 5 kHz pulses measured per-second). Note that band (A) is used in generating the $\lambda_{\text{pump}} = 480$ nm used for experiments in the main text, and that band (B) is used in generating the main text $\lambda_{\text{pump}} = 535$ nm.

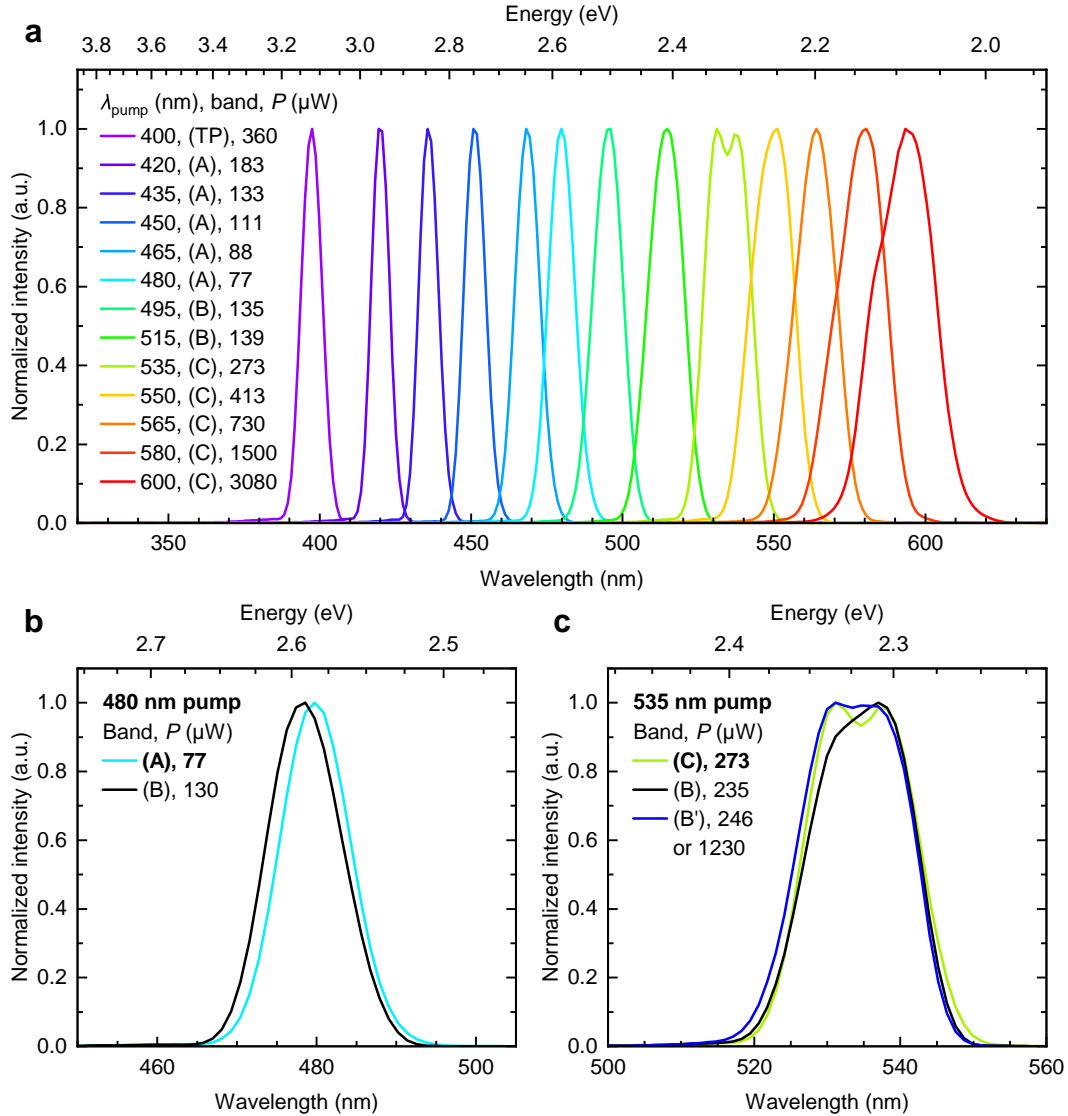


Figure S17: **Normalized intensity spectra of the pumps used in the UV-vis-probe ps transient absorption experiments, normalized to the maximum intensity.** Pump wavelengths (as set in WinTopas4), the TimePlate usage (here dubbed (TP)) or TOPAS Prime configuration for a band (here dubbed (A), (B), (C)), and the measured powers (of 5 kHz pulses measured per-second) are specified in the legend. **(a)** Intensity spectra of the pumps used in the experiments shown in the main text (Figures 4, 5, and 7a). **(b)** Intensity spectra of 480 nm pumps in band (A) (main text data) and band (B) (SI data; see Figure S18). **(c)** Intensity spectra of 535 nm pumps in band (C) (main text data), band (B) (SI data; see Figure S19), and band (B') (SI data; see Figure S20). The pump spot sizes at the sample position were generally not measured to save time, but are known to vary per-day and per-pump wavelength, with previous diameter ($1/e^2$) measurements typically in the range 400–800 μm .

S6.2 Replicates at same pump wavelengths in different bands

The use of different TOPAS Prime configurations does not have any effect on the transient absorption of CAN-OCPO in trehalose. We undertook control measurements using nominally (as set in WinTopas4) 480 nm and 535 nm pump wavelengths generated using band (B). For $\lambda_{\text{pump}} = 480$ nm, a comparison of the normalized intensity spectra between band (A) (main text) and band (B) (control) is shown in Figure S17b, and a comparison of transient absorption spectra and dynamics is shown in Figure S18. The results are near-identical. For $\lambda_{\text{pump}} = 535$ nm, a comparison of the normalized intensity spectra between band (C) (main text) and band (B) (control) is shown in Figure S17c, and a comparison of transient absorption spectra and dynamics is shown in Figure S19. Again, the results are near-identical. We note that a different CAN-OCPO film spot was used for each measurement, and (as stated above) measurements using each band were done on separate experimental days.

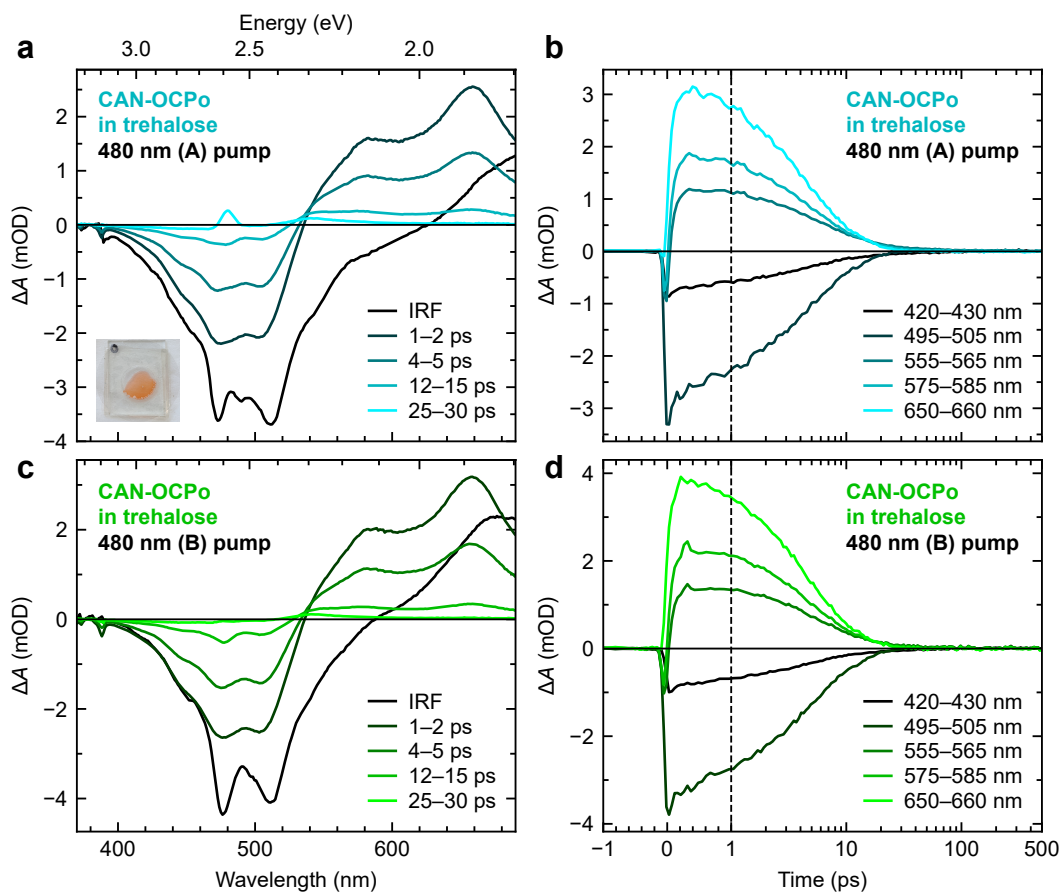


Figure S18: **Transient absorption spectra (a,c) and dynamics (b,d) on CAN-binding OCPo in trehalose using 480 nm pump wavelength in band (A) (a,b) and band (B) (c,d).** Both pumps give near-identical features, with differences attributable to small variations between the pump spectra (see Figure S17b). We note that a different film spot was used between band (A) and band (B), and each band's measurements were done on separate experimental days. The dynamic plots (b,d) have a linear time-axis up to 1 ps, and subsequently logarithmic up to 500 ps.

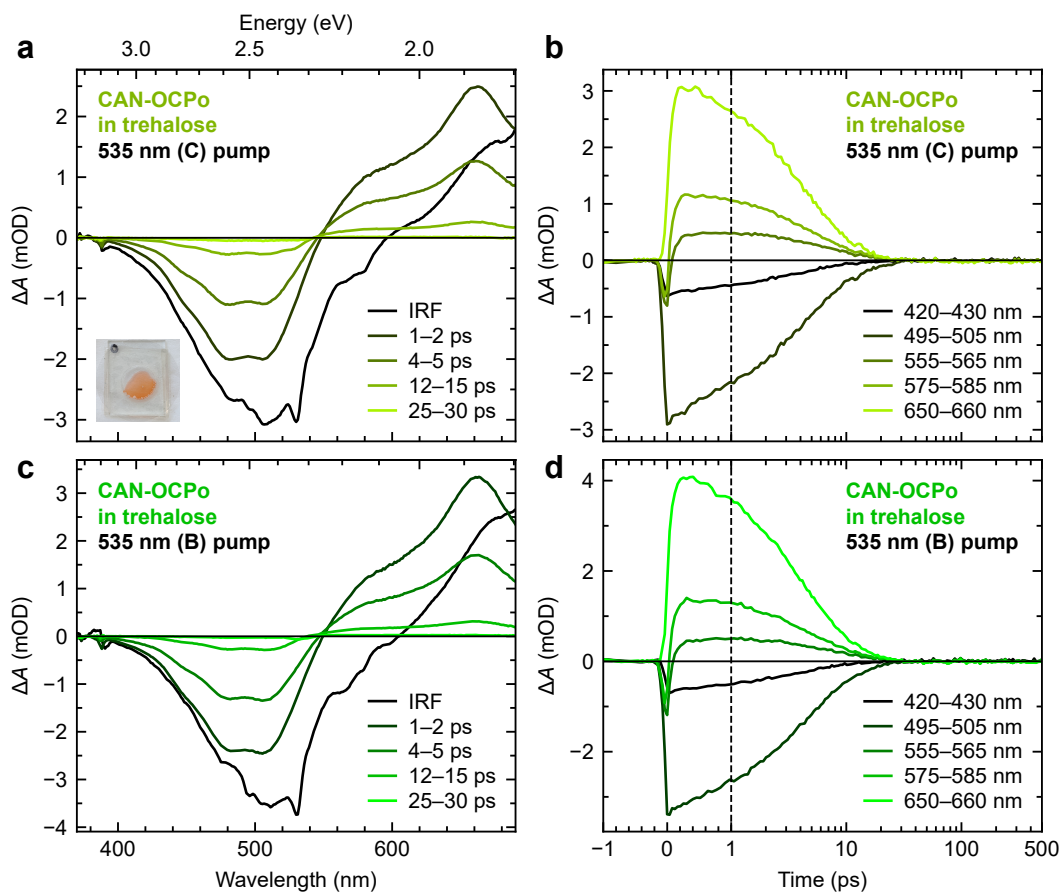


Figure S19: **Transient absorption spectra (a,c) and dynamics (b,d) on CAN-binding OCPo in trehalose using 535 nm pump wavelength in band (C) (a,b) and band (B) (c,d).** Both pumps give near-identical features, with differences attributable to small variations between the pump spectra (see Figure S17c). We note that a different film spot was used between band (C) and band (B), and each band's measurements were done on separate experimental days. The dynamic plots (b,d) have a linear time-axis up to 1 ps, and subsequently logarithmic up to 500 ps.

S6.3 Pump fluence independence

A brief check shows that the pump fluence has no effect on the CAN-OCPo in trehalose transient absorption beyond increased degradation, although only a few pump fluences were used at $\lambda_{\text{pump}} = 535$ nm only. Figure S20 shows the transient absorption spectra (panels a,c) and dynamics (b,d) using a $10 \mu\text{J cm}^{-2}$ pump fluence (a,b) and then a $50 \mu\text{J cm}^{-2}$ pump fluence (c,d) at the same spot on the film. Pump powers for those fluences were tuned following a measurement of the pump diameters ($1/e^2$), which were found to be $934.1 \mu\text{m}$ (major axis) and $671.1 \mu\text{m}$ (minor axis). Therefore, $273 \mu\text{W}$ (a,b) and $1230 \mu\text{W}$ (c,d) pump powers gave the respective pump fluences. See methods Section S2.3 for further details. A subsequent measurement using $200 \mu\text{J cm}^{-2}$ pump fluence ($4920 \mu\text{W}$ pump power) led to near-complete sample degradation (not shown). We note that band (B') was the same TOPAS Prime configuration as band (B), but the former was a different experimental day, with additional post-sample filters compared to the other UV-vis-probe measurements, along with slightly differing pump intensity spectra (see Figure S17c).

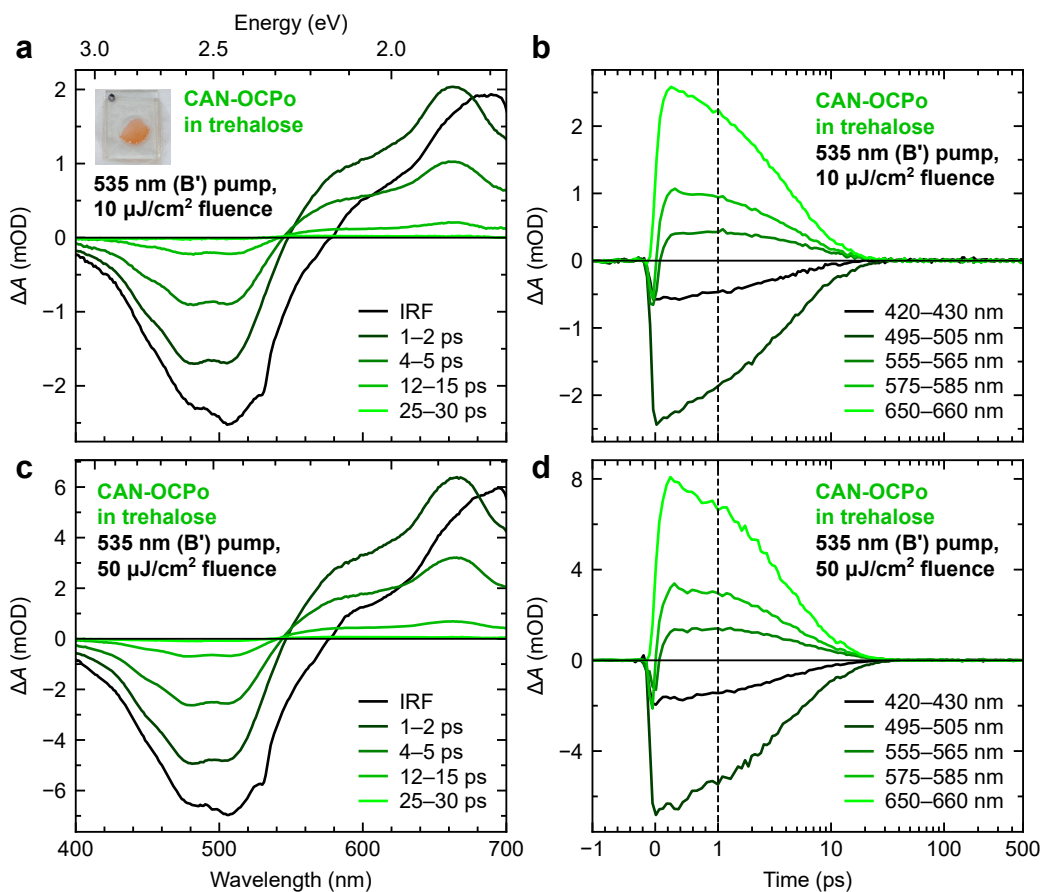


Figure S20: **Pump fluence dependence on the transient absorption spectra (a,c) and dynamics (b,d) of the same spot on CAN-binding OCPo in trehalose using 535 nm pump wavelength in band (B').** Both the $10 \mu\text{J cm}^{-2}$ pump fluence (a,b) and the subsequent $50 \mu\text{J cm}^{-2}$ fluence (c,d) gave near-identical spectra (a,c) and dynamics (b,d) on the same film spot, with differences attributable to sample degradation. The dynamic plots (b,d) have a linear time-axis up to 1 ps, and subsequently logarithmic up to 500 ps.

S6.4 Global fit of dynamics parameters

Table S4: **Fit parameters found using a global triexponential fit to the data in Figure 5.** The triexponential equation used is $\Delta A_{\text{fit}}(t) = \alpha_1 \exp(-t/\tau_1) + \alpha_2 \exp(-t/\tau_2) + \alpha_3 \exp(-t/\tau_3)$ with a lower bound $\alpha_i \geq 0$ applied. The fitted time constants are $\tau_1 = 2.8 \pm 0.2$ ps, $\tau_2 = 6.5 \pm 0.4$ ps, and $\tau_3 = 65 \pm 2$ ps; note that as a global fit, these are the same for all pump wavelengths. Errors specified here are fit parameter standard errors.

λ_{pump} (nm)	α_1	α_2	α_3
400	0.243 ± 0.047	0.315 ± 0.043	0.500 ± 0.010
420	0.167 ± 0.054	0.485 ± 0.047	0.430 ± 0.010
435	0.238 ± 0.055	0.475 ± 0.050	0.350 ± 0.009
450	0.271 ± 0.061	0.540 ± 0.055	0.267 ± 0.009
465	0.333 ± 0.070	0.615 ± 0.063	0.161 ± 0.008
480	0.355 ± 0.072	0.637 ± 0.066	0.090 ± 0.008
495	0.512 ± 0.076	0.598 ± 0.073	0.012 ± 0.007
515	0.533 ± 0.077	0.602 ± 0.074	0.006 ± 0.007
535	0.591 ± 0.073	0.509 ± 0.071	0.011 ± 0.007
550	0.735 ± 0.074	0.452 ± 0.076	0.000 ± 0.007
565	0.783 ± 0.070	0.361 ± 0.073	0.000 ± 0.007
580	0.850 ± 0.068	0.297 ± 0.073	0.004 ± 0.007
600	0.909 ± 0.064	0.194 ± 0.070	0.015 ± 0.007

S6.5 Global target analysis summary and discussion

It is usual, in analysis of OCP transient absorption data, to disentangle and quantify spectral contributions using analysis such as dynamic fitting with multi-exponential fits, or spectrokinetic analysis such as global lifetime/target analysis.^{15,31,34,36,60,71} However, due to the IVR and VC apparent within the S_1 lifetimes, these analyses are not completely suited for this system. In particular, the aforementioned multi-exponential fitting implicitly assumes well-defined species, and that first-order rate equations describing concentration changes between species may be written (their solutions being a sum of exponentials). Meanwhile, global lifetime/target analysis assumes that the spectra of the species are time-independent (*i.e.* well-defined) and that the kinetics (concentration traces) are probe wavelength-independent,⁸⁹⁻⁹¹

a condition called bilinearity. These assumptions do not hold due to the effect of IVR and VC.^{50,55–58}

Nevertheless, to compare with literature, depict a sample of our global target analysis models in Figure S21a, and a selection of the results in Figure S21b–d, with further details below. Here we apply models involving 3 or 4 components depending on the pump wavelength, hence resulting in 3 or 4 species-associated difference spectra (SADS). The 3-component model (Figure S21a, excluding blue box) sufficiently fits transient absorption data with pumps from 495 nm to 580 nm, while a fourth component (Figure S21a, SADS4-inclusive) is required to fit the data with pumps from 400 nm to 480 nm, once again consistent with the presence of long-lived forms of OCPo and associated S*-like features for $\lambda_{\text{pump}} \leq 480$ nm. We note that the profile of all SADS and their fitted time constant t_i vary with excitation wavelength, suggesting that the model is not valid with this dataset. We discuss the global lifetime analysis further, give plots of all SADS, and show additional models below.

S6.6 Global target analysis extended results

Global target analysis on the UV-vis-probe ps transient absorption datasets was done using the Glotaran 1.5.1 software package (<http://glotaran.org>),⁸⁶ a GUI for the R package TIMP.⁸⁷ Since a target model is applied, we term the extracted ΔA -profiles species-associated difference spectra (SADS). Data used had already been processed with the steps outlined in the methods (Section S2.4); in particular, a chirp correction had already been applied, so that a term to account for chirp did not need to be included in the fitting. Noisy regions in the data due to pump scatter were excluded for all times to ensure a good fit of the rest of the data. Noisy red and blue ends in the data associated with tails of the probe were also excluded, so that the fitted wavelengths were typically 400 nm to 690 nm. Terms to account for the instrument response function (IRF) and the coherent artifact were included. For the IRF, a Gaussian is convoluted with the exponential decays and parametrized within the model, with its center and full-width half-maximum (FWHM) fitted. For the coherent

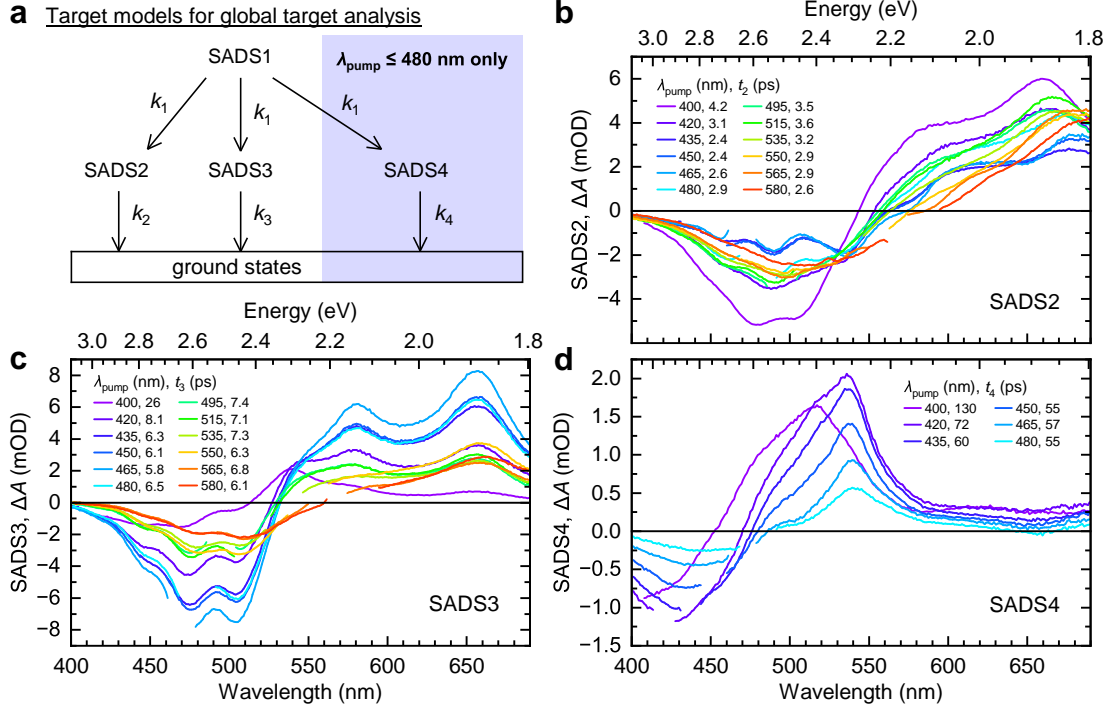


Figure S21: **Sample of the results of global target analysis performed on the transient absorption data.** (a) Target model used in the global target analysis performed, with resulting species-associated difference spectra (SADS) shown in the other panels: (b) SADS2, (c) SADS3, (d) SADS4; note that SADS4 is fitted only with pump wavelengths ≤ 480 nm. Full results and additional global target analysis are detailed in Section S6.6.

artifact, an additional component with the time profile of the IRF is fitted; we do not show this component in our figures.

We generally use a model depicted in Figure S22b where we fit a SADS corresponding to a single initially populated S_2 -like state that subsequently decays with an equal (shared) time constant into each of the fitted SADS, with those subsequently decaying with different time constants into the ground state. In the main text, we eventually assign different ground-state heterogeneities within OCPo; a target model possibly more accurate to this is depicted in Figure S22a. It includes multiple SADS corresponding to multiple S_2 -like states that decay individually with different time constants into a paired SADS, subsequently decaying with different time constants into a ground state. However, the ~ 100 fs time resolution, the relatively temporal sampling around time zero, and the coherent artifact obscure distinct states within the first ~ 200 fs, so attempts applying the more detailed model failed to

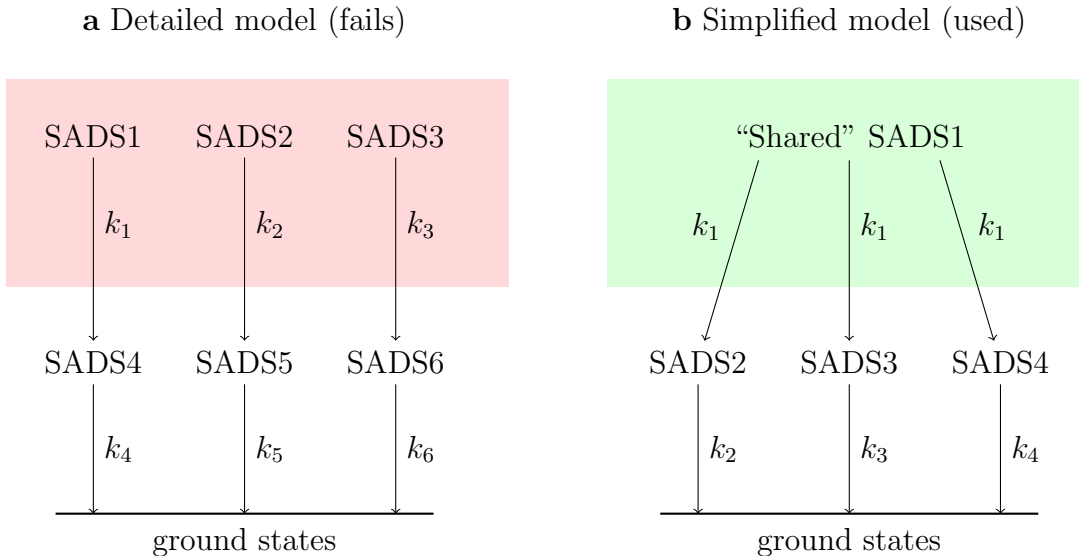


Figure S22: **Diagrams of representative global target analysis models applied to the UV-vis ps transient absorption data.** (a) The model considering distinct S_2 -like states from ground-state heterogeneities that fails to converge or give reasonable results. (b) The simplified model that was used instead, with a shared S_2 -like state and shared decay rate k_1 to the distinct SADS. The instrument response function and coherent artifact are accounted for in the model. Note that in some applications of the model, the number of SADS is adjusted (*e.g.* SADS4 may be removed, or a SADS5 added). See SI text for full details.

converge or give reasonable results. We consequently use the aforementioned model with a single, shared, fast-decaying SADS. Regardless, we believe that this does not remove support for a multiple ground-state assignment.

We find that the 4-SADS model is needed to fit transient absorption datasets with pump wavelengths from 400 nm to 480 nm, but the 3-SADS model is sufficient to fit those with pump wavelengths from 495 nm to 600 nm. The associated fitted decay time constants vary but are somewhat consistent with those extracted from the global triexponential fit of the normalized dynamics (main text Figure 5 and SI Table S4). The requirement that a fourth SADS is needed to fit transient absorption datasets for $\lambda_{\text{pump}} \leq 480$ nm is once again consistent with the presence of long-lived forms of OCPo and associated S^* -like features for those pump wavelengths.

We note that the four-SADS model somewhat underfits the transient absorption data

for the pump wavelength 400 nm (Figure S23) and possibly 420 nm (Figure S24) with an observable structure in the residuals. The result of respective five-SADS models are shown in Figures S35 and S36. The requirement of SADS5 for a better fit is indicative of further ground-state heterogeneity.

An exception to the “target” fitting procedure specified above is the analysis of the 600 nm pump wavelength transient absorption data (Figure S37). As a relatively high pump power is used (see legend in Figure S17), the coherent artifact is relatively strong, so the early-time dynamics cannot be easily fitted with the target model. We therefore fitted times beyond 0.5 ps with a 2-component parallel global lifetime analysis model with no IRF or coherent artifact terms, very similar to the model applied to the visible-probe transient absorption data (Section S3.3), although with no weighting of the data here due to greater maximum delay used (~ 500 ps). This corresponds to two decay-associated difference spectra (DADS) decaying in parallel after initial population from the unmodelled (cropped out) S_2 -like states. DADS1 and DADS2 are comparable to SADS2 and SADS3 respectively.

The variations in the SADS profiles and associated decay time constants per-pump wavelength (particularly for SADS2 and SADS3) are indicative that global target (and lifetime) analysis is not valid with this dataset. This is because of the affects of internal vibrational redistribution (IVR) and vibrational cooling (VC). The assumption of bilinearity (separable spectral and kinetic contributions) in using global lifetime/target analysis^{89–91} does not hold, with the IVR/VC essentially giving the spectra some time-dependence.^{55–58} Indeed, SADS2 and SADS3 have a mixed and unknown physical correspondence, likely mixed S_1 decay, IVR, and VC between the different ground-state forms of CAN-OCPo. Likewise, SADS1 may correspond to S_2 /IVR/VC for multiple CAN-OCPo forms (as discussed above; see Figure S22), in addition to a potential coherent artifact contribution (the additional IRF-time profile component may not always account for it fully). Meanwhile, SADS4 (and SADS5) can more safely be associated with the S^* -like form of OCPo due to the 1-order difference between their associated decay time constants compared to those for SADS1, SADS2, and

SADS3.

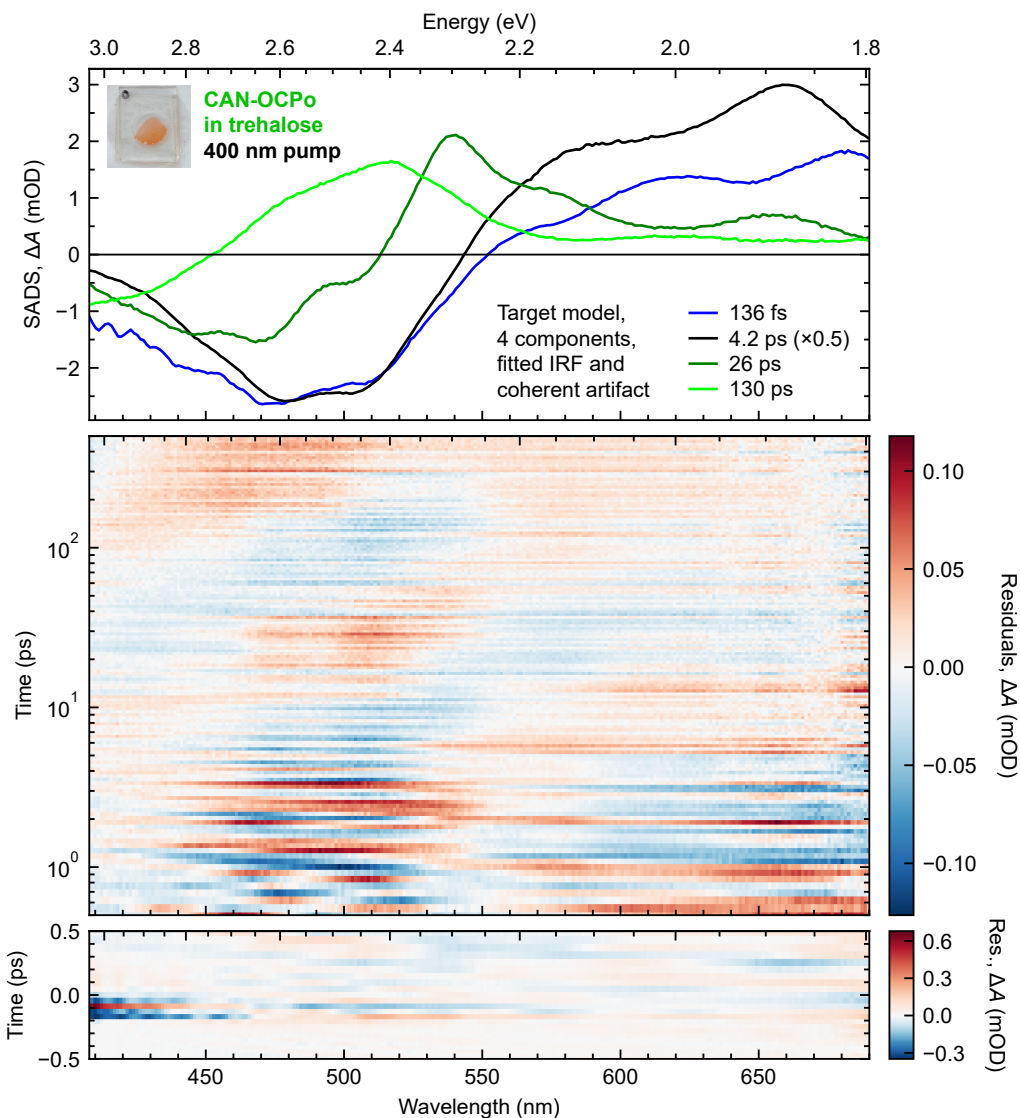


Figure S23: Results of global target analysis with a 4-component target model on transient absorption data of CAN-binding OCPo in trehalose with pump wavelength 400 nm and a UV-vis probe: SADS (top) and residuals (middle, bottom). Only the wavelength range 407–690 nm was fitted to exclude noisy data due to low probe light and significant pump scatter. SADS time constants are specified in the legend; multiplications refer to scalings applied to the SADS. The fitted IRF has center -78 fs and FWHM 64 fs. A coherent artifact with the concentration profile of the IRF was fitted but not shown here. Residuals = Data $-$ Fit; note the logarithmic time-scale in the middle panel, and the linear time-scale and different residuals scale in the bottom panel. See text for further details.

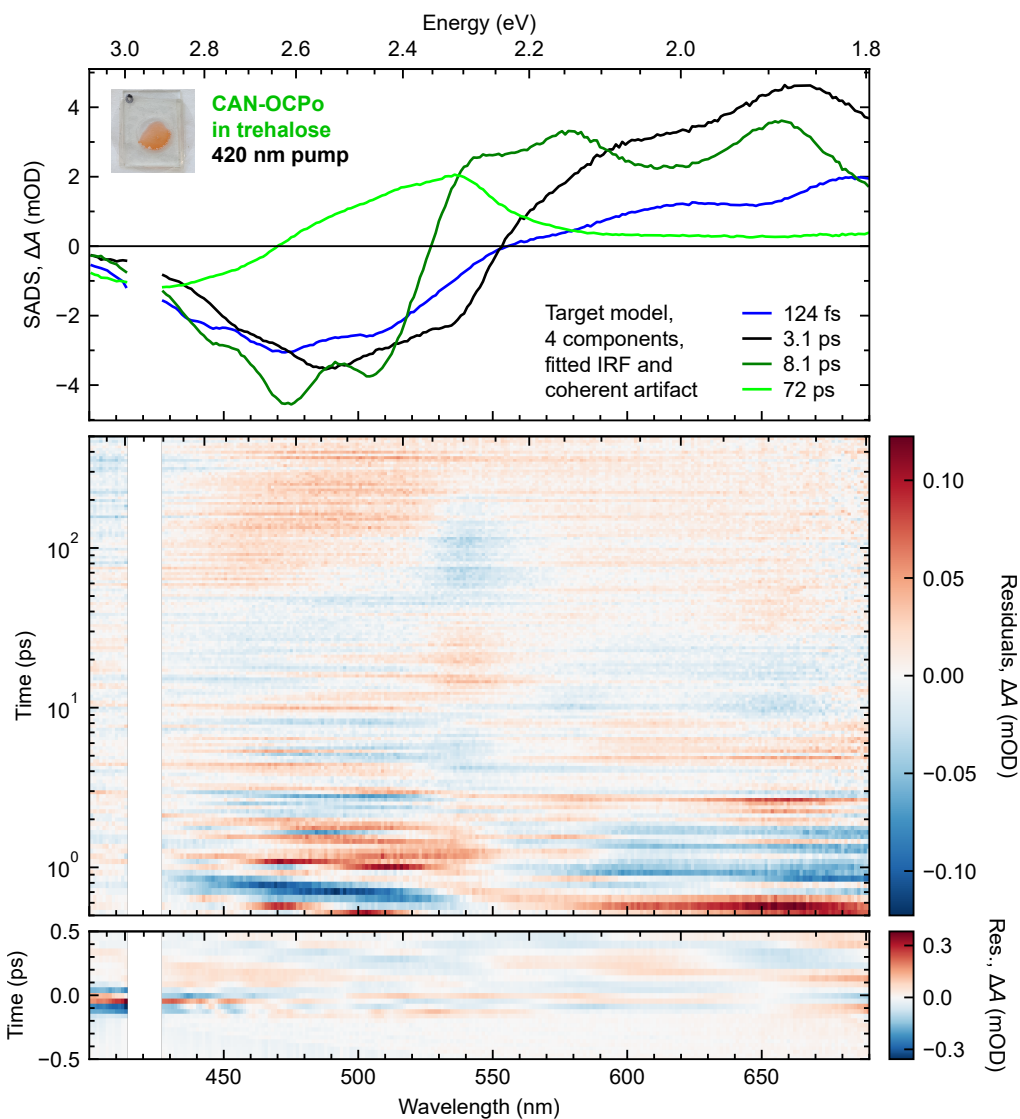


Figure S24: Results of global target analysis with a 4-component target model on transient absorption data of CAN-binding OCPo in trehalose with pump wavelength 420 nm and a UV-vis probe: SADS (top) and residuals (middle, bottom). Only the wavelength range 400–690 nm was fitted, and noisy data from 414–427 nm due to significant pump scatter was excluded from the fit. SADS time constants are specified in the legend. The fitted IRF has center -50 fs and FWHM 47 fs. A coherent artifact with the concentration profile of the IRF was fitted but not shown here. Residuals = Data – Fit; note the logarithmic time-scale in the middle panel, and the linear time-scale and different residuals scale in the bottom panel. See text for further details.

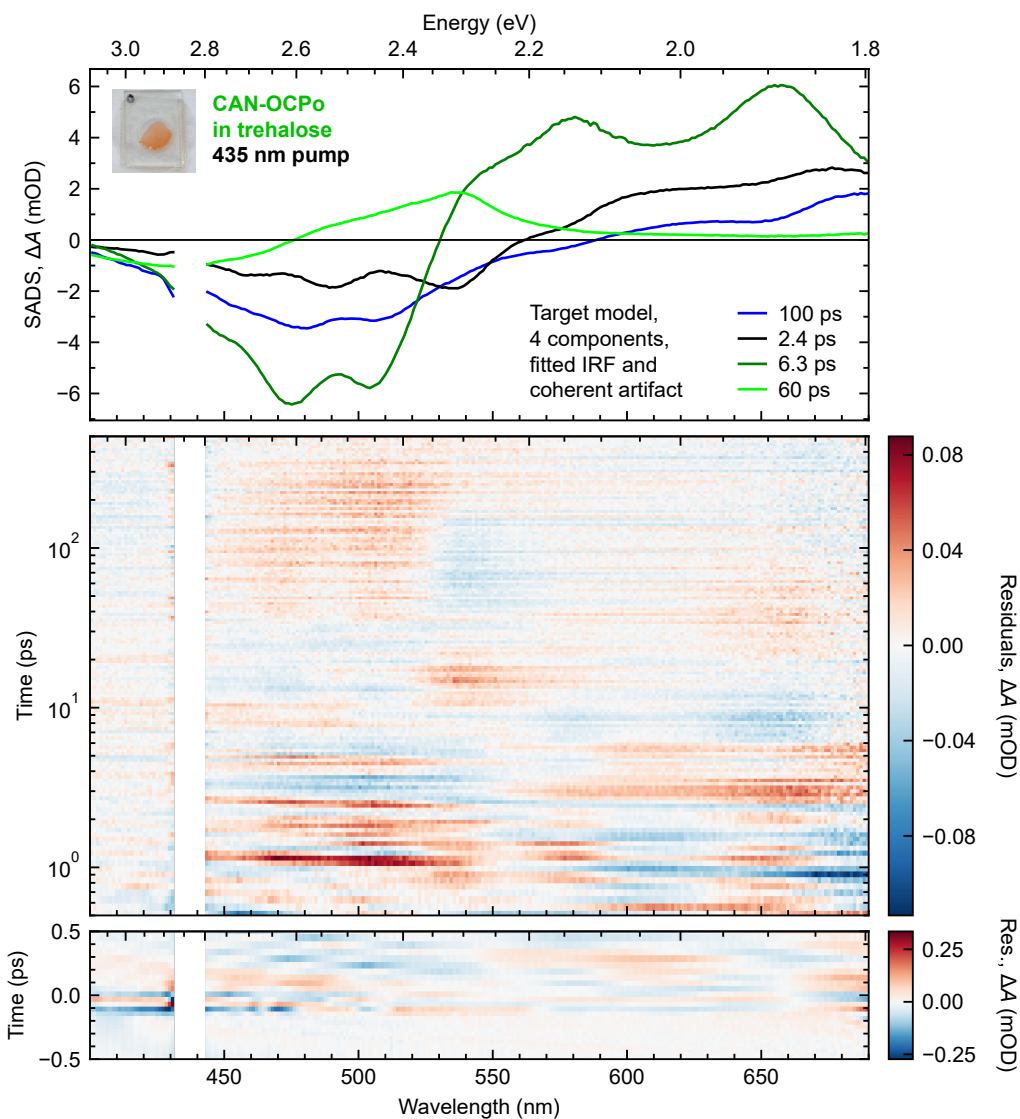


Figure S25: Results of global target analysis with a 4-component target model on transient absorption data of CAN-binding OCPo in trehalose with pump wavelength 435 nm and a UV-vis probe: SADS (top) and residuals (middle, bottom). Only the wavelength range 400–690 nm was fitted, and noisy data from 432–443 nm due to significant pump scatter was excluded from the fit. SADS time constants are specified in the legend. The fitted IRF has center -55 fs and FWHM 36 fs. A coherent artifact with the concentration profile of the IRF was fitted but not shown here. Residuals = Data – Fit; note the logarithmic time-scale in the middle panel, and the linear time-scale and different residuals scale in the bottom panel. See text for further details.

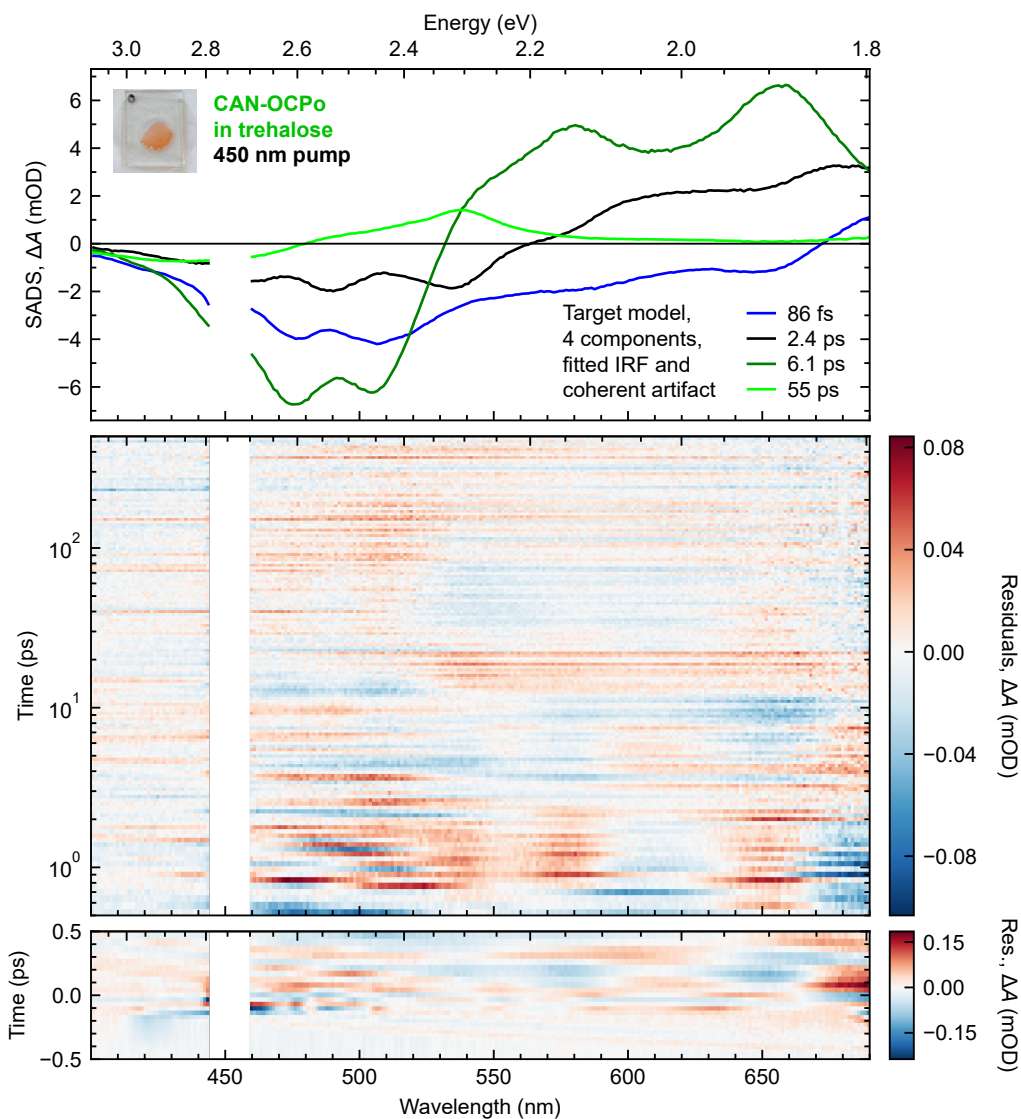


Figure S26: Results of global target analysis with a 4-component target model on transient absorption data of CAN-binding OCPO in trehalose with pump wavelength 450 nm and a UV-vis probe: SADS (top) and residuals (middle, bottom). Only the wavelength range 400–690 nm was fitted, and noisy data from 444–459 nm due to significant pump scatter was excluded from the fit. SADS time constants are specified in the legend. The fitted IRF has center -66 fs and FWHM 30 fs. A coherent artifact with the concentration profile of the IRF was fitted but not shown here. Residuals = Data – Fit; note the logarithmic time-scale in the middle panel, and the linear time-scale and different residuals scale in the bottom panel. See text for further details.

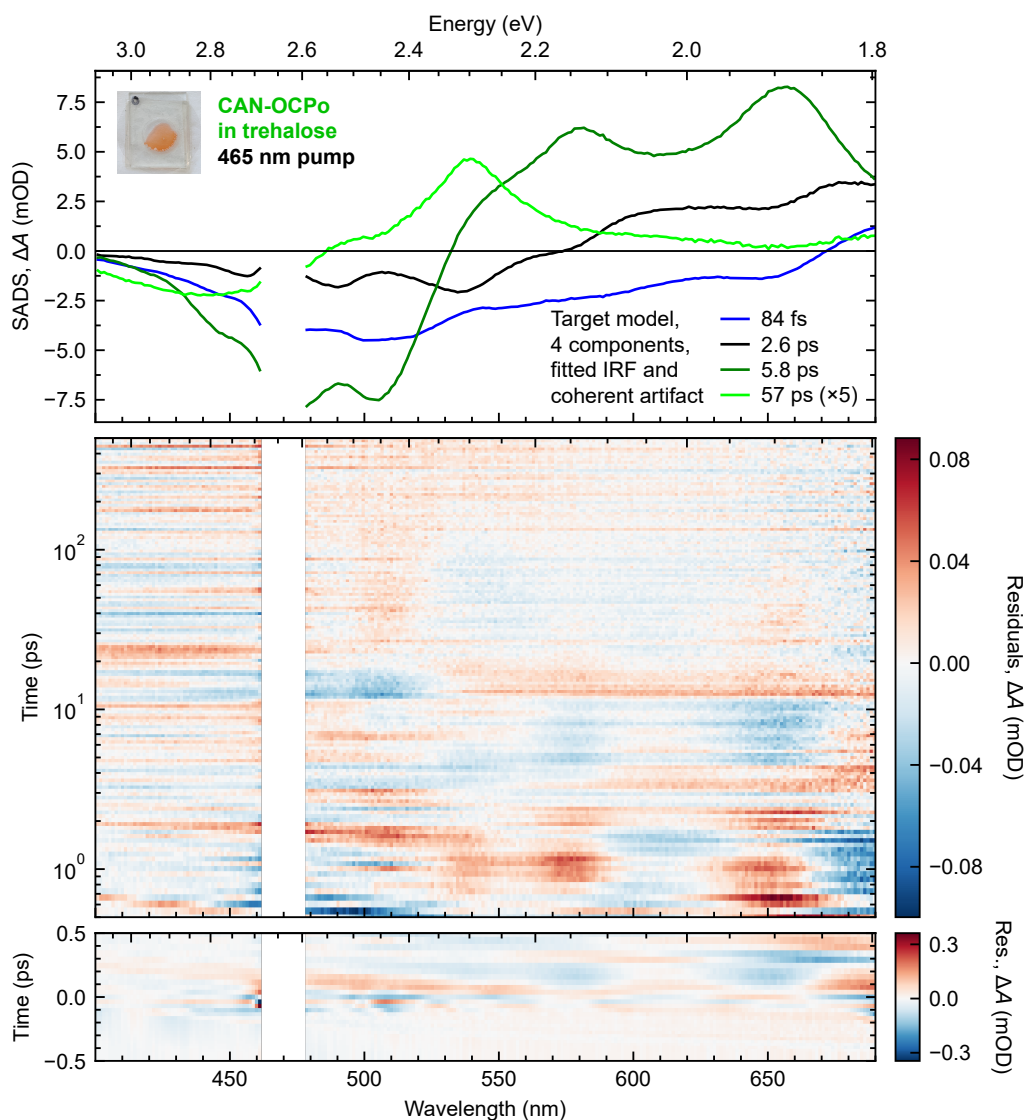


Figure S27: Results of global target analysis with a 4-component target model on transient absorption data of CAN-binding OCPo in trehalose with pump wavelength 465 nm and a UV-vis probe: SADS (top) and residuals (middle, bottom). Only the wavelength range 400–690 nm was fitted, and noisy data from 462–478 nm due to significant pump scatter was excluded from the fit. SADS time constants are specified in the legend; multiplications refer to scalings applied to the SADS. The fitted IRF has center -53 fs and FWHM 26 fs. A coherent artifact with the concentration profile of the IRF was fitted but not shown here. Residuals = Data $-$ Fit; note the logarithmic time-scale in the middle panel, and the linear time-scale and different residuals scale in the bottom panel. See text for further details.

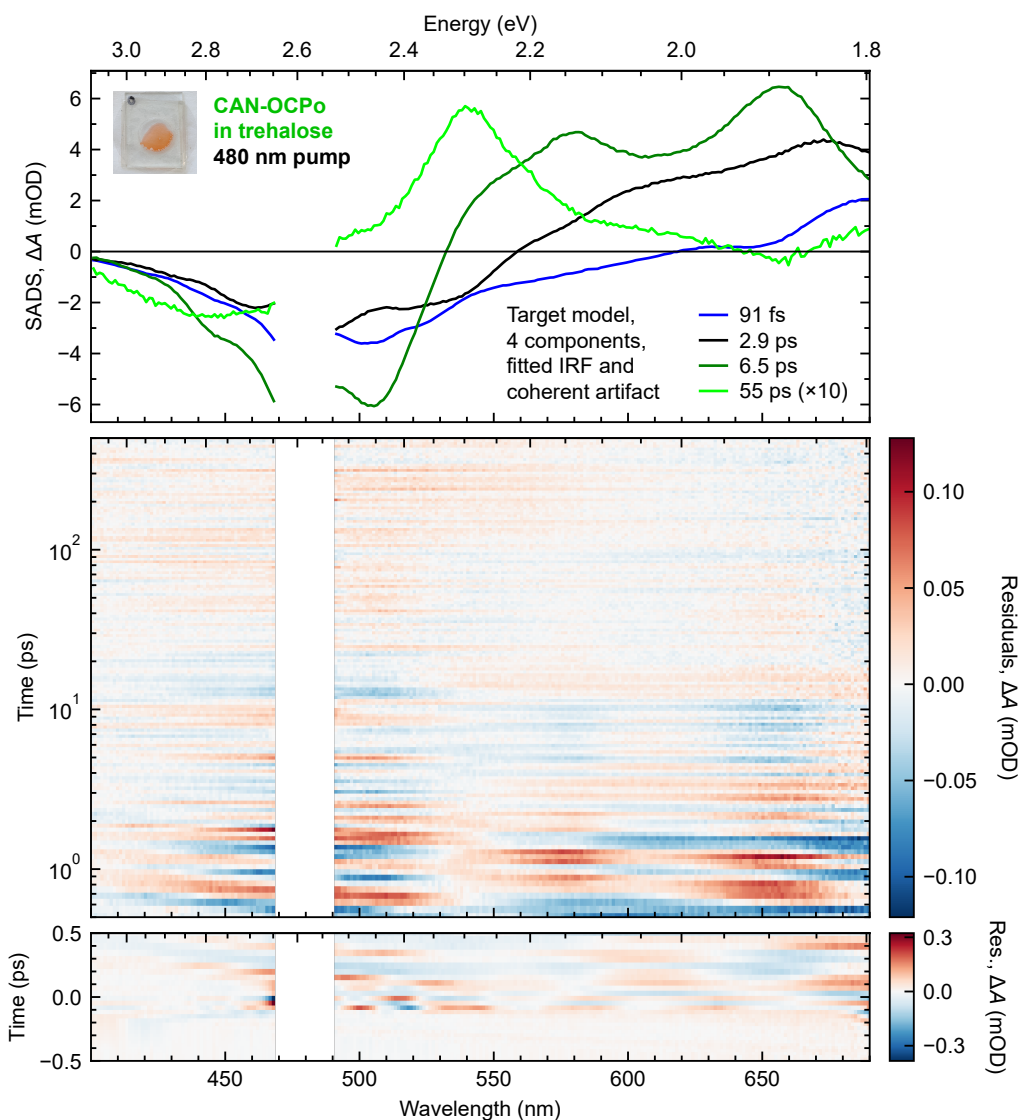


Figure S28: Results of global target analysis with a 4-component target model on transient absorption data of CAN-binding OCPo in trehalose with pump wavelength 480 nm and a UV-vis probe: SADS (top) and residuals (middle, bottom). Only the wavelength range 400–690 nm was fitted, and noisy data from 469–491 nm due to significant pump scatter was excluded from the fit. SADS time constants are specified in the legend; multiplications refer to scalings applied to the SADS. The fitted IRF has center -29 fs and FWHM 31 fs. A coherent artifact with the concentration profile of the IRF was fitted but not shown here. Residuals = Data – Fit; note the logarithmic time-scale in the middle panel, and the linear time-scale and different residuals scale in the bottom panel. See text for further details.

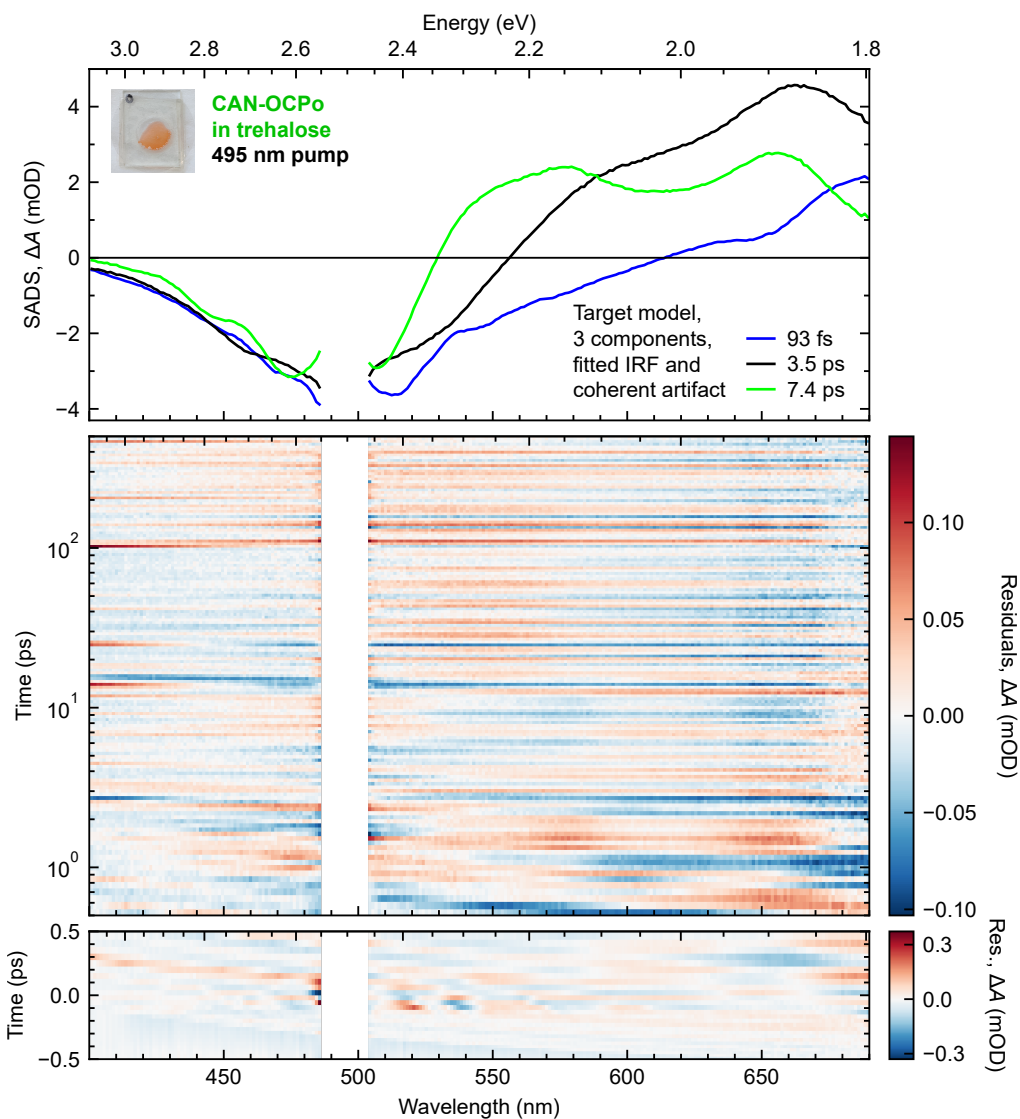


Figure S29: Results of global target analysis with a 3-component target model on transient absorption data of CAN-binding OCPO in trehalose with pump wavelength 495 nm and a UV-vis probe: SADS (top) and residuals (middle, bottom). Only the wavelength range 400–690 nm was fitted, and noisy data from 486–504 nm due to significant pump scatter was excluded from the fit. SADS time constants are specified in the legend. The fitted IRF has center -25 fs and FWHM 38 fs. A coherent artifact with the concentration profile of the IRF was fitted but not shown here. Residuals = Data – Fit; note the logarithmic time-scale in the middle panel, and the linear time-scale and different residuals scale in the bottom panel. See text for further details.

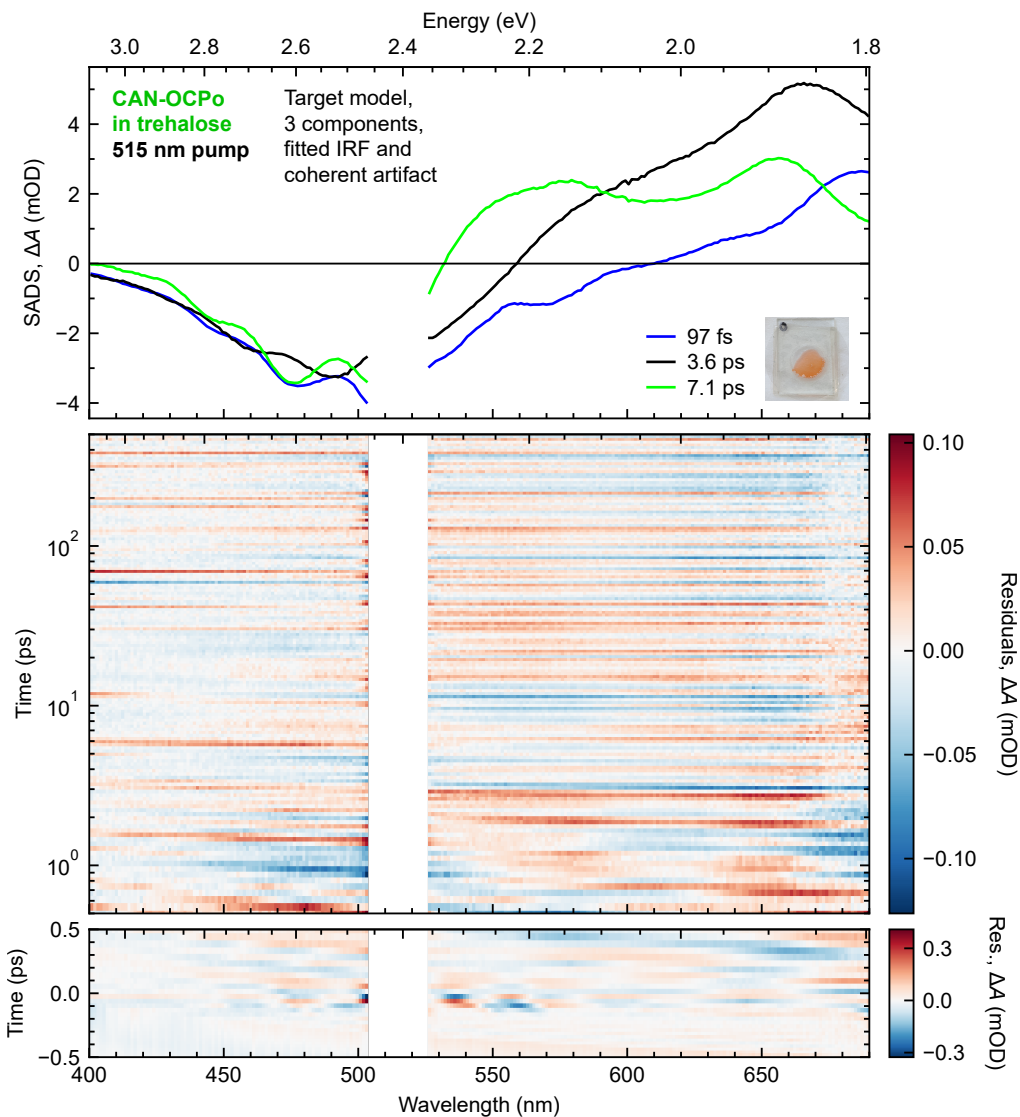


Figure S30: Results of global target analysis with a 3-component target model on transient absorption data of CAN-binding OCPo in trehalose with pump wavelength 515 nm and a UV-vis probe: SADS (top) and residuals (middle, bottom). Only the wavelength range 400–690 nm was fitted, and noisy data from 504–526 nm due to significant pump scatter was excluded from the fit. SADS time constants are specified in the legend. The fitted IRF has center -33 fs and FWHM 33 fs. A coherent artifact with the concentration profile of the IRF was fitted but not shown here. Residuals = Data – Fit; note the logarithmic time-scale in the middle panel, and the linear time-scale and different residuals scale in the bottom panel. See text for further details.

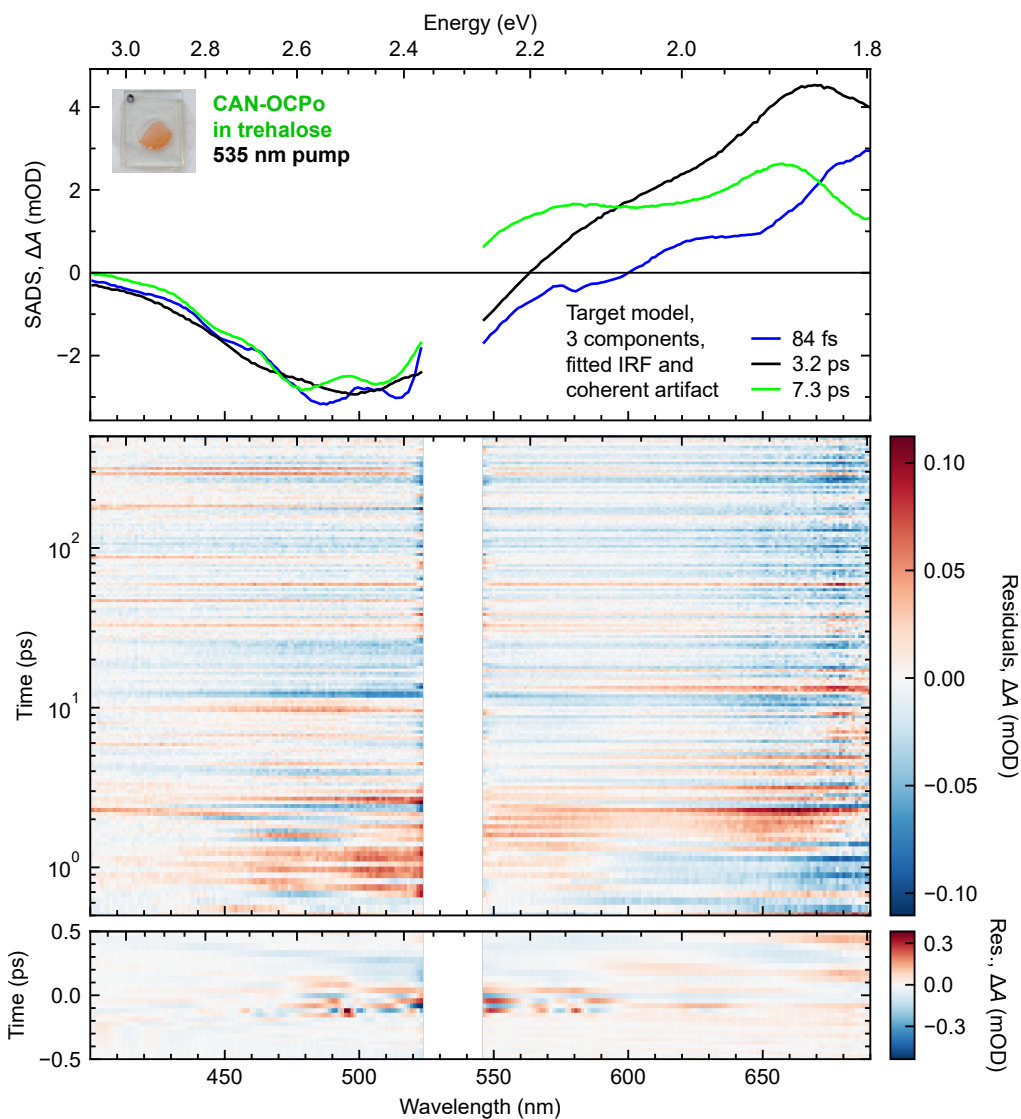


Figure S31: Results of global target analysis with a 3-component target model on transient absorption data of CAN-binding OCPo in trehalose with pump wavelength 535 nm and a UV-vis probe: SADS (top) and residuals (middle, bottom). Only the wavelength range 400–690 nm was fitted, and noisy data from 524–546 nm due to significant pump scatter was excluded from the fit. SADS time constants are specified in the legend. The fitted IRF has center -30 fs and FWHM 53 fs. A coherent artifact with the concentration profile of the IRF was fitted but not shown here. Residuals = Data – Fit; note the logarithmic time-scale in the middle panel, and the linear time-scale and different residuals scale in the bottom panel. See text for further details.

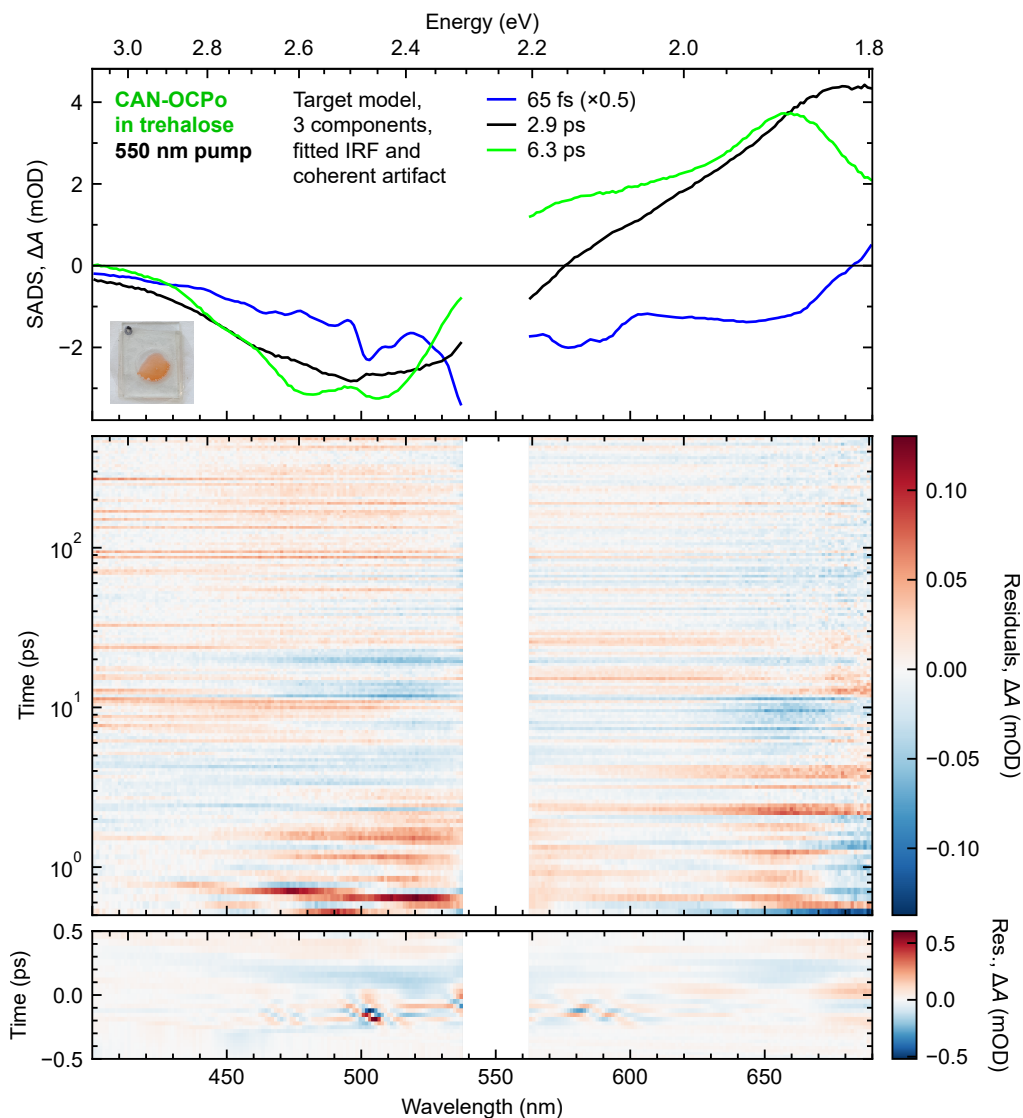


Figure S32: Results of global target analysis with a 3-component target model on transient absorption data of CAN-binding OCPo in trehalose with pump wavelength 550 nm and a UV-vis probe: SADS (top) and residuals (middle, bottom). Only the wavelength range 400–690 nm was fitted, and noisy data from 538–562 nm due to significant pump scatter was excluded from the fit. SADS time constants are specified in the legend; multiplications refer to scalings applied to the SADS. The fitted IRF has center -136 fs and FWHM 51 fs. A coherent artifact with the concentration profile of the IRF was fitted but not shown here. Residuals = Data – Fit; note the logarithmic time-scale in the middle panel, and the linear time-scale and different residuals scale in the bottom panel. See text for further details.

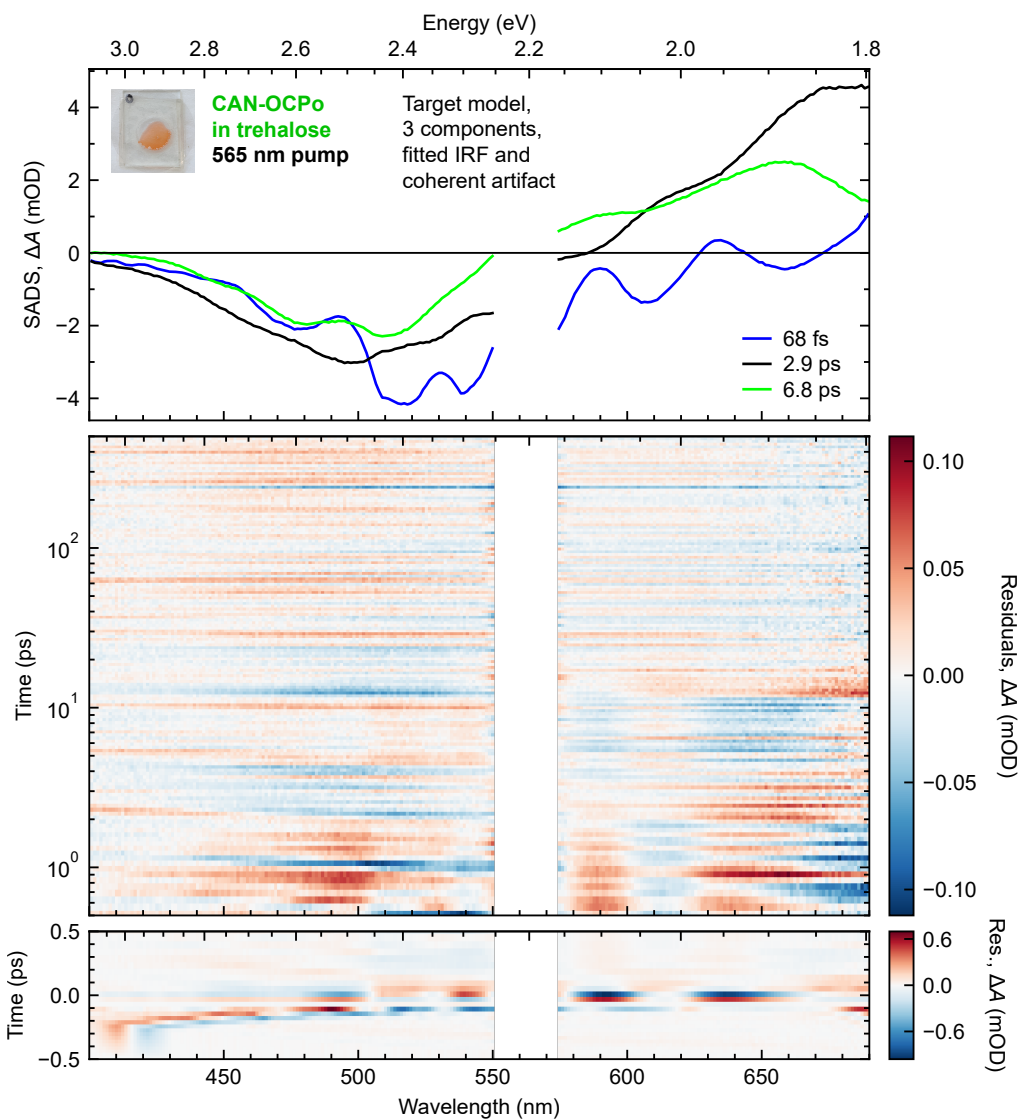


Figure S33: Results of global target analysis with a 3-component target model on transient absorption data of CAN-binding OCPo in trehalose with pump wavelength 565 nm and a UV-vis probe: SADS (top) and residuals (middle, bottom). Only the wavelength range 400–690 nm was fitted, and noisy data from 551–574 nm due to significant pump scatter was excluded from the fit. SADS time constants are specified in the legend. The fitted IRF has center -49 fs and FWHM 5 fs. A coherent artifact with the concentration profile of the IRF was fitted but not shown here. Residuals = Data – Fit; note the logarithmic time-scale in the middle panel, and the linear time-scale and different residuals scale in the bottom panel. See text for further details.

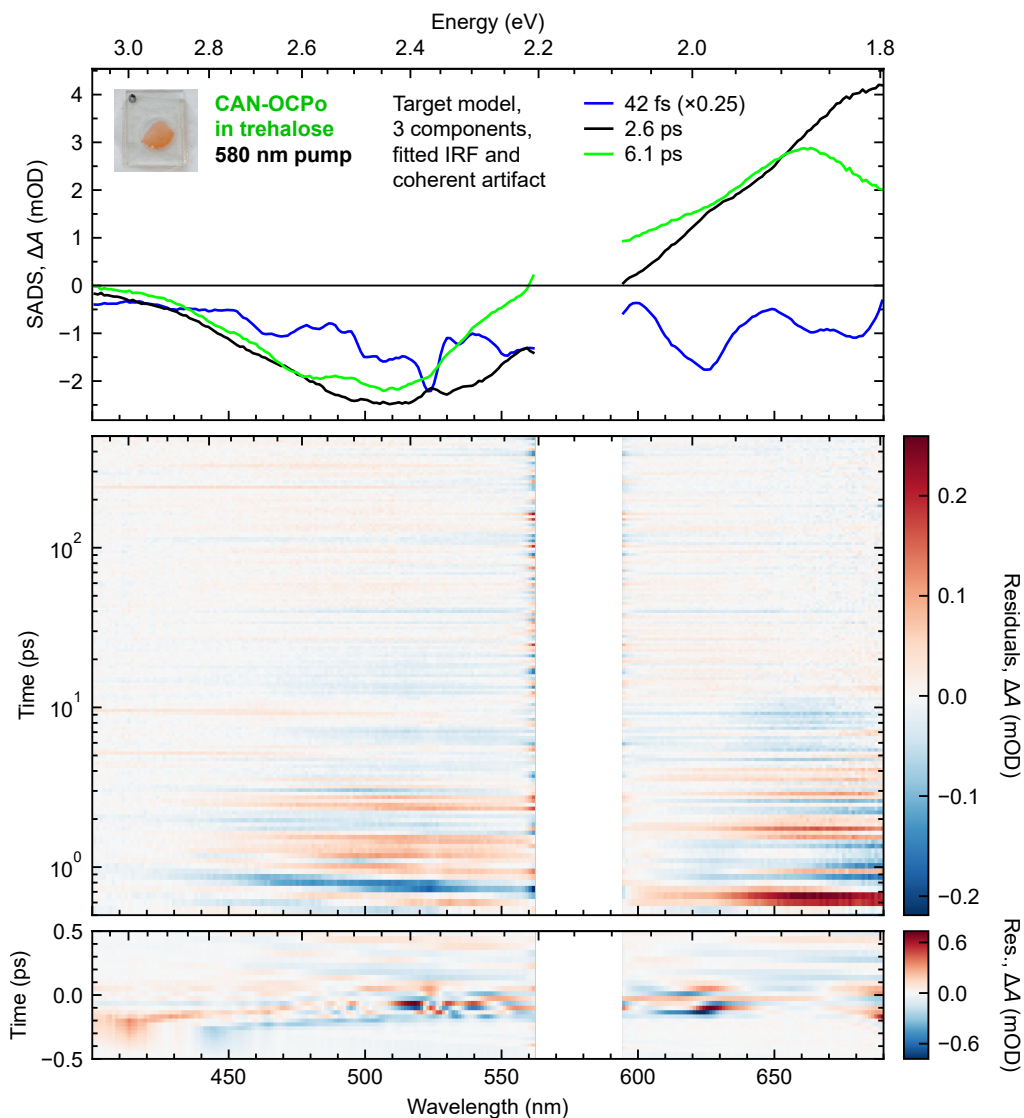


Figure S34: Results of global target analysis with a 3-component target model on transient absorption data of CAN-binding OCPo in trehalose with pump wavelength 580 nm and a UV-vis probe: SADS (top) and residuals (middle, bottom). Only the wavelength range 400–690 nm was fitted, and noisy data from 562–594 nm due to significant pump scatter was excluded from the fit. SADS time constants are specified in the legend; multiplications refer to scalings applied to the SADS. The fitted IRF has center -72 fs and FWHM 43 fs. A coherent artifact with the concentration profile of the IRF was fitted but not shown here. Residuals = Data – Fit; note the logarithmic time-scale in the middle panel, and the linear time-scale and different residuals scale in the bottom panel. See text for further details.

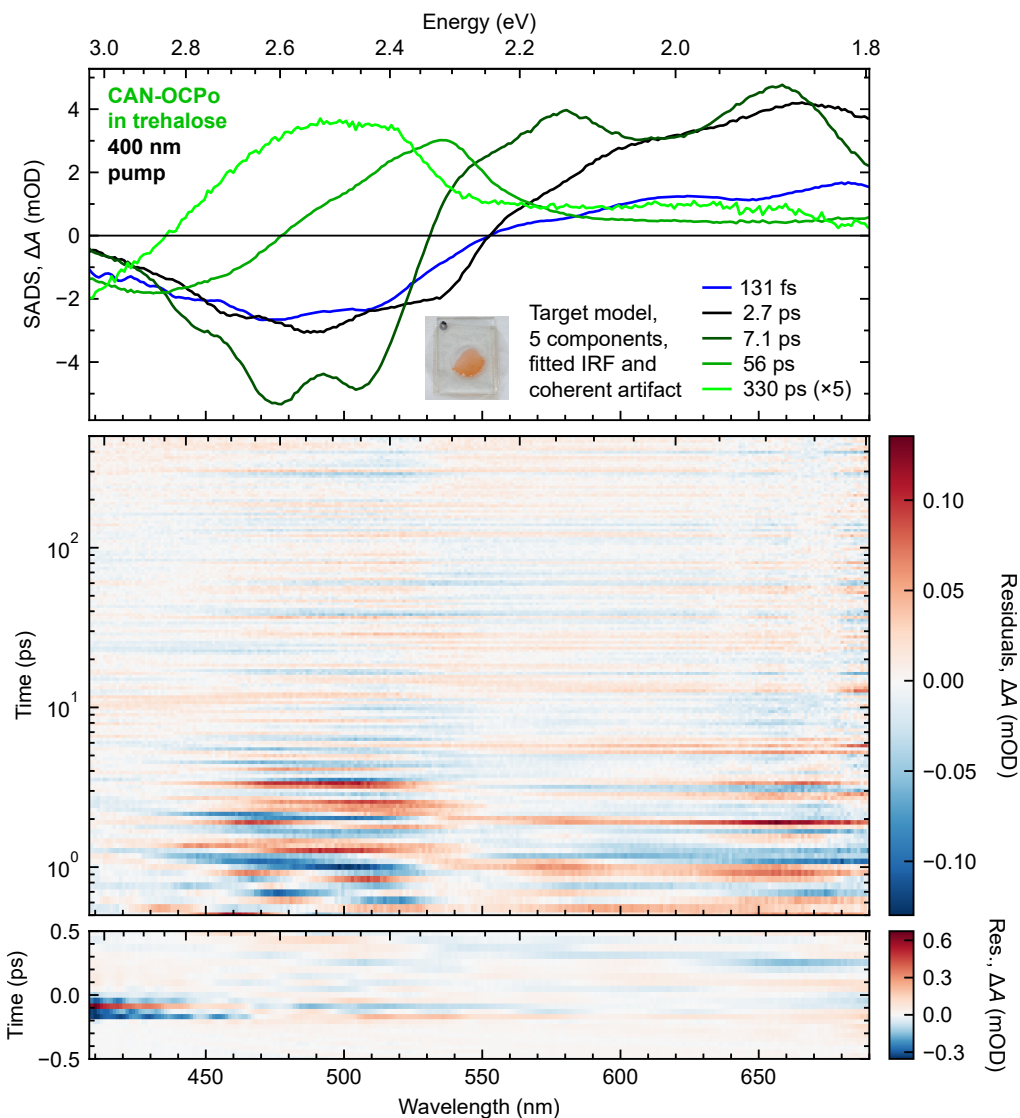


Figure S35: Results of global target analysis with a 5-component target model on transient absorption data of CAN-binding OCPo in trehalose with pump wavelength 400 nm and a UV-vis probe: SADS (top) and residuals (middle, bottom). Only the wavelength range 407–690 nm was fitted to exclude noisy data due to low probe light and significant pump scatter. SADS time constants are specified in the legend; multiplications refer to scalings applied to the SADS. The fitted IRF has center –88 fs and FWHM 59 fs. A coherent artifact with the concentration profile of the IRF was fitted but not shown here. Residuals = Data – Fit; note the logarithmic time-scale in the middle panel, and the linear time-scale and different residuals scale in the bottom panel. See text for further details.

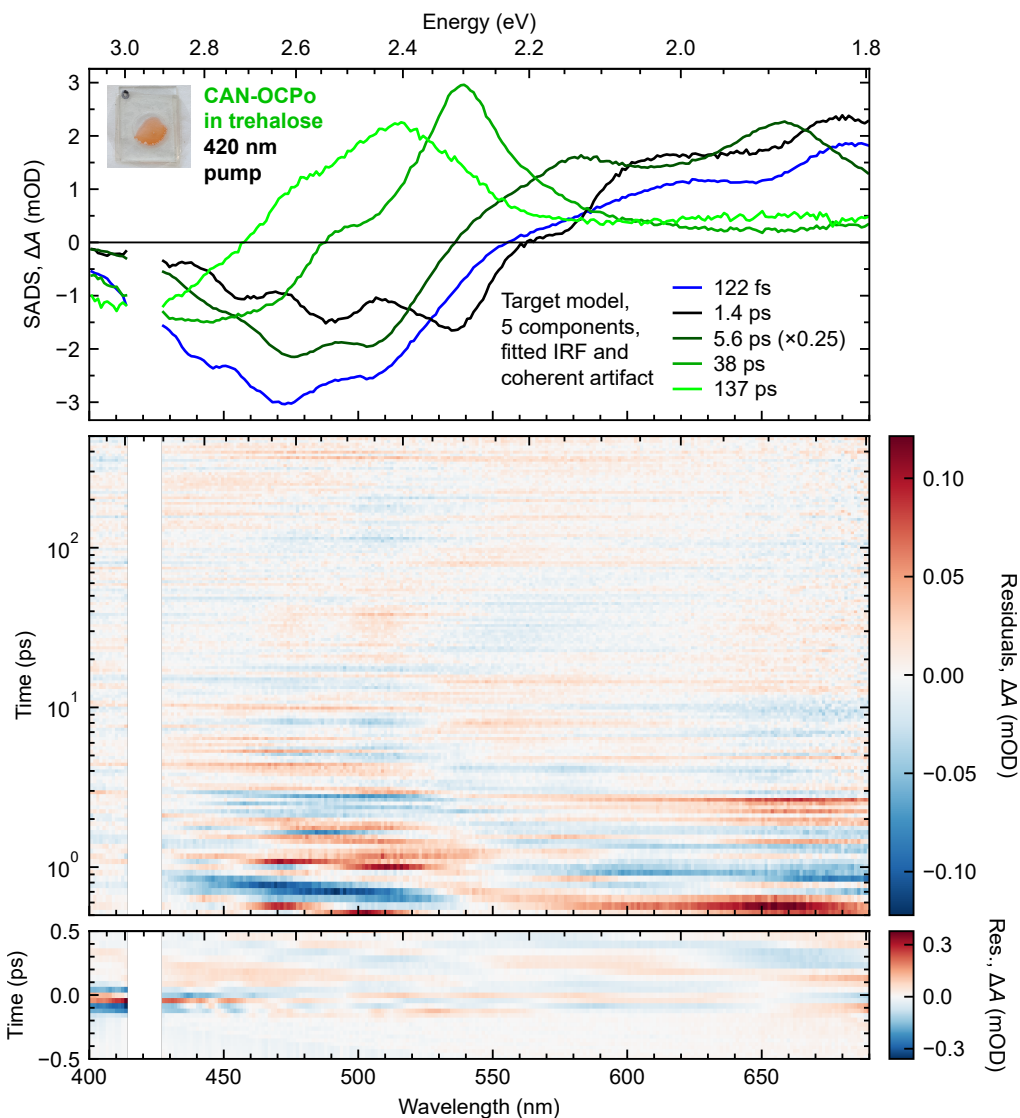


Figure S36: Results of global target analysis with a 5-component target model on transient absorption data of CAN-binding OCPo in trehalose with pump wavelength 420 nm and a UV-vis probe: SADS (top) and residuals (middle, bottom). Only the wavelength range 400–690 nm was fitted, and noisy data from 414–427 nm due to significant pump scatter was excluded from the fit. SADS time constants are specified in the legend; multiplications refer to scalings applied to the SADS. The fitted IRF has center -50 fs and FWHM 46 fs. A coherent artifact with the concentration profile of the IRF was fitted but not shown here. Residuals = Data – Fit; note the logarithmic time-scale in the middle panel, and the linear time-scale and different residuals scale in the bottom panel. See text for further details.

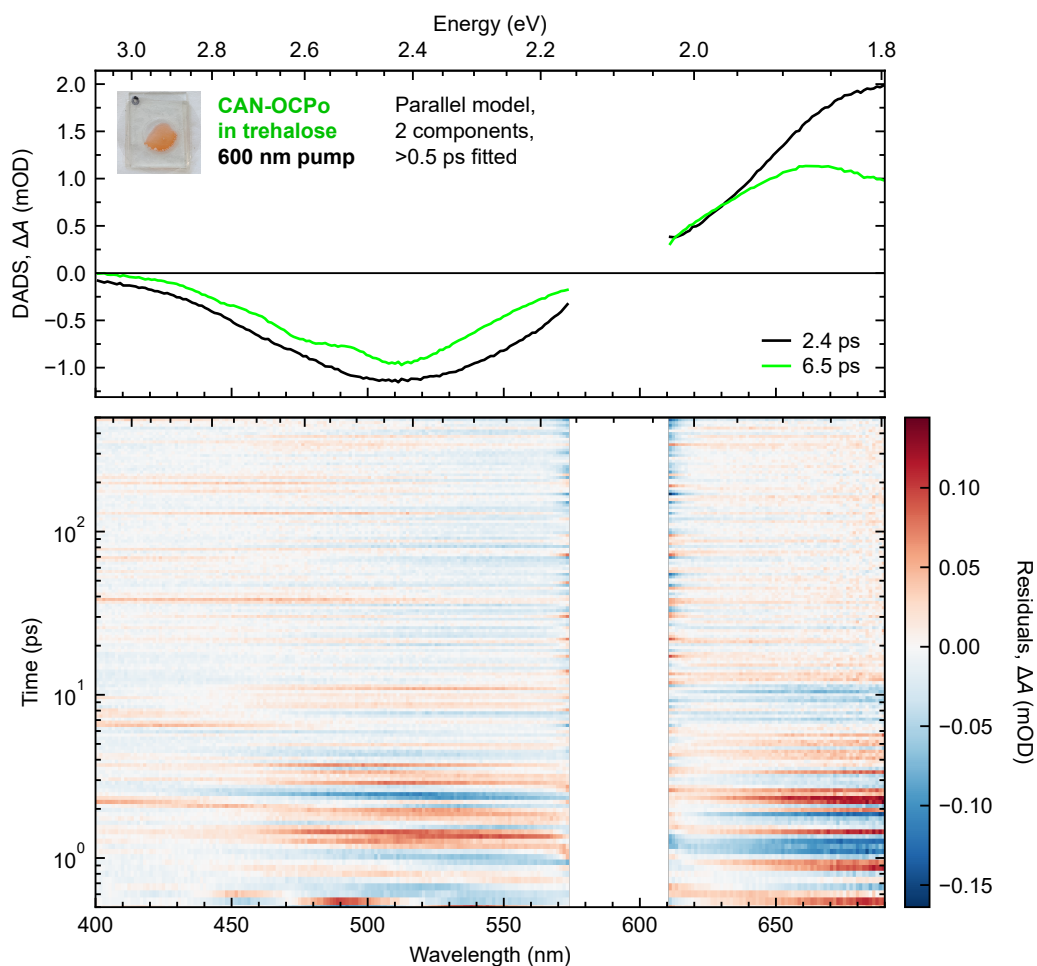


Figure S37: Results of global lifetime analysis with a 2-component parallel model on transient absorption data of CAN-binding OCPo in trehalose with pump wavelength 600 nm and a UV-vis: DADS (top) and residuals (bottom). Only the wavelength range 400–690 nm and times >0.5 ps were fitted, and noisy data from 574–611 nm due to significant pump scatter was excluded from the fit. DADS time constants are specified in the legend. Residuals = Data – Fit. See text for further details.

S7 Time-resolved absorbance fit parameters and discussion

S7.1 Global fit of difference dynamics

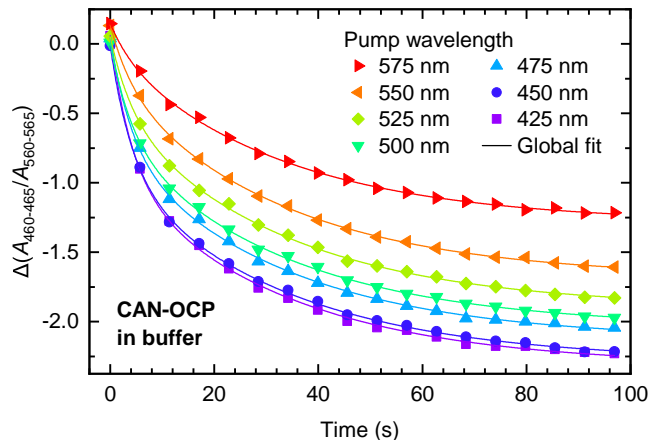


Figure S38: **Difference average absorbance ratios against time for CAN-binding OCP in buffer under excitation with narrowband laser light, fitted with a global biexponential fit.** Points are data and lines are the global biexponential fit. Only the data points shown (<100 s) are fitted. See Table S5 for the fit parameters.

Table S5: **Fit parameters found using a global biexponential fit to the data in main text Figure S38.** The biexponential equation used is $\Delta(A_{460-465}/A_{560-565})_{\text{fit}} = \beta_0 - \beta_1[1 - \exp(-t/T_1)] - \beta_2[1 - \exp(-t/T_2)]$. The fitted time constants are $T_1 = 4.12 \pm 0.18$ s and $T_2 = 32.9 \pm 0.7$ s; note that as a global fit, these are the same for all pump wavelengths. Only the times $t < 100$ s are fitted. Errors specified here are fit parameter standard errors.

λ_{pump} (nm)	β_0	β_1	β_2
425	0.061 ± 0.014	0.996 ± 0.029	1.383 ± 0.024
450	-0.012 ± 0.014	0.890 ± 0.028	1.381 ± 0.023
475	0.043 ± 0.014	0.779 ± 0.028	1.393 ± 0.022
500	0.006 ± 0.014	0.658 ± 0.027	1.389 ± 0.021
525	0.053 ± 0.014	0.527 ± 0.027	1.426 ± 0.020
550	0.136 ± 0.014	0.405 ± 0.026	1.413 ± 0.019
575	0.147 ± 0.014	0.211 ± 0.024	1.225 ± 0.018

S7.2 Experimental oversights discussion

The number of pump photons incident per second (photon rate) at the power meter position is given by

$$\dot{N}_\gamma = \frac{P}{E_\gamma} = P \frac{\lambda_{\text{pump}}}{hc} \quad (\text{S5})$$

where P is the steady-state power of the pump, $E_\gamma = hc/\lambda_{\text{pump}}$ is the per-photon energy, λ_{pump} is the pump wavelength, h is Planck's constant, and c is the speed of light in a vacuum. The fraction of pump photons absorbed by the OCP, assuming a zero angle of incidence and negligible scattering from the high-quality cuvette, is

$$F_{\text{dark}} = 1 - 10^{-A_{\text{dark}}} \quad (\text{S6})$$

where A_{dark} is the absorbance of the dark-adapted OCP in buffer measured in a separate UV-vis spectrometer at zero angle of incidence. Therefore, overlooking the later-discussed power losses and angle dependence, the number of pump-induced OCPo excitations per second (excitation rate) is given by

$$\dot{N}_{\text{pump}} = \dot{N}_\gamma F_{\text{dark}} = P \frac{\lambda_{\text{pump}}}{hc} (1 - 10^{-A_{\text{dark}}}) \quad (\text{S7})$$

which was controlled to a value of $\dot{N}_{\text{pump}} = 2.53 \times 10^{16} \text{ s}^{-1}$ in the experiment for most pump wavelengths. The exception to this control was for 675 nm pump, where instead the photon rate (Equation S5) was controlled to $\dot{N}_\gamma = 8.76 \times 10^{16} \text{ s}^{-1}$, the same as that for $\lambda = 550 \text{ nm}$; this is because OCPo is non-absorbing at 675 nm, and the tunable filter is unable to reach the higher photon rates (*i.e.* $\dot{N}_\gamma = 1.89 \times 10^{17} \text{ s}^{-1}$ at $\lambda_{\text{pump}} = 575 \text{ nm}$) when set to 675 nm.

However, as noted in the methods (Section S2.5), two of the oversights made require some scrutiny in response to the significant pump wavelength-dependence on the OCPo→OCPr yield. First, the beam path after the pump power measurement position involves reflection by three UV-enhanced Al mirrors and focusing by a lens. This results in a considerable

power (photon rate) loss, defined here by a fraction R_P that has some pump-wavelength dependence. R_P was determined once all measurement runs (three experimental replicates) were complete by taking comparative pump power measurements at the usual position as well as the sample position (doing this during the main experiment was impossible due to spatial limitations, and would also cause pre-measurement photocoverion). The resulting correction to the photon rate is

$$\dot{N}_\gamma^{\text{corr.}} = R_P \dot{N}_\gamma = R_P P \frac{\lambda_{\text{pump}}}{hc} \quad (\text{S8})$$

which we note remains incident on the cuvette rather than on the buffer. The second oversight was that the pump light was not close to normal incidence to the cuvette; it was at an angle of incidence $\theta \sim 40^\circ$, resulting in the pump path length within the buffer being extended compared to that at normal incidence by a factor $1/\cos\theta$. Hence, since absorbance is directly proportional to path length in the sample (from the Beer-Lambert law⁹²), the corrected absorbance is $A_{\text{dark}}/\cos\theta$, and therefore the correct fraction of pump photons absorbed is

$$F_{\text{dark}}^{\text{corr.}} = 1 - 10^{-A_{\text{dark}}/\cos\theta} \quad (\text{S9})$$

where we recall that A_{dark} is determined at normal incidence in a separate UV-vis spectrometer. We note we are continuing to assume negligible scattering of the pump off the high-quality cuvette, when for a significantly off-normal angle of incidence this may fail to be the case. Combining these corrections, we obtain

$$\dot{N}_{\text{pump}}^{\text{corr.}} = \dot{N}_\gamma^{\text{corr.}} F_{\text{dark}}^{\text{corr.}} = R_P P \frac{\lambda_{\text{pump}}}{hc} (1 - 10^{-A_{\text{dark}}/\cos\theta}) \quad (\text{S10})$$

which is the corrected pump-induced excitation rate in OCPo.

We print Table S6 with pump wavelength and the measured or calculated quantities defined in Equations S5 to S10, assuming an angle of incidence of $\theta = 40^\circ$. We highlight that

Table S6: **Pump wavelengths and powers used in experiments with photoconverting OCP in buffer, with derived quantities also printed.** Corrected quantities were calculated using unrounded values and $\theta = 40^\circ$. See Equations S5 to S10 and SI text for definitions of the quantities.

λ_{pump} (nm)	A_{dark} (OD)	F_{dark}	P (μW)	\dot{N}_γ $\times 10^{-16}$	\dot{N}_{pump} $\times 10^{-16}$	$F_{\text{dark}}^{\text{corr.}}$	R_P	$\dot{N}_\gamma^{\text{corr.}}$ $\times 10^{-16}$	$\dot{N}_{\text{pump}}^{\text{corr.}}$ $\times 10^{-16}$
425	0.233	0.415	285	6.10	2.53	0.503	0.55	3.35	1.69
450	0.397	0.599	187	4.23	2.53	0.697	0.54	2.29	1.60
475	0.551	0.719	147	3.52	2.53	0.809	0.54	1.89	1.53
500	0.552	0.719	140	3.52	2.53	0.809	0.52	1.83	1.48
525	0.345	0.548	175	4.62	2.53	0.646	0.51	2.38	1.53
550	0.148	0.289	316	8.76	2.53	0.359	0.49	4.26	1.53
575	0.062	0.134	654	18.9	2.53	0.171	0.48	9.06	1.55
675	0	0	256	8.76	0	0	0.43	3.72	0

the corrected pump-induced excitation rate ($\dot{N}_{\text{pump}}^{\text{corr.}}$) is a minimum for $\lambda_{\text{pump}} = 500$ nm, and generally increasing from there in either λ_{pump} -direction. This does not match the dependence of pump wavelength on the photoconversion dynamics, *e.g.* the wavelength dependence on the amplitudes (β_1, β_2) in the dynamics global fit (main text Figure 7b, Table S5), so we conclude that the oversights made did not have a substantial effect on the OCP_o→OCP_r photoconversion.

We note that some significant sources of error here are due to the pump power fluctuations, the intrinsic error of the Thorlabs S120VC power meter (note that R_P is calculated from two pump power measurements per pump wavelength, distinct from the single P pump power measurement per pump wavelength per experimental replicate), and the visual estimation (rather than a measurement) of the pump angle of incidence θ .